ERP SOURCE TRACKING AND LOCALIZATION FROM SINGLE TRIAL EEG/MEG SIGNALS

By Hamid R. Mohseni

SUBMITTED IN PARTIAL FULFILMENT OF THE
REQUIREMENTS FOR THE DEGREE OF
DOCTOR OF PHILOSOPHY
AT
CARDIFF UNIVERSITY
CARDIFF, WALES, UK
JANUARY 2010

© Copyright by Hamid R. Mohseni, 2010

UMI Number: U585287

All rights reserved

INFORMATION TO ALL USERS

The quality of this reproduction is dependent upon the quality of the copy submitted.

In the unlikely event that the author did not send a complete manuscript and there are missing pages, these will be noted. Also, if material had to be removed, a note will indicate the deletion.



UMI U585287

Published by ProQuest LLC 2013. Copyright in the Dissertation held by the Author.

Microform Edition © ProQuest LLC.

All rights reserved. This work is protected against unauthorized copying under Title 17, United States Code.



ProQuest LLC 789 East Eisenhower Parkway P.O. Box 1346 Ann Arbor, MI 48106-1346 For My Wife

Table of Contents

Ta	able (of Con	tents	iv
Li	st of	Table	\mathbf{s}	vii
Li	st of	Figur	es	viii
A	bstra	ct		xvi
A	ckno	wledge	ements	xviii
St	atem	ent of	Originality	xix
Li	st of	Abbre	eviations	xxii
N	omer	ıclatur	·es	xxiv
1	Intr	oducti	ion	1
	1.1	Aim a	and Objectives	. 2
	1.2		s Outline	
2	Intr	oducti	ion to EEG and MEG	7
	2.1	Electr	oencephaloghy	. 7
		2.1.1	EEG Advantages and Limitations	. 8
		2.1.2	EEG Acquisition	. 8
		2.1.3	Referencing	. 10
		2.1.4	Preprocessing	. 10
	2.2	Event-	-Related Potentials	. 12
		2.2.1	P300	. 12
	2.3	Magne	etoencephalogram and its Comparison with EEG	. 14

3	Sing	gle Tria	l Estimation and Dipole Source Localization for E/MEG:	
	a Li	teratur	re Survey	16
	3.1	Single '	Trial Estimation of ERPs	17
		3.1.1	Single-Channel Single Trial Estimation	17
		3.1.2	Multichannel Single Trial Estimation	22
	3.2	E/MEG	G Dipole Source Localization	24
	3.3	Fundar	nentals of KF and PF	28
		3.3.1	Problem Formulation in State Space	29
			Kalman Filtering	30
		3.3.3	Particle Filters	32
1	Stat	te Spac	e Approaches for Single Trial Estimation of ERPs	38
	4.1	Introdu	action	38
	4.2	Problem	m Formulation in State Space	39
	4.3	Experi	ments and Results	41
		4.3.1	Simulation Results	42
		4.3.2	Real Data Results	51
	4.4	Conclu	sions	55
,	Def	lation I	Beamforming for E/MEG Dipole Source Localization	57
	5.1	Introdu	iction	57
	5.2	Method	ds	58
		5.2.1	Problem Formulation	58
		5.2.2	Beamforming	59
		5.2.3	Deflation Beamforming	61
		5.2.4	Performance Analysis	65
		5.2.5	Iterative Localization and Deflation	67
	5.3	Numer	ical Results	68
		5.3.1	Two Dipoles Example	69
		5.3.2	Simulated MEG Localization	75
	5.4	Applica	ation to Auditory ERF	78
	5.5	Conclu	sions	80
3	Dip	ole Loc	alization and Tracking of E/MEG Sources via Joint Beam-	
	forr	ning - l	Rao-Blackwellized Particle Filtering	88
	6.1	Introdu	action	88
	6.2	Metho	ds	90
		6.2.1	Problem Formulation in State Space	90
		622	A Reamforming - RBPF in Time and Space Domains (B-RBPF)	93

	6.3	Simulation Results	97
		6.3.1 MUSIC, RAP-MUSIC, and BF	98
			00
	6.4	Conclusions	13
	A		17
7	Var	iational Bayes for Spatiotemporal Identification of ERP Subcom-	
	pon	ents 1	19
	7.1	Introduction	19
	7.2	Methods	21
		7.2.1 Problem Formulation	21
		7.2.2 Parameter Estimation by Variational Bayes	23
	7.3	Results	31
		7.3.1 Simulated Data Results	.31
		7.3.2 Real Data Results	35
	7.4	Discussion	.39
	7.5	Conclusions	42
	Α	ML Estimation of $\mathbf{a}_{k,i}$	43
	В		44
	C	Derivation of Equations (7.16) and (7.17)	45
8	Sun	nmary, Conclusions, and Future Works	47
	8.1	Summary and Conclusions	147
	8.2	Future Work	150
В	ibliog	graphy 1	52

List of Tables

6.1	Errors of two moving dipoles' locations and moments using the RBPF	
	and B-RBPF methods. The error of locations and moments are in	
	meter and μV units, respectively	113

List of Figures

2.1	Scalp electrode positions in a 10-20 system used for recording the avail-	
	able data set.	9
2.2	Oddball paradigm. Left: auditory sequences in which S refers to fre-	
	quent tones and T refers to infrequent tones. Right: thick line is the	
	result of averaging for the infrequent tones and thin line for the fre-	
	quent tones	13
4.1	Superposition of simulated ERPs and their ST estimations $SNR = -$	
	5dB and $SBR = -10dB$; (a) simulated ERPs, (b) noisy ERPs (average	
	in thick black line), (c) extracted ERPs using the KF method, and (d)	
	extracted ERPs using the PF method. Notice that the PF estimates	
	the ERPs very closely with respect to the original ERPs shown in (a).	45
4.2	Three examples for ST estimation $SNR = -5dB$ and $SBR = -10dB$;	
	(a) simulated EEG and ERP for trial number 5, (b) simulated and	
	estimated ERPs using PF and KF methods for trial number 5, (c) and	
	(d) show the results for trial number 35, while (e) and (f) demonstrate	
	the estimates for trial number 55	46

4.3	Amplitudes of the first and second peaks from trial to trial and their	
	estimations $SNR = -5dB$ and $SBR = -10dB$; (a) simulated (thick line),	
	estimated using PF (solid line) and estimated amplitudes using KF	
	(dashed line) for the positive peak, (b) estimated values for the negative	
	peak, (c) the error between the simulated and estimated amplitudes	
	for PF (black bar) and KF methods (white bar) for the first peak,	
	(d) mean and standard deviation of errors for each method (e) the	
	error between simulated and estimated amplitudes for PF (black bar)	
	and KF methods (white bar) for the second peak, and (f) mean and	
	standard deviation of errors for each method	47
4.4	Latencies of the first and second peaks from trial to trial and their	
	estimations for $SNR = -5dB$ and $SBR = -10dB$; (a) simulated (thick	
	line), estimated using PF (solid line), and estimated latencies using	
	KF (dashed line) for the positive peak, (b) simulated (thick line), esti-	
	mated using PF (solid line) and estimated latencies using KF (dashed	
	line) results for the negative peak, (c) the error between simulated and	
	estimated latencies for PF (black bar) and KF methods (white bar) for	
	the first peak, (d) the error between simulated and estimated latencies	
	for PF (black bar) and KF methods (white bar) for the second peak,	
	(e) the error between simulated and estimated latencies for PF (black	
	bar) and KF methods (white bar) for the second peak, and (f) mean	
	and standard deviation of errors for each method	49
4.5	Performance of KF and PF methods as indexed by mean square error	
	for 100 Monte Carlo trials (a) input SNR versus output SNR. Both	
	methods, especially PF, are robust to high input SNR, and (b) input	
	SBR versus output SBR. This decreases rapidly in comparison with	
	SNR	50

4.6	Estimation of P300 in real data using the proposed method (a) super-	
	position of original trials with their average, (b) ERP image of original	
	signals - there is no evident ERP signature in this image, (c) super-	
	position of estimated ERPs using the PF method, (d) ERP image of	
	estimated ERPs (P300 in red color) using the PF method, (e) esti-	
	mated P300 filtered peak amplitude versus trials using PF. There is	
	a decreasing trend across trials, (f) superposition of estimated ERPs	
	using the KF method, (g) ERP image of estimated ERPs with (P300	
	in red) using the KF method, and (h) estimated P300 filtered peak	
	amplitude versus trials using KF. Unlike PF (see (e) above) there is	
	no directional trend across trials.	53
4.7	Latency vs. amplitude in four subjects with their linear regression	
	obtained by PF shown by black and KF shown by red. A significant	
	negative correlation between amplitude and latency with average $r=$	
	$-0.357~(p < 0.01, ext{ two tailed})$ for four subjects can be seen only for	
	the PF method ($r = -0.0986$, n.s.), (a) subject number one (PF:	
	$r = -0.472, \ p < 0.001)$ (KF: $r = -0.2864, \ p < 0.05)$, (b) subject	
	number two (PF: $r = -0.400$, $p < 0.005$) (KF: $r = 0.0185$, n.s.), (c)	
	subject number three (PF: $r = -0.227$, $p < 0.05$) (KF: $r = -0.1182$,	
	n.s.), and (d) subject number four (PF: $r=-0.327,\ p<0.05$) (KF:	
	r = -0.0102, n.s.)	54
5.1	Location of sources used for different simulations; (a) axial view and	
	(b) coronal view	69
5.2	Output error vs. SNR when the sources are S1 and S2. The deflation	
	BF (red lines) has considerably better performance compared to BF	
	approach (blue lines) in the face of different value of SNRs	70

5.3	Investigation of depth of the source. The first source is fixed at S3. The	
	second source has the same x and y coordinates as those of S4, while its	
	z coordinate is decreasing. The horizontal axis is the distance between	
	second source and S4. Both BF and deflation BF are sensitive to the	
	depth of the source, however, deflation BF shows better performance.	72
5.4	Output error vs. α for investigation of correlation between sources.	
	lpha = 0 means two sources are uncorrelated and $lpha = 1$ means two	
	sources have exactly the same moments (i.e. completely correlated).	
	Deflation BF (red lines) has much less sensitivity to the correlation	
	between sources in comparison with the BF (blue lines), and its error	
	is monotonically increasing.	73
5.5	Investigation of distance between sources. The first source is fixed at	
	S3 and the second source has the same x and z coordinates as those	
	of S3, while its y coordinate is increasing. The horizontal axis is the	
	distance between two sources. When the distance between sources is	
	more than 4cm, deflation BF (red lines) has better performance than	
	BF (blue lines), however, when the sources have distance less than 3cm	
	the BF outperforms deflation BF	75
5.6	Output error vs. SBR for investigation of effect of real noise. Real	
	background MEG has been added to the simulated data. Deflation BF	
	(red lines) outperforms BF method (blue lines), and indeed is robust	
	to the non-Gaussian noise	76
5.7	Location of three dipoles used for MEG simulation in (a) axial view	
	and (b) coronal view	76

5.8	Power profile of the simulated MEG, when sources are strongly corre-	
	lated using (a) BF method, (b) deflation BF method while deflating the	
	second and third dipoles, (c) deflation BF method while deflating the	
	first and third dipoles, and (d) deflation BF method while deflating the	
	first and second dipoles. Due to correlation between the sources, BF	
	method shows activation between three actual sources. Three power	
	profiles obtained by deflation BF show that deflation BF has been	
	successful to identify the three sources	82
5.9	Estimated moments for the localized sources in Fig. 5.8 by (a) BF	
	method, and (b) deflation BF. Dotted lines are the simulated moments	
	and solid lines are the estimated moments. In contrast to the BF, the	
	deflation BF shows true variation of the moments	83
5.10	Power profile of the simulated MEG, when one source dominates oth-	
	ers using (a) BF method, (b) deflation BF method while deflating the	
	second and third dipoles, (c) deflation BF method while deflating the	
	first and third dipoles, and (d) deflation BF method while deflating	
	the first and second dipoles. In the BF approach one source dom-	
	inates others and other sources are not reconstructed. The deflation	
	BF method, however, reconstructs all the sources in three power profile	
	images successfully	84
5.11	Estimated moments for localized sources in Fig. 5.10 by (a) BF method	•
	and, (b) deflation BF. Dotted lines are simulated moments and solid	
	lines are estimated moments. In contrast to the BF, the deflation BF	
	shows true variation of the moments	85
5.12	The averaged auditory ERFs over 1500 trials. A 0.1sec pre-stimulus	
	was used for baseline corrections.	85

5.13	Power profile of real data obtained using (a) BF method in axial view,	
	(b) BF method in coronal view, (c) deflation BF while deflating the	
	second source in axial view, (d) deflation BF while deflating the second	
	source in coronal view, (e) deflation BF while deflating the first source	
	in axial view, and (f) deflation BF while deflating the first source in	
	coronal view. The estimated source locations are shown by cross mark-	
	ers. Due to partial correlation between the sources, the BF method	
	shows that the location of dipoles are bleeding towards the center of	
	the head. The deflation BF, however, shows the true location of dipoles	
	on the primary auditory cortex	86
5.14	Estimated moments of the real data sources obtained by BF (dotted	
	lines) and deflation BF (solid lines); (a) first dipole moments and (b)	
	second dipole moments. Since BF method localizes the sources closer to	
	the center of the brain, its moments have bigger amplitudes compared	
	to those of deflation BF	87
6.1	Dipole locations used in simulation studies for (a) locations in axial	
	view, and (b) the same locations in coronal view	101
6.2	Examples of simulated data: (a) noiseless moments in x , y and z di-	
	rections, (b) simulated noiseless E/MEG for 25 electrodes, and (c)	
	simulated noisy E/MEG with SNR=-5dB. The GWN was added to	
	the moments and the signals obtained after applying the forward matrix	102
6.3	Output error vs. input SNR for one stationary dipole	103
6.4	Output SNR vs. input SNR for two distal sources for (a) the first	
	source (S1) and (b) the second source (S2)	105
6.5	Output error vs. input SNR for two proximal sources for (a) the first	
	source (S3), and (b) the second source (S4)	106
6.6	Output error vs. input SNR for two deep sources for (a) the first source	
	(S5) and (b) the second source (S6)	107

6.7	Effect of correlation between sources on the output location error for	
	(a) the first source, and (b) the second source	108
6.8	Effect of colored noise on the output location error for (a) the first	
	source, and (b) the second source	109
6.9	Effect of real noise on the output location error for (a) the first source,	
	and (b) the second source	110
6.10	Output location error vs. SNR for two simulated sources. In this	
	example it is assumed that only one source is generating the the data.	111
6.11	Original and estimated dipole trajectories using the RBPF and B-	
	RBPF methods in (a) axial view and (b) coronal view	114
6.12	Original and estimated moments using RBPF and B-RBPF: (a) mo-	
	ment of the first dipole in x direction, (b) moment of the first dipole in	
	y direction, (c) moment of the first dipole in z direction, (d) moment	
	of the second dipole in x direction, (e) moment of the second dipole in	
	y direction, and (f) moment of the second dipole in z direction	115
7.1	An example of simulated EEG data with SNR = -5dB, (a) original	
	number 5 trial for multichannel EEG, (b) original number 55 trial, (c)	
	noisy number 5 trial, and (d) noisy number 55 trial	133
7.2	An example of estimated amplitude, latency, and width of two ERP	
	subcomponents from simulated data with $SNR = 5dB$, (a) amplitude,	
	(b) mean, and (c) variance	134
7.3	Estimated locations using the proposed method for Fig. 7.2 in (a) axial	
	and (b) sagittal views.	134
7.4	An example of the estimated amplitude, latency, and width of two ERP	
	subcomponents in simulated data with $SNR = -5dB$, (a) amplitude, (b)	
	latency, and (c) width	135
7.5	Estimated locations using the proposed method for Fig. 7.4 in (a) axial	
	and (b) sagittal views.	135

7.6	Average ERP over 60 trials of real data for a female subject. The	
	lower diagram represents the amplitude and time scales for all the	
	plots. P300 amplitude can be seen better in the central sensors. \dots	137
7.7	Average re-referenced and segmented data around P300 (200ms-500ms)	
	shown with red lines and fitted data shown with blue lines. The lower	
	diagram represents the amplitude and time scales for all the plots.	
	The parameters of the fitted waveforms were used for initializing the	
	algorithm.	138
7.8	Estimated amplitude, latency, and width in real data for P3a (red	
	marker) and P3b (blue marker) in (a) axial and (b) sagittal views	139
7.9	Estimated locations of P3a (red marker) and P3b (blue marker)	139

Abstract

Electroencephalography (EEG) and magnetoencephalography (MEG), which are two of a number of neuroimaging techniques, are scalp recordings of the electrical activity of the brain. EEG and MEG (E/MEG) have excellent temporal resolution, they are easy to acquire, and have a wide range of applications in science, medicine and engineering. These valuable signals, however, suffer from poor spatial resolution and in many cases from very low signal to noise ratios. In this study, new computational methods for analyzing and improving the quality of E/MEG signals are presented. We mainly focus on single trial event-related potential (ERP) estimation and E/MEG dipole source localization. Several methods basically based on particle filtering (PF) are proposed.

First, a method using PF for single trial estimation of ERP signals is considered. In this method, the wavelet coefficients of each ERP are assumed to be a Markovian process and do not change extensively across trials. The wavelet coefficients are then estimated recursively using PF. The results both for simulations and real data are compared with those of the well known Kalman Filtering (KF) approach. In the next method we move from single trial estimation to source localization of E/MEG signals. The beamforming (BF) approach for dipole source localization is generalized based on prior information about the noise. BF is in fact a spatial filter that minimizes the power of all the signals at the output of the filter except those that come from the locations of interest. In the proposed method, using two more constraints than in the classical BF formulation, the output noise powers are minimized and the interference activities are stopped.

PF is also introduced for E/MEG dipole source localization. PF, which can deal with the nonlinearity of the inverse problem, is capable of localizing and tracking E/MEG sources. This method is also combined with the BF approach and the results are compared with those of BF and recursive applied and projected MUSIC (RAP-MUSIC) techniques, which are well-established methods in E/MEG source localization. The final work is devoted to spatiotemporal separation and identification of ERP subcomponents. This method simultaneously estimates the single trial ERP signals and localizes the sources. Variational Bayes implies that the ERP subcomponent parameters can be estimated separately. Therefore, ERP source locations are estimated using PF, source amplitudes and noise covariance matrices are estimated using a maximum likelihood (ML) approach, and latency and width of ERP subcomponents are estimated using the Newton-Raphson technique. The method is verified via simulations and also applied to an oddball paradigm to show its potential use in practical applications.

Acknowledgements

I would like to thank Dr. Sanei and Dr. Wilding, my supervisors, for their many suggestions and constant support during this research. Also, I am thankful to Dr. Evans and Dr. Muthukumaraswamy in Cardiff University Brain Research Imaging Centre (CUBRIC) for collecting and providing the real EEG and MEG data.

Cardiff, Wales October 2009 Hamid R Mohseni

Statement of Originality

Chapter 4-7 of this thesis represent my original works to my best knowledge unless it is referenced or stated. In brief, these novelties stem from the following contributions:

Chapter 4: State Space Approaches for Single Trial Estimation of ERPs

Single trial estimation of ERP is formulated in state space and its recursive solution is given using particle filter.

Chapter 5: Deflation Beamforming for E/MEG Dipole Source Localization

The classical beamforming is modified by incorporating multiple constraints to its minimization criterion. The solution can be considered as a generalization of pseudo-inverse, maximum likelihood, beamforming, and beamforming with loading factor, which are well established methods for dipole source localization in E/MEG.

Chapter 6: Dipole Localization and Tracking of E/MEG Sources via Joint Beamforming - Rao-Blackwellized Particle Filtering

Dipole source localization is formulated in state space and its solution is given using Rao-Blackwellized Particle Filter. Very similar approach has been published in [12]. Our paper, which was published in Sensor, Array and Multichannel Signal Processing Conference (SAM), 2008 [77], however, shows that these two independent studies have taken place in parallel.

The most important novelty of this chapter is the use of joint beamforming and

Rao-Blackwellized particle filtering for E/MEG source localization, which improves the performance of the method compared to the Rao-Blackwellized particle filtering method.

Chapter 7: Variational Bayes for Spatiotemporal Identification of ERP Subcomponents

A new model for tracking ERP subcomponent parameters is proposed and the solution for estimating parameters are given using particle filter, maximum likelihood, and Newton-Raphson techniques. The proposed model is more comprehensive than the available models, since it considers not only variable amplitude, latency, and width but also variable locations for ERP subcomponents.

List of Publications

- Hamid R. Mohseni, Edward L. Wilding, and Saeid Sanei, "Variational Bayes for Spatiotemporal Identification of ERP Subcomponents," under review, IEEE Transaction on Biomedical Engineering, 2009.
- Hamid R. Mohseni, Edward L. Wilding, and Saeid Sanei, "A Deflation Based Beamforming Approach for EEG Multiple Dipole Source Localization," under second review, IEEE Transaction on Biomedical Engineering, 2009.
- Hamid R. Mohseni, Kinaoush Nazarpour, Edward L. Wilding, and Saeid Sanei,
 "Application of Particle Filters in Single Trial Event-Related Potential Estimation," *Physiol. Meas.* vol. 30, pp 1101-1116, 2009.
- K. Nazarpour, H.R. Mohseni, C.W. Hesse, J. A. Chambers, and S. Sanei "A Novel Semi-Blind Signal Extraction Approach for the Removal of Eye-Blink Artifact from EEGs," *EURASIP Journal on Advances in Signal Processing*, 2008.

- Hamid R. Mohseni, Edward L. Wilding, and Saeid Sanei, "A New Beamforming-Based MEG Dipole Source Localization Method," submitted to IEEE International Conf. On Acoustic, Speech and Signal Processing, ICASSP, 2010.
- Hamid R. Mohseni, and Saeid Sanei, "A New Method for Spatiotemporal Identification of Event-Related Potential Subcomponents," *International Conference of the IEEE in Medicine and Biology (EMBC)*, 2009 (invited paper).
- Hamid R. Mohseni, Edward L. Wilding, and Saeid Sanei, "A Beamforming Particle Filter for EEG Dipole Source Localization," *IEEE International Conf.* On Acoustic, Speech and Signal Processing, ICASSP, 2009 (best student paper in bio-imaging and signal processing area).
- Hamid R. Mohseni, Edward L. Wilding, and Saeid Sanei "Sequential Monte Carlo Techniques for EEG Dipole Placing and Tracking," Fifth IEEE Sensor Array and Mutichanel Signal processing Signal Processing Workshop, SAM, 2008.
- Hamid R. Mohseni, Edward L. Wilding, and Saeid Sanei, "Single Trial Estimation of Event-Related Potentials Using Particle Filtering" IEEE International Conf. On Acoustic, Speech and Signal Processing, ICASSP, 2008.
- Hamid R. Mohseni, Edward L. Wilding, and Saeid Sanei "Preprocrssing of Event-Related Potential Signals via Kalman Filtering and Smoothing," 15th IEEE International Conference on Digital Signal Processing, DSP, 2007.

List of Abbreviations

AR Autoregressive

BESA Brain Electrical Source Analysis

BF Beamforming

BOLD Blood Oxygenation Level Dependent

B-RBPF Beamforming-RBPF

DWT Discrete Wavelet Transforms

E/MEG EEG and MEG

ECD Electric Current Dipole

ECoG Electrocorticogram

EEG Electroencephalogram

EOG Electro-oculogram

ERP Event-Related Potentials

fMRI Functional Magnetic Resonance Imaging

GWN Gaussian White Noise

HEOG Horizontal EOG

i.i.d. Independent and Identically-Distributed

ICA Independent Component Analysis

KF Kalman Filtering

LCMV Linearly Constrained Minimum Variance

MAP Maximum A PosterioriMEG Magnetoencephalogram

ML Maximum Likelihood

MUSIC

MUltiple Signal Classification

PET

Positron Emission Tomography

 \mathbf{PF}

Particle Filtering

RAP-MUSIC Recursively Applied and Projected MUSIC

RBPF

Rao-Blackwellized Particle Filter

SBR

Signal to Background Ratio

SIR-PF

Sampling Importance Resampling PF

SNR

Signal to Noise Ratio

ST-ERP

Single Trial Event-Related Potential

SVD

Singular Value Decomposition

VEOG

Vertical EOG

Nomenclatures

t	Discrete time index
\boldsymbol{k}	Trail index
$(.)^T$	Transpose operation
(.) [†]	Pseudoinverse
$. _{2}$	Frobenious norm
p(.)	Probability density function
p(. .)	Conditional probability density function
\mathbf{x}_t	State of the system at time t
\mathbf{y}_t	Measurement vector at time t (EEG and MEG)
\mathbf{Y}_k	Measurement matrix at the kth trail (EEG and MEG)
f_t and h_t	General nonlinear functions
\mathbf{w}_t	State noise
\mathbf{v}_t	Measurement noise
\mathbf{Q}_w	Covariance matrix of the state noise
\mathbf{Q}_v	Covariance matrix of the measurement noise
$\mathcal{N}(a;,m,P)$	Gaussian function with mean vector \mathbf{m} and covariance matrix \mathbf{P}
	evaluated at a
$\mathcal{N}(\mathbf{m},\mathbf{P})$	Gaussian distribution with mean vector $\mathbf m$ and covariance matrix $\mathbf P$
\mathbf{K}_t	Kalman gain at time t
$\delta(.)$	Dirac delta function
N	Number of particles
$w_t^{(n)}$	Weight of n th particle at time t

$x_t^{(n)}$	The n th particle at time t
$\pi(.)$	Importance density function
$oldsymbol{ ho}_i$	Location of the ith dipole
H	Forward matrix
\mathbf{m}_i	Moment of the ith dipole
I	Identity matrix
W	Linear spatial filter
\mathbf{C}_y	Covariance matrix of the data
\mathbf{C}_v	Covariance matrix of the noise
Γ	Lagrange multiplier
P_{signal}	Power of the signal
P_{noise}	Power of the noise
\mathbf{R}_t	Matrix of all dipole locations
$\tilde{ ext{M}}_t$	Matrix of all dipole moments
$\underline{\mathbf{m}}_t$	Vector of all dipole moments
L	Number of sensors

Window length

M

Chapter 1

Introduction

Functional brain imaging is a relatively new and multidisciplinary research field that encompasses techniques devoted to a better understanding of the human brain through noninvasive imaging of the electrophysiological, hemodynamic, metabolic, and neurochemical processes. These imaging techniques are powerful tools for studying neural processes in the normal and pathological brain functions. Clinical applications include improved understanding and treatment of serious neurological and neuropsychological disorders such as intractable epilepsy, schizophrenia, depression, and Parkinson's and Alzheimer's diseases.

Images of dynamic changes in the spatial distribution of brain metabolism and neurochemistry can be formed using positron emission tomography (PET). These images have spatial resolutions as high as 2mm. Temporal resolution, however, is limited to several minutes because of the dynamics of the processes being studied and photon-counting noise. For more direct studies of neural activity, local hemodynamic changes may be investigated. As neurons become active, they induce very localized changes in blood flow and oxygenation levels that can be imaged as a correlate of neural activity. Hemodynamic changes can be detected using PET [16], functional

magnetic resonance imaging (fMRI) [113], and transcranial optical imaging [44] methods. Of these, fMRI is currently the most widely used and can be readily performed using a 1.5-7T clinical MRI magnet. fMRI studies are capable of producing spatial resolutions as high as 1-3mm, however, temporal resolution is limited by the relatively slow hemodynamic response, compared to electrical neural activity. In addition to limited temporal resolution, interpretation of fMRI data is hampered by the rather complex relationship between the blood oxygenation level dependent (BOLD) changes and the underlying neural activity. Regions of BOLD changes in fMRI images do not necessarily correspond one-to-one with regions of electrical neural activity.

Among the available functional imaging techniques, electroencephalogram (EEG) and magnetoencephalogram (MEG) uniquely have temporal resolutions below 1ms. This temporal precision allows us to explore dynamics of neural networks or cell assemblies that occur at typical time scales in the order of tens of milliseconds [83]. EEG and MEG (E/MEG) are two complementary techniques that measure, respectively, the scalp electric potentials and the magnetic induction outside the head produced by electrical activity in neural cell assemblies. They directly measure the electrical brain activity and offer the potential for superior temporal resolution when compared to PET or fMRI. Sampling of electromagnetic brain signals at millisecond intervals is readily achieved and is limited only by the multichannel analog-to-digital conversion rate of the measurements.

1.1 Aim and Objectives

There are drawbacks, however, that limit the application of E/MEG. One of the main drawbacks is the low spatial resolution. This is because of the fact that the

E/MEG resolution is limited by both the number of spatial measurements and their location over the scalp. The only way to localize the putative electric sources in the brain is through the solution of the inverse problem, a problem that can only be solved by introducing a priori assumptions on the generation of E/MEG signals. The more appropriate these assumptions are the more trustable are the source estimations. During the last two decades different such assumptions have been formulated and implemented in inverse solution algorithms. They range from single equivalent current dipole estimations to the calculation of three-dimensional (3D) current density distributions. Each approach uses different mathematical, biophysical, statistical, anatomical or functional constraints.

The main shortcoming of the current source localization methods is that the signal should be stationary during the time of processing. Here, using particle filtering (PF) new methods that can be applied to the non-stationary signals are proposed. The conventional beamforming (BF) approach for source localization is also extended when the location and covariance matrix of the noise is known. Furthermore, a new model for analyzing event-related potentials (ERP) is given and its parameters are estimated separately using different methods. In fact, this method is a single trial estimation that can also localize the source activities.

Another main drawback of E/MEG is its low signal to noise ratio. Conventional methods to improve ERP signal quality involve averaging time-locked segments of the EEG signals over many trials. These methods assume that the statistical parameters of the ERP waves of a given kind remain the same over time and the background EEG is a random process that is attenuated by averaging over trials. There is evidence, nevertheless, that ERP waves may vary considerably over time. Hence, along with

many approaches for estimation of single trials, novel methods to investigate the variability of ERPs across trials are proposed.

Several techniques are proposed in this study and in the following, a brief overview of them is presented.

1.2 Thesis Outline

The layout of the thesis is as follows. In Chapter 2, an introduction to EEG and its acquisition and specifications is presented followed by a brief introduction to ERP and its application focusing on the P300 component. This chapter ends with an overview of MEG and its comparison with the EEG signals.

Bayesian filtering and mathematical frameworks for Kalman filtering (KF) and PF, which are the main bases of different proposed approaches in this study, are presented in Chapter 3.

In Chapter 4, an approach for estimation of single trial event-related potentials (ST-ERPs) using PF is presented. The method is based on recursive Bayesian mean square estimation of ERP wavelet coefficients, which are estimated sequentially by their previous estimates as prior information. To enable a performance evaluation for this approach in the Gaussian and non-Gaussian distributed noise conditions, Gaussian white noise (GWN) and real electroencephalogram (EEG) signals is added to the simulated ERPs and the results are compared to that of KF approaches.

In Chapter 5, a deflation scheme based on BF for multiple dipole source localization of surface E/MEG data is considered. Two more constraints are added to the conventional BF formulation and a closed-form solution is given. The first constraint minimizes the power of the noise at the output of the BF. The solution can

be considered as a generalization of pseudo-inverse, maximum likelihood, and loading factor methods which have been applied effectively for E/MEG source localization. By adding another constraint to the BF formulation, the identified dipoles are deflated and, simultaneously, the location of the next dipole is identified. This method is called deflation BF and is capable of detecting highly correlated sources, as well as sources with small power that are dominated by other sources. An iterative deflation and localization method is also proposed to improve the accuracy of the method.

In addition, in Chapter 6, a method based on Rao-Blackwellized particle filtering (RBPF) and BF for E/MEG dipole source localization and tracking is presented. The localization problem is formulated in state space and PF is employed to provide a recursive nonlinear and non-Gaussian Bayesian solution. The use of Rao-Blackwellization in combination with PF improves the performance and reduces the computational costs. In this approach, the nonlinear part of the model (location) is estimated by PF and the linear part of the model (the moments) is marginalized out and estimated using KF. Further performance improvement can be obtained via joint beamforming-RBPF (B-RBPF). In this approach, it is assumed that the data is stationary within a window around the current time sample. RBPF and B-RBPF were applied to different kinds of simulated data and the results were compared with those obtained by using RAP-MUSIC and BF algorithms, which are two well-established methods for dipole source localization.

Finally, in Chapter 7 a novel method for the detection and tracking of ERP subcomponents from trial to trial is proposed. The ERP subcomponent sources are assumed to be electric current dipoles (ECDs) and their locations and parameters (amplitude, latency, and width) are estimated and tracked from trial to trial. Variational Bayes implies that the parameters can be estimated separately using the likelihood function of each parameter. Estimations of dipole locations, which have nonlinear relation to the measurement, are given by PF, estimations of amplitude and noise covariance matrix of the measurement are optimally given by maximum likelihood (ML) approach, and estimations of latency and width of the Gaussian functions are given by Newton-Raphson technique. New recursive methods are introduced for both ML and Newton-Raphson approaches to prevent the divergence of the filtering in the presence of very low signal to noise ratio (SNR). The main advantage of the method is the ability to track the varying dipole locations.

Chapter 2

Introduction to EEG and MEG

In this chapter, an introduction to EEG and its acquisition is given first and then a brief review of ERPs focusing on the P300 component is presented. In the final section, MEG is introduced and compared with EEG.

2.1 Electroencephaloghy

EEG is the recording of electrical activity from over the scalp produced by firing the neurons within the brain. These electrical activities can provide records of brain activity at any reasonable scale of temporal resolution. In comparison with the other neuroimaging techniques, EEG can be acquired easily and inexpensively. Because of these advantages, it has been widely employed in human monitoring and research by workers from different fields. For instance, EEG has been used for clinical diagnosis of epilepsy. It has also attracted engineers to provide a method for interfacing brain and machine, which can improve the life style of disabled people. In addition to the medical applications, EEG has been recently employed in game industries and many commercial products based on EEG have been produced.

2.1.1 EEG Advantages and Limitations

EEG has several advantages as a tool for investigation of the brain activities. For instance, EEG is non-invasive, convenient to acquire and inexpensive. EEG also has a high temporal resolution compared to other techniques such as fMRI and is capable of detecting changes in electrical activity in the brain in a millisecond time scale. Furthermore, EEG measures the brain's electrical activity directly, while other methods record the changes in blood flow (e.g., SPECT, fMRI) or metabolic activity (e.g. PET), which are indirect markers of brain electrical activity.

EEG has several limitations. The most important one is its poor spatial resolution which is limited by the number and location of the electrodes. Another important limitation is that some particular sets of neurons make more contribution to EEG signals (those which are located in the superficial layers of cortex and generate radial currents toward the skull) than the others (those which are located in deep structures such as the hippocampus and produce currents tangential to the skull).

2.1.2 EEG Acquisition

In conventional scalp EEG, the recording is obtained by placing silver/silver chloride electrodes on the scalp using a conductive gel or paste, usually after preparing the scalp area by light abrasion to reduce the impedance. Electrode locations and names are specified by the international 10-20 system in most clinical and research applications. An example of the electrode locations and names in a two-dimensional map has been shown in Fig. 2.1.

Extra electrodes are sometimes used for the measurement of EOG, ECG, and EMG of the eyelid and eye surrounding muscles. In the available recording, two electrodes

were placed above and below the eye for vertical EOG (VEOG) and two others placed left and right of the eye for horizontal EOG (HEOG). VEOG and HEOG usually are used as a cue to remove eye blink and movement related artifacts from the signals.

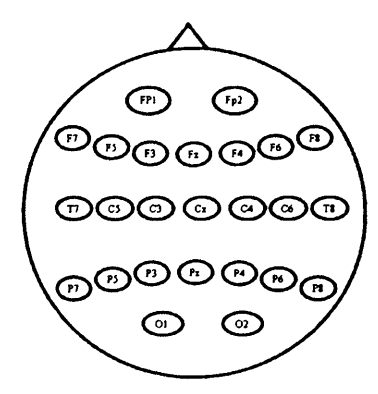


Figure 2.1: Scalp electrode positions in a 10-20 system used for recording the available data set.

As an example in epilepsy surgery, it may be necessary to insert electrodes near the surface of the brain. This is referred to as electrocorticography (ECoG), intracranial EEG (I-EEG) or subdural EEG (SD-EEG). The ECoG signal is processed in the same manner as digital scalp EEG, with a couple of caveats. ECoG is typically recorded at higher sampling rates than scalp EEG because of the requirements of Nyquist theorem - the subdural signal is composed of a higher predominance of higher frequency components. Also, many of the artifacts which affect scalp EEG do not impact ECoG, and therefore the linear filtering in preprocessing stage is often not needed.

2.1.3 Referencing

Electric potentials are defined only with respect to a reference, i.e., an arbitrarily chosen zero level. The choice of the reference may differ depending on the purpose of the recording and has to be selected in advance. In referential montage, each channel represents the difference between a certain electrode and a predefined reference electrode. There is no standard position at which this reference is always placed. Midline positions are often used since they do not amplify the signal in one hemisphere versus the other. In this work, the Fz (midline frontal) site as the reference is used in online recording. This referencing was changed (off-line) to another popular reference called linked mastoids - a mathematical average of electrodes attached to both left and right mastoids. With digital EEG, all signals are typically digitized and stored usually w.r.t a particular referential montage and the signals using other montages can be mathematically constructed.

Another type of montage is *average reference* montage, which is especially useful for localization of the sources. In this montage, the outputs of all of the channels are averaged, and the averaged signal is used as a common reference for each channel.

2.1.4 Preprocessing

A linear bandpass filter is usually used to remove the noise. Typical settings for the highpass and lowpass cut-off frequencies are 0.5-1 Hz and 35-70 Hz, respectively. The highpass part typically filters out the slow artifacts, such as electrogalvanic signals and movement-related artifact, whereas the lowpass part filters out the high-frequency artifacts, such as electromyogram signals. An additional notch filter is sometimes used to remove the artifact caused by electrical power lines (50Hz in Europe). In

the available recording, the frequency bandwidth of the linear bandpass filter was 0.03-40Hz and the sampling rate was set to 250Hz. The data are digitized using a 16 bit analog to digital convertor with 250Hz sampling rate which satisfies the Nyquist theorem for an EEG with a bandwidth within 0.03-40Hz.

During the recording, EEG signals undergo slow shifts over time such that the zero level might differ considerably across channels. These signal shifts can be due to brain activity, but can also be caused by sweating (in the case of EEG), muscle tension, or other noise sources. It would be therefore desirable to have a time range where one can reasonably assume that the brain is not producing any stimulus related activity, and that any shift from the zero line is likely due to noise. In most studies, this baseline interval is defined as several tens or hundreds of milliseconds preceding the stimulus - in the available data set, a 0.15sec pre-stimulus interval was used for baseline correction. For each recorded channel, the mean signal over this interval is computed, and subtracted from the signal at all time points. This procedure is usually referred to as baseline correction.

Eye blink is one of the major artifacts in a laboratory environment. In many applications of ERP, the recorded trials are visually inspected and those containing eye blink are removed from analysis. Another useful and semi automatic method, which has been used in the available data set, is independent component analysis (ICA) [112]. In this method, after applying ICA, the component(s) including eye blink are set to zero and they are back projected to obtain a set of eye blink-free EEG signals.

2.2 Event-Related Potentials

ERP is any measured brain response that is directly the result of a thought or perception. More formally, it is any stereotyped electrophysiological response to an internal or external stimulus. ERP experiments usually involve a subject being provided a stimulus to which s/he reacts either overtly or covertly. There are often at least two conditions that vary in some manner of interest to the researcher. As this stimulus-response is going on, an EEG is being recorded from the subject. The ERP is obtained by segmenting and averaging the EEG signal for each of the trials within a certain condition; averages from one stimulus-response condition can then be compared with averages from the responses from other stimulus.

There is considerable interest in the EEG techniques concerned with ERP recording and analysis since they deal with brain functional and mental abnormalities and can be used as indicators of cognitive processes and dysfunctions which are not accessible in behavioral testings.

2.2.1 P300

In this section P300 which is a well-known ERP component is explained. This component is used to validate the proposed methods in this thesis. P300 is a positive wave that occurs approximately 300ms after a rare or task-relevant stimulus, which can be auditory, visual, or somatosensory. P300 is the most widely used ERP because of the relatively large amplitude $(5-20\mu V)$ and easy acquisition.

The paradigm used to elicit a P300 is the presentation of unexpected and infrequent stimuli randomly interspersed between frequent stimuli to an attentive subject [104]. In this paradigm, labeled as oddball, the subject usually has to classify the

stimuli, i.e. to count the infrequent target, or to press a button whenever an infrequent stimulus occurs. An example of auditory oddball paradigm in which frequent and infrequent tones are presented to participants has been shown in Fig.2.2.

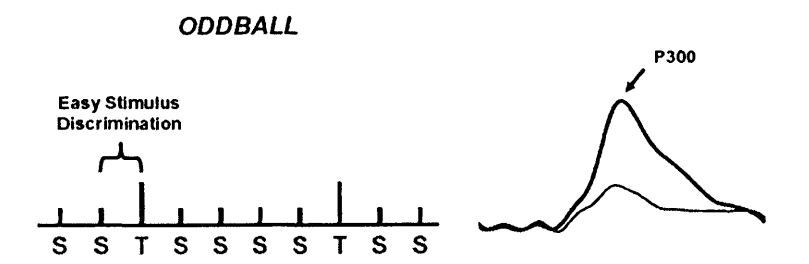


Figure 2.2: Oddball paradigm. Left: auditory sequences in which S refers to frequent tones and T refers to infrequent tones. Right: thick line is the result of averaging for the infrequent tones and thin line for the frequent tones.

The amplitude of P300 is inversely related to the stimulus occurrence probability and directly related to the task difficulty. The latency of P300 correlates to some extent with categorization or evaluation of the stimulus and consequently is related to the task difficulty. Concerning subject parameters, the latency of P300 shows a positive correlation with age and negative correlation with level of attention and vigilance. For more detailed information on P300 the reader may refer to a number of comprehensive reviews [18, 28, 50].

The topography of P300 recorded by surface electrodes shows a maximum over the midline of centro-parietal regions (Pz site). The generator sites of the P300 are not known with certainty, but the available data leads to the conclusion that several cortical and sub-cortical structures contribute to this positive wave [87].

In clinical studies a prolongation of the latency has been reported in dementia [36], Parkinson's disease [105], Huntington's disease [43] as well as in patients with chronic renal failures and head injuries. In addition, a diminution of amplitude has been

reported in schizophrenics [93], in depressed patients, and in chronic alcoholics [17]. Note that many of these findings are restricted to the group of patients and they can not be used to detect individual dysfunctions.

P300 subcomponent

The origin and number of responsible sources of P300 are unknown, however, it is assumed P300 has two subcomponents: P3a and P3b. There is good evidence to believe that P300 subcomponents arise from interactions between frontal and parietal neural sources - P3a is in frontal and P3b is in parietal loci. There is also localization work which justifies this assumption that the P300 data can be modeled accurately by sources placed in anterior and in posterior-parietal cortex [42].

2.3 Magnetoencephalogram and its Comparison with EEG

MEG is an imaging technique used to measure the magnetic fields produced by electrical activity in the brain via extremely sensitive devices such as super conducting quantum interference devices (SQUIDs). These measurements are commonly used in both research and clinical settings. There are many uses for the MEG, including assisting surgeons in localizing a pathology, assisting researchers in determining the function of various parts of the brain, neuro-feedback, and many others.

Although EEG and MEG are generated by the same neurophysiologic processes, there are important differences concerning the neurogenesis of MEG and EEG [17]. In contrast to electric fields, magnetic fields are less distorted by the resistivity of

the skull and scalp, which results in a better spatial resolution of the MEG. As electric and magnetic fields are oriented perpendicular to each other, the directions of highest sensitivity, usually the directions of the field maxima, are orthogonal to each other. Whereas scalp EEG is more sensitive to radial than tangential components of a current source in a spherical volume conductor, MEG detects only its tangential components. This shows that MEG selectively measures the activity in the sulci, whereas scalp EEG measures activity both in the sulci and at the top of the cortical gyri but appears to be dominated by radial sources.

Scalp EEG is sensitive to extracellular volume currents produced by postsynaptic potentials, MEG primarily detects intracellular currents associated with these synaptic potentials because the field components generated by volume currents tend to cancel out in a spherical volume conductor [7]. The decay of magnetic fields as a function of distance is more pronounced than for electric fields. MEG is therefore more sensitive to superficial cortical activity, which should be useful for the study of neocortical epilepsy. Finally, MEG is reference-free which is in contrast to scalp EEG where an active reference can lead to serious difficulties in the interpretation of the data.

Despite the above differences between EEG and MEG data, the mathematical formulation of both data provided in this thesis is the same, and the proposed method can similarly be applied to both data. Throughout this thesis, therefore, E/MEG abbreviation which stands for both EEG and MEG data is used. Depending on the application, however, the proposed methods are applied either to the real EEG or MEG data.

Chapter 3

Single Trial Estimation and Dipole Source Localization for E/MEG: a Literature Survey

This chapter is devoted to the literature survey of two major approaches for E/MEG signal processing. The first approach is single trial estimation and the next is dipole source localization. In addition, in Section 3.3 mathematical theory of KF and PF, as the foundations of proposed approaches in the following chapters, are presented. Throughout this thesis, plain italics indicate scalars, lowercase boldface italics indicate vectors, uppercase boldface indicates matrices and tiled uppercase boldface indicates higher order matrices.

3.1 Single Trial Estimation of ERPs

Conventional methods for analyzing ERPs typically involve time-locked averaging over many trials. The assumption underlying this approach is that the background EEG as a random process is attenuated by averaging, if the results of averaging is to be an accurate reflection of the activity elicited on individual trials, the positive- and negative-going ERP modulations (components) for all the trials must have the same onset latencies, durations, and amplitudes. Recent studies have indicated that there is single-trial variability in ERPs due to environmental and cognitive factors that might include fatigue, habituation, and changes in levels of attention [51]. These factors are of course not mutually exclusive, but the key point here is that the ST-ERP enables capturing the changes in the signals of interest due to neurophysiological changes, which are lost when using conventionally averaged measures. Therefore, researchers in the signal processing community have proposed a number of mathematical methods to extract the ERP information as much as possible. The proposed approaches for detection of ERP parameters (basically amplitude and latency) can generally be categorized into single- and multi-channel based methods. In the following sections an overview of major approaches in each category is presented.

3.1.1 Single-Channel Single Trial Estimation

There are numerous studies reporting approaches in the past three decades for ERP detection and tracking using only one channel. Several of these approaches are categorized below based on the models used in their estimation.

The simplest model for the ERP can be

$$\mathbf{y}_k = \mathbf{s}_k + \mathbf{v}_k \tag{3.1}$$

where \mathbf{y}_k and \mathbf{s}_k are the measured EEG and the ERP at the kth trial, respectively, and \mathbf{v}_k is the additive noise. If it is assumed that \mathbf{s}_k remains constant from trial to trial and the noise \mathbf{v}_k is Gaussian zero mean, the result of ensemble averaging of \mathbf{y}_k over a number of trials is an optimum solution for \mathbf{s}_k and also can be considered as the ML estimation. However, in the laboratory environment, \mathbf{v}_k is generally the background EEG which is a non-stationary and non-Gaussian noise.

Pioneering studies such as [70] employed a time-invariant linear minimum mean squared error filter to estimate s_k in equation (3.1) based on the auto- and cross-covariance values of the background EEG (as noise) and ERPs (as signals of interest). Time-varying [122] and Wiener [13] filtering are the other approaches that have been widely utilized. The fundamental problem in these methods, however, is obtaining an estimator for the cross-covariance matrix between the data s_k and the noise v_k . Another intensively studied technique for estimation of s_k based on equation (3.1) is adaptive filtering. Most attention has been paid to the use of least mean square (LMS) algorithm in the filtering problem (e.g. [14] and [106]).

The pitfall of such approaches, however, lies in considering the ERP signal as a stationary process: ERPs are superpositions of transient responses with changing temporal and spectral components.

The next model for ERP is

$$\mathbf{y}_k = \mathbf{s}(t + \tau_k) + \mathbf{v}_k \tag{3.2}$$

Here only the latency τ_k is varying and shape of ERPs are constant. Equation (3.2) is the most utilized model in analyzing ERPs after the model in equation (3.1).

Peak picking [9] is a straightforward method for finding the latency variability (jitter). This method simply looks for the largest positive peak in the ERP component time interval in the lowpass filtered trials. The latency of this peak is then considered to be the single-trial latency.

A well-known approach for ST-ERP estimation based on equation (3.2) has been proposed by Woody [118]. His approach was to cross correlate a predetermined template against a sequence of samples of the response in order to estimate the signal latency. The individual responses were then corrected for their average latency variations and an average response computed. The Woody technique results in an average signal which is obtained by removing the estimated latency variation before averaging. Although this method of analysis represents a significant step forward over conventional averaging, some information inherent in the signal, such as independent shifts in latency and amplitude in the components of the individual responses are still buried in the noise.

Similarly, in [86] the ML estimator of the model in equation (3.2) in the frequency domain was formulated yielding estimators for latency variability.

In [48] the performances of the above three methods ([9, 118, 86]) as well as an extension of the latter method were studied. Performance of all methods critically depended on the signal-to-noise ratio, however, there was some advantage for the more sophisticated methods (particularly [86] and its extension), when signal-to-noise ratios were in the realistic range.

In the next model ERPs have invariant shapes, while their latencies and amplitudes can vary across trials. These assumptions results

$$\mathbf{y}_k = a_k \mathbf{s}(t + \tau_k) + \mathbf{v}_k \tag{3.3}$$

where a_k is the amplitude of ERP component at the kth trial. The ML estimation of this equation has been given in [47]. A restriction of this paper is that it is based on the assumption of uncorrelated background noise, whereas it is known for instance that the alpha rhythm is both temporally and spatially correlated over channels (e.g. [80] and [81]). Moreover, in [107], Truccolo et al. demonstrate that neglecting trial-to-trial shape variations results in an estimate of the background noise of which the variance is non-stationary over the time interval of interest.

In the next model the ERP at each trial is assumed to be superimposed of several components:

$$\mathbf{y}_k = \sum_{i=1}^q a_{i,k} \mathbf{s}(t + \tau_{i,k}) + \mathbf{v}_k$$
 (3.4)

where q is the number of components. Each component is assumed to have a trial-invariant waveform, but a trial-dependent amplitude scaling factors and latency shifts. A maximum a posteriori (MAP) solution of such a multi-component ERP model via an iterative algorithm is presented in [108]. The method is called differentially variable component analysis (dVCA). The dVCA method is implemented in the time domain and due to the matched-filtering operation in the method, the white noise assumption may affect the performance of the estimator.

The frequency-domain solution of the dVCA method has been carried out in [119]. The ongoing activity is herein assumed to be an autoregressive (AR) random process.

This assumption reduces the number of unknowns significantly and in contrast to the dVCA solution, the resulting ML estimator provides a certain solution.

There are several other studies which consider a linear observation model for ERP as:

$$\mathbf{y}_k = \mathbf{H}\boldsymbol{\theta}_k + \mathbf{v}_k \tag{3.5}$$

This model connects the vector of sampled measurements \mathbf{y}_k with the parameters $\boldsymbol{\theta}_k$ and the measurement errors \mathbf{v} . \mathbf{H} is a matrix that does not contain parameters to be estimated and should be selected a priori. With a linear observation model the choice of the observation matrix \mathbf{H} has a significant role in ST-ERP estimation. For instance, to consider accurately any nonlinear part of the model such as latency may considerably increase the size of \mathbf{H} .

A Bayesian approach for realizing a robust estimator for parameters of equation (3.5) has been carried out in [53]. In this approach, using subspace regularization, the second-order statistical information extracted from a set of measured potentials was used to represent a priori knowledge in the estimation procedure. It was shown that, using this approach, the latencies of some ERP peaks can be estimated accurately. This approach does not, however, yield reliable estimates of peak amplitudes, mainly due to unpredictable fluctuations of the background EEG.

KF has also been employed for estimation of the ERPs based on equation (3.5) in [34]. One of the main advantages of the proposed method is considering the non-stationarity of ERPs from trial to trial. The method uses, however, a trivial model assuming that **H** is an identity matrix. Furthermore, the method utilizes the entire trial as the input to the filter and this high dimensional input would impair the performance of the filter. Likewise, Kalman smoothing has been applied to ST-ERP

and the results compared with those of the conventional averaging method in [76].

Other techniques employed for ST-ERP estimation include parametric methods [59, 60], clustering analysis [38], matching pursuit [121], matched filtering [19, 94], and wavelet transforms [8, 68, 90].

It is noteworthy that all these techniques focus solely on characterizing the temporal trial to trial signal variability and ignore spatial information whereby inefficient and less accurate estimates are achieved.

3.1.2 Multichannel Single Trial Estimation

Some of the approaches explained in the previous section for single channel have been extended to multichannel measurements. For instance, a multichannel extension of ML estimator [47] for the model in equation (3.3) was applied in [22], where the ongoing brain activity was modeled with a stationary autoregressive (AR) time series. The estimator accounts for spatially and temporally correlated background noise that is superimposed on the brain responses.

Furthermore, a multichannel extension of the dVCA method for the multiple component model (equation (3.4)) has recently appeared in [57]. Multichannel subspace regularization [53] given for equation (3.5) has also been carried out in [91].

Other multichannel estimation of ERP includes principal component analysis (PCA) methods [3, 15]. It is evident that the performances of these methods are somehow limited by some signal source properties such as stationarity and these methods are also unable to retain their performance when the SNR is low.

ICA based methods [52, 61, 94] have also been widely exploited in ERP extraction [95]. These approaches, however, assume that the EEG sources are independent,

which can be well violated in presence of intrinsic correlated noise sources.

Another important approach for single trial estimation is considering the spatiotemporal information of ERP data. Several methods have been devoted to this idea by modeling the ERP sources using the ECD model:

$$\mathbf{Y}_{k} = \sum_{i=1}^{q} \mathbf{H}(\rho_{k,i}) \mathbf{M}_{k,i}(\boldsymbol{\rho}_{k,i}) + \mathbf{N}_{k}$$
(3.6)

where $\rho_{k,i}$ and $\mathbf{M}_{k,i}$ are the location and moments of the *i*th ECD at the *k*th trial, respectively. \mathbf{N}_k is the spatiotemporal additive noise at the *k*th trial. Moment is a matrix that shows the strength and orientation of the ECD in three dimensional space for each trial.

In [23] and [97] spatiotemporal measurements are incorporated in a spherical head model using the ECD model in equation (3.6). The dipoles are assumed to have fixed locations and orientations, whereas their strengths are allowed to change in time according to either a parametric [97] or nonparametric [23] model. In [98] only the dipole position is fixed, and the orientation and strength are allowed to vary in time according to a parametric model. A method is also presented in [27] for spatially correlated noise between the sensors with unknown spatial covariances. Similar to this approach, a method was presented in [80], in which the noise covariance and the dipole parameters are estimated separately.

The main drawback of all of these spatiotemporal methods is that the dipole locations are assumed to remain the same during the course of recording. In Chapter 7, a method that can estimate and track both the dipole moments and locations from trial to trial is proposed.

3.2 E/MEG Dipole Source Localization

Scalp-recorded E/MEGs suffer from relatively poor spatial resolution. The poor spatial resolution motivates research into proposing methods that can localize accurately the E/MEG sources. One strategy in source localization is distributed or tomographic source localization. In this method, the brain is divided into a number of small grid cells and the likely E/MEG activity for each grid cell is constructed. Since the number of unknown parameters is likely to be higher than the number of known measurements, the distributed source localization is generally an ill-posed and underdetermined problem. A popular strategy to overcome this problem is dipole source localization, which assumes that one or multiple current dipoles represent the sources. Physiologically, this assumption may not be strictly true, but this approach leads to an over-determined problem.

Dipole source localization is a difficult endeavor because of the nonlinear nature of the localization, (typically) a very low SNR for the E/MEG, and also the fact that the noise is spatially colored as well as temporally non-stationary. In the following, several approaches for the localization of scalp-recorded E/MEG are briefly reviewed and their strengths and weaknesses are highlighted. This review provides the background for key elements of the new approaches that are developed in the next chapters. Here, the methods proposed for tomographic source localization are ignored, and only the dipole source localization methods are reviewed. Readers may refer to reviews in [6] and [71] for details of several methods proposed for tomographic source localization.

In the presence of measurement errors, the forward model may be represented as $\mathbf{y}_t = \sum_{i=1}^q \mathbf{H}(\boldsymbol{\rho}_t) \mathbf{m}_t(\boldsymbol{\rho}_t) + \mathbf{v}_t$, where \mathbf{y}_t is the multichannel measurement at time t, \mathbf{H} is the forward matrix, and \mathbf{v} is the spatiotemporal noise. The goal is to estimate

the current dipoles responsible for the scalp-recorded activity in terms of their threedimensional locations ρ_t and moments \mathbf{m}_t at time sample t.

This problem is clearly a nonlinear minimization problem and the dipole locations (nonlinear part) can be found iteratively based on gradient descent algorithms. This technique, which is integrated in the brain electrical source analysis (BESA) [96] software, is the most commonly used method for localizing E/MEG sources [65]. A general risk of these methods is that they can be trapped in undesirable local minima, resulting in the algorithm accepting a certain wrong location. The complexity of the directed search algorithms and the problem of local minima both increase with the number of dipoles. Thus, the maximum number of independent sources which can be reliably localized for a given time point is lower than what would be in reality. To overcome this problem, the parameters of a multi dipole model can be reliably and conveniently estimated using global optimization methods, which do not require initial estimates for the source locations. For instance, dipole fitting using simulated annealing has been presented in [35, 39], and using clustering and genetic algorithms has been carried out and compared in [109]. These techniques, however, do not necessarily obtain the global location maxima inside the head. The alternative grid based techniques described below avoid such problems and give dipole locations inside the head. In the grid based method, the brain is divided into sufficiently small grid cells and each grid cell is scanned to find the possible sources in a region of interest which can range from a small location to the whole brain volume.

A simple grid based method that has been described in [41] and [54] is least-squares fit, which computes the moments of each grid cell based on the Moore-Penrose pseudo-inverse. The computed moment is used to construct a likelihood criterion based on the

available measurements. These methods can either be applied to a single snapshot or a block of time samples. When applied sequentially to a set of individual time slices, the result can be used for moving and unconstrained dipole locations [117]. Alternatively, by using the entire block of data in the least-squares fit, the dipole locations can be fixed over the entire interval [97]. The fixed and moving dipole models have each proven useful in E/MEG and remain the most widely used approach to processing experimental and clinical data.

Another grid based technique which is well known in the E/MEG dipole source localization field is based on multiple signal classification (MUSIC) [79]. This technique provides suboptimal estimates using singular value decomposition (SVD) for multiple dipole locations by using a three-dimensional search. Recursively applied and projected MUSIC (RAP-MUSIC) [78] is an improvement to the MUSIC method. RAP-MUSIC deflates those sources that have already been identified by projecting the signal subspace away from the gain vectors corresponding to those sources¹. RAP-MUSIC assumes, however, that the signal subspaces are completely independent. This is the main drawback of the method. Fine principal vector (FINE) [120] is another extension of the MUSIC algorithm which employs projections onto a subspace that is spanned by a small set of particular vectors (the FINE vector set) in the estimated noise-only subspace (or the signal subspace) instead of the entire estimated signal subspace. The FINE vector set is identified as an intersection set between the signal subspace and the subspace that is spanned by the array manifold of a specific region surrounding the scanned point. The FINE approach is able to enhance spatial resolution and localization accuracy (relative to MUSIC and RAP-MUSIC) for closely

¹For more details reader may refer to Chapter 6.

spaced neural sources [26].

It has been shown that a class of adaptive spatial filters known as beamformers has the best spatial resolution and performance amongst existing methods [21]. BF falls within array processing methods and has been used widely in communications and radar signal processing applications [110]. BF - its application for E/MEG dipole source localization is presented in [111] - provides an adaptive method which places nulls, using some linear constraints, at positions corresponding to the noise sources². The transient and often correlated nature of the neural activation in different parts of the brain often, however, limits the BF performance. Since E/MEG has variable sensitivity to source locations, the noise gain of the filter varies as a function of location. One strategy to account for this effect is to normalize the output power of BF with respect to the estimated power in the presence of noise only [92]. BF is robust to moderate source correlations, but sources that are strongly correlated are poorly resolved [6]. A modified beamformer method that circumvents these shortcomings by suppressing the activations from regions with interfering coherent sources has been proposed in [20, 46]. Modification of the source model has also been employed for reconstruction of correlated sources in [10]. Beamspace transformations for dimension reduction, which preserve source activity located within a given region of interest, have also been presented in [37].

A non-stationary Bayesian filtering method (particle filtering: PF) is a recent development in dipole source localization [101]. PF is an emerging methodology and is particularly useful for dealing with nonlinearity and non-stationarity of E/MEG data [29]. The main disadvantage of PF is the computational cost and the required

²Mathematical details of this approach has been given in Chapter 5.

memory which are exponentially related to the number of dipoles. In Chapter 6, a method based on the Rao-Blackwellized particle filter (RBPF), which effectively overcomes this problem, is introduced.

In several simulation and experimental studies, the importance of a priori knowledge about the number and possible locations of the sources has been discussed [1, 31, 72]. Thus, a key question that has to be answered is how to obtain a correct estimate of the number of sources. Often, this choice is based on the physiological knowledge [11, 30]. Several other studies have proposed to define the number of dipoles based on other functional imaging data such as PET or fMRI [49, 33, 58]. However, this is not without risk given that the relationship between hemodynamic changes measured with fMRI and the electrophysiological changes measured with E/MEG is not yet well understood [25, 64]. A third alternative for defining the number of active sources is to use the available mathematical approaches that aim to identify the optimal number of dipoles over a given data period automatically [115, 116].

In the following sections, KF and PF as the cores of the approaches presented in the subsequent chapters are described in more detail.

3.3 Fundamentals of KF and PF

Bayesian filtering methods, especially KF and PF, are fundamental approaches for several new directions in the current study. In this section an introduction to them is presented. First, a description of nonlinear tracking problem in state space is illustrated. The optimal solution to this problem is often intractable, and only when certain constraints are held, a solution can be given. The KF defined in Section 3.3.2 is such a solution when the state space is linear, and PF outlined in Section 3.3.3 is

another solution when the state space is nonlinear.

3.3.1 Problem Formulation in State Space

Suppose that the sequence $\mathbf{y}_{1:t} = \{\mathbf{y}_i, i = 1, ..., t\}$ is the observation of the system at time 1, 2, ..., t, and $\{\mathbf{x}_t, t \in \mathbb{N}\}$ is the state of the system at time t. The state \mathbf{x}_t is assumed to be Markovain process for which the new state is only subject to the previous state. Hence, the evolution of the state and the relation between the state and the observation are, respectively, given by:

$$\mathbf{x}_{t} = f_{t-1}(\mathbf{x}_{t-1}, \mathbf{w}_{t-1}) \tag{3.7}$$

$$\mathbf{y}_t = h_t(\mathbf{x}_t, \mathbf{v}_t) \tag{3.8}$$

where f_t and h_t are generally nonlinear functions of the state \mathbf{x}_t , and \mathbf{w}_{t-1} and \mathbf{v}_t are independent and identically distributed (i.i.d.) noise processes.

The aim of filtering is to estimate \mathbf{x}_t based on a set of all available observations $\mathbf{y}_{1:t} = \{\mathbf{y}_i, i = 1, \dots, t\}$ up to time t. By recursive calculation of the posteriori density function $p(\mathbf{x}_t|\mathbf{y}_{1:t})$ of state \mathbf{x}_t , the estimation of the state \mathbf{x}_t can be the expected value of posteriori density as:

$$E\{\mathbf{x}_t\} = \int_{all \ \mathbf{x}_t} \mathbf{x}_t p \mathbf{x}_t p(\mathbf{x}_t | \mathbf{y}_{1:t}) d\mathbf{x}_t.$$

Via Bayes theorem and assuming that the state \mathbf{x}_t and measurements \mathbf{y}_t are Markovain process, an available measurement \mathbf{y}_t at time t is used to recursively update

the posterior density of state [29]:

$$p(\mathbf{x}_t|\mathbf{y}_{1:t}) = \frac{p(\mathbf{y}_t|\mathbf{x}_t)p(\mathbf{x}_t|\mathbf{y}_{1:t-1})}{p(\mathbf{y}_t|\mathbf{y}_{1:t-1})}$$
(3.9)

where $p(\mathbf{x}_t|\mathbf{y}_{1:t-1})$ is computed in the prediction stage using the Chapman-Kolmogorov equation:

$$p(\mathbf{x}_{t}|\mathbf{y}_{1:t-1}) = \int_{all \ \mathbf{x}_{t}} p(\mathbf{x}_{t}|\mathbf{x}_{t-1}) p(\mathbf{x}_{t-1}|\mathbf{y}_{1:t-1}) d\mathbf{x}_{t-1}$$
(3.10)

and $p(\mathbf{y}_t|\mathbf{y}_{1:t-1})$ is a normalizing constant and depends only on the measurement model (3.8) and the statistics of the noise \mathbf{v}_t :

$$p(\mathbf{y}_t|\mathbf{y}_{1:t-1}) = \int_{all \ \mathbf{x}_t} p(\mathbf{y}_t|\mathbf{x}_{1:t}) p(\mathbf{x}_t|\mathbf{y}_{1:t-1}) d\mathbf{x}_t.$$
(3.11)

Computing these expressions and recursions in many problems is intractable and it is not typically simple to compute the normalizing constant $p(\mathbf{y}_t|\mathbf{y}_{1:t-1})$, the marginal of posterior $p(\mathbf{x}_t|\mathbf{y}_{1:t-1})$ and in particular $p(\mathbf{x}_t|\mathbf{y}_{1:t})$ probabilities. This is because they require the evaluation of high-dimensional complex integrals. To solve this problem, a large number of papers and books have been devoted to obtaining approximations for these distributions [29]. Among different approaches, KF and PF are two major approaches to solve the recursive equations (3.9), (3.10) and (3.11). KF is especially useful for linear systems, and PF has been widely reported as one of the best filters for nonlinear systems. In the following sections these algorithms are briefly reviewed.

3.3.2 Kalman Filtering

In the KF, by making the following assumptions, the posteriori density becomes Gaussian, and only the mean and covariance matrices are calculated in each step.

• f_t and h_t are assumed to be known and linear functions, so equations (3.7) and (3.8), respectively, become:

$$\mathbf{x}_{t} = \mathbf{F}_{t-1} \mathbf{x}_{t-1} + \mathbf{w}_{t-1} \tag{3.12}$$

$$\mathbf{y}_t = \mathbf{H}_t \mathbf{x}_t + \mathbf{v}_t; \tag{3.13}$$

- Random sequences \mathbf{w}_{t-1} and \mathbf{v}_t are assumed to be mutually independent zero mean white Gaussian noises with known covariances \mathbf{Q}_w and \mathbf{Q}_v , respectively;
- Prior distribution p(x₀) = N(x₀; m₀, P₀) (initial distribution) is considered to be Gaussian, where N(x; m, P) refers to a Gaussian distribution of x with mean m and covariance P.

These assumptions cause the resulting distributions to be Gaussian as follows

$$p(\mathbf{x}_{t-1}|\mathbf{y}_{t-1}) = \mathcal{N}(\mathbf{x}_{t-1}; \mathbf{m}_{t-1,t-1}, \mathbf{P}_{t-1,t-1})$$
(3.14)

$$p(\mathbf{x}_t|\mathbf{y}_{t-1}) = \mathcal{N}(\mathbf{x}_t; \mathbf{m}_{t,t-1}, \mathbf{P}_{t,t-1})$$
(3.15)

$$p(\mathbf{x}_t|\mathbf{y}_t) = \mathcal{N}(\mathbf{x}_t; \mathbf{m}_{t,t}, \mathbf{P}_{t,t})$$
(3.16)

where $\mathbf{m}_{i,j}$ and $\mathbf{P}_{i,j}$ are, respectively, the mean and covariance matrix of the conditional pdf $p(\mathbf{x}_i|\mathbf{y}_j)$. Using these assumptions, one can evaluate the optimal linear filtering equations in a closed-form. The above distribution parameters, therefore, can be calculated by the KF prediction and the update steps as:

• Prediction step:

$$\mathbf{m}_{t,t-1} = \mathbf{F}_{t-1} \mathbf{m}_{t-1,t-1} \tag{3.17}$$

$$\mathbf{P}_{t,t-1} = \mathbf{Q}_w + \mathbf{F}_{t-1} \mathbf{P}_{t-1,t-1} \mathbf{F}_{t-1}^T$$
(3.18)

• Update step:

$$\mathbf{m}_{t,t} = \mathbf{m}_{t,t-1} + \mathbf{K}_t(\mathbf{y}_t - \mathbf{H}_t \mathbf{m}_{t,t-1})$$
 (3.19)

$$\mathbf{P}_{t,t} = \mathbf{P}_{t,t-1} - \mathbf{K}_t \mathbf{\Lambda}_t \mathbf{K}_t^T \tag{3.20}$$

where

$$\Lambda_t = \mathbf{H}_t \mathbf{P}_{t,t-1} \mathbf{H}_t^T + \mathbf{Q}_v \tag{3.21}$$

$$\mathbf{K}_{t} = \mathbf{P}_{t,t-1} \mathbf{H}_{t}^{T} \mathbf{H}_{t} \mathbf{S}_{t}^{-1} \tag{3.22}$$

are the covariance of the innovation term $\mathbf{y}_t - \mathbf{H}_t \mathbf{m}_{t,t-1}$ and the Kalman gain, respectively.

In the linear Gaussian environment where the state distribution is Gaussian, KF is an optimal solution. Also, considering any other distribution for states, the KF is the best linear estimator in the presence of Gaussian white noise.

3.3.3 Particle Filters

PF is an emerging and powerful technique for sequential signal processing with a wide range of applications in array processing, target tracking and video processing. In PF, the posterior distributions are approximated by discrete random measures defined by particles $\{\mathbf{x}^{(n)}, n = 1, ..., N\}$ and their associated weights $\{w^{(n)}, n = 1, ..., N\}$. The distribution based on these samples and weights at time t is approximated as:

$$p(\mathbf{x}) \approx \sum_{n=1}^{N} w^{(n)} \delta(\mathbf{x} - \mathbf{x}^{(n)})$$
 (3.23)

where δ is the Dirac delta function. With this approximation, the expectation of function $p(\mathbf{x})$ is

$$E\{\mathbf{x}\} \approx \sum_{n=1}^{N} w^{(n)} p(\mathbf{x}^{(n)}).$$
 (3.24)

If the particles are generated according to the distribution $p(\mathbf{x})$, the weights are the same and equal to 1/N. When generation of the particles by direct sampling from unknown distribution $p(\mathbf{x})$ is impossible, the particles are generated from a known distribution $\pi(\mathbf{x})$ called *importance density*. This concept known as importance sampling results in the following weights [4]:

$$w^{(n)} \propto \frac{p(\mathbf{x}^{(n)})}{\pi(\mathbf{x}^{(n)})} \tag{3.25}$$

Suppose at time t the approximation of the posteriori distribution $p(\mathbf{x}_t|\mathbf{y}_{1:t})$ subject to having $p(\mathbf{x}_{t-1}|\mathbf{y}_{1:t-1})$ is desired. In other words, given the discrete random measure $\{\mathbf{x}_{t-1}^{(n)}, w_{t-1}^{(n)}; n = 1, \dots, N\}$ and the observation \mathbf{y}_t , particles and weights $\{\mathbf{x}_t^{(n)}, w_t^{(n)}; n = 1, \dots, N\}$ should be estimated. If the importance density is chosen such that it can be factorized to

$$\pi(\mathbf{x}_t|\mathbf{y}_{1:t}) = \pi(\mathbf{x}_t|\mathbf{x}_{t-1},\mathbf{y}_{1:t})\pi(\mathbf{x}_{t-1}|\mathbf{y}_{1:t-1})$$
(3.26)

the new samples $\mathbf{x}_t^{(n)}$ can then be generated according to the importance density $\pi(\mathbf{x}_t|\mathbf{x}_{t-1}^{(n)},\mathbf{y}_t)$ which depends on the old samples and the new measurements.

To update the new weights based on old weights, Bayes' rule (3.9) is used to decompose the posterior density:

$$p(\mathbf{x}_{t}|\mathbf{y}_{1:t}) = \frac{p(\mathbf{y}_{t}|\mathbf{x}_{t})p(\mathbf{x}_{t}|\mathbf{y}_{1:t-1})}{p(\mathbf{y}_{t}|\mathbf{y}_{1:t-1})}$$

$$= \frac{p(\mathbf{y}_{t}|\mathbf{x}_{t})p(\mathbf{x}_{t}|\mathbf{x}_{t-1})p(\mathbf{x}_{t-1}|\mathbf{y}_{1:t-1})}{p(\mathbf{y}_{t}|\mathbf{y}_{1:t-1})}$$
(3.27)

and equation (3.25) can be written as

$$w_t^{(n)} \propto \frac{p(\mathbf{x}_t^{(n)}|\mathbf{y}_{1:t})}{\pi(\mathbf{x}_t^{(n)}|\mathbf{y}_{1:t})}$$
 (3.28)

By replacing (3.27) into (3.28) and using (3.26) the new formulation for estimation of weights are shown to be

$$w_{t}^{(n)} \propto \frac{p(\mathbf{y}_{t}|\mathbf{x}_{t}^{(n)})p(\mathbf{x}_{t}^{(n)}|\mathbf{x}_{t-1}^{(n)})}{p(\mathbf{y}_{t}|\mathbf{y}_{1:t-1})\pi(\mathbf{x}_{t}^{(n)}|\mathbf{x}_{t-1}^{(n)},\mathbf{y}_{1:t})} \times \frac{p(\mathbf{x}_{t-1}^{(n)}|\mathbf{y}_{1:t-1})}{\pi(\mathbf{x}_{t-1}^{(n)}|\mathbf{y}_{1:t-1})}$$
(3.29)

Using equation (3.29) and considering the fact that $p(\mathbf{y}_t|\mathbf{y}_{1:t-1})$ is a normalizing constant, the new weights are updated as follows:

$$w_t^{(n)} \propto w_{t-1}^{(n)} \frac{p(\mathbf{y}_t | \mathbf{x}_t^{(n)}) p(\mathbf{x}_t^{(n)} | \mathbf{x}_{t-1}^{(n)})}{\pi(\mathbf{x}_t^{(n)} | \mathbf{x}_{t-1}^{(n)}, \mathbf{y}_{1:t})}$$
(3.30)

and thus, the filtered posterior density $p(\mathbf{x}_t|\mathbf{y}_{1:t})$ can be approximated as:

$$p(\mathbf{x}_t|\mathbf{y}_{1:t}) \approx \sum_{n=1}^{N} w_t^{(n)} \delta(\mathbf{x} - \mathbf{x}_t^{(n)})$$
(3.31)

where the weights are defined in (3.30). It can be shown that as $N \to \infty$, the approximation (3.31) approaches to the true posterior density $p(\mathbf{x}_t|\mathbf{y}_{1:t})$.

Resampling: The importance sampling weights indicate the level of importance of the corresponding particles. A relatively small weight implies that the sample is drawn far from the main body of the posterior distribution and has a small contribution in the final estimation. Such a particle is said to be ineffective. If the number of ineffective particles is increased, the number of particles contributing to the estimation of states is decreased, so the performance of the filtering procedure deteriorates. This problem can be avoided by a resampling procedure. Resampling is a scheme that eliminates the particles with small weights and replicates those with large weights. Therefore, at the end of resampling, all weights are equal to 1/N and the number of each particle denotes the importance of that particle.

A direct implementation of resampling would consist of generating N_s i.i.d. variables from the uniform distribution, computing the normalized cumulative sum of them, and comparing them with the cumulative sum of normalized weights. In each step, if the cumulative sum of normalized weights is bigger than the cumulative sum of N_s i.i.d. variables, a particle is produced.

Resampling can be involved in every fixed number of iterations (e.g. at each or every five steps of iterations) or it can be conducted dynamically [63]. In the dynamic method, an effective sample size is used to monitor the variation of the importance weights of the particles, and consequently the need for resampling.

In the following sections, sampling importance resampling PF (SIR-PF), which is an important version of PF, is explained. SIR has been used throughout this thesis and for convenience, PF is used instead of SIR-PF.

SIR particle filter

The choice of importance density is one of the most crucial issues in the design of PF and plays a significant role in its performance. This function must have the same support as the probability distribution to be approximated. In general, the closer the importance density to the actual density, the better the approximation is. The most popular choice of the importance density is given by

$$\pi(\mathbf{x}_t|\mathbf{x}_{t-1}^{(n)},\mathbf{y}_{1:t}) = p(\mathbf{x}_t|\mathbf{x}_{t-1}^{(n)})$$
(3.32)

This choice results in SIR-PF which implies sampling from $p(\mathbf{x}_t|\mathbf{x}_{t-1}^{(n)})$. A sample can be obtained by generating a noise sample $\mathbf{w}_{t-1}^{(n)} \sim \mathcal{N}(\mathbf{0}, \mathbf{Q}_w)$ and setting $\mathbf{x}_t^{(n)} = f_{t-1}(\mathbf{x}_{t-1}^{(n)}, \mathbf{w}_{t-1}^{(n)})$. This choice of importance density implies that the particle weights in equation (3.30) can be updated by:

$$w_t^{(n)} \propto w_{t-1}^{(n)} p(\mathbf{y}_t | \mathbf{x}_t^{(n)})$$
 (3.33)

where $p(\mathbf{y}_t|\mathbf{x}_t^{(n)})$ is the likelihood function and depends on the measurement noise distribution.

In PF sampling from $p(\mathbf{x}_t|\mathbf{x}_{t-1}^{(n)})$ is needed and a sample can be obtained by generating the noise sample $\mathbf{w}_{t-1}^{(n)} \sim \mathcal{N}(\mathbf{0}, \mathbf{Q}_w)$ and setting $\mathbf{x}_t^{(n)} = f_{t-1}(\mathbf{x}_{t-1}^{(n)}, \mathbf{w}_{t-1}^{(n)})$. Here, $\mathcal{N}(\mathbf{0}, \mathbf{Q}_w)$ is a zero mean Gaussian distribution with covariance matrix \mathbf{Q}_w .

The importance density in PF is independent of the measurement and the state space is explored without any knowledge of the observations. This filter, therefore, can be inefficient and sensitive to outliers. However, PF does have the advantage that the weights are easily evaluated and the importance density can be easily sampled.

Chapter 4

State Space Approaches for Single Trial Estimation of ERPs

4.1 Introduction

The objective in this chapter is to develop a reliable ST-ERP estimation method to detect and illustrate ERP amplitude and latency variability during the course of a recording session. The proposed method is based on PF whereby the approximate wavelet coefficients of ERPS are estimated recursively. The results of the proposed method in the same framework is compared to that of the method in which KF is employed as an estimator. Empirically, as will be discussed later, if a sufficient number of particles is chosen, PF outperforms KF. PF also is a sequential method and can track variability of trials (as can KF), which represents an advantage over some other methods, in particular ML, ICA and DWT. However, in comparison with other methods, such as ICA, PF does not use the spatial information, and compared to MAP estimation, PF does not use any prior knowledge about the measurements

and may be sensitive to the outliers.

This chapter is organized as follows. First, the ST-ERP estimation in the state space is formulated. KF and PF, which were explained in Chapter 3, are recursive solutions to this problem. In Section 4.3, the results are presented and the performance of the PF and KF methods are compared. Section 4.4 concludes the chapter.

4.2 Problem Formulation in State Space

The performance of estimators (PF and KF) in the state space is highly influenced by the dimension of the hidden state vector \mathbf{x} . In order to reduce this dimension, one could use DWT, which decomposes the signal into high (detail) and low (approximation) frequency contained coefficients by incorporating a set of predefined wavelets [69]. Considering that ERPs have relatively low frequency spectral components with different temporal localizations, DWT has been recommended for denoising and dimension reduction in [67]. Therefore, let m approximation wavelet coefficients of time locked measured ERPs in the kth ($k \in \mathbb{N}$) trial be

$$\mathbf{y}_k = [y_k(1) \quad y_k(2) \quad \dots \quad y_k(m)]^T \tag{4.1}$$

where $[.]^T$ denotes the transpose operation. By modeling the wavelet coefficients in the state space, the evolution of the state \mathbf{x}_k and the relations between the states and the measurements (wavelet coefficients of the measurement) are respectively given by

$$\mathbf{x}_{k} = f_{k-1}(\mathbf{x}_{k-1}, \mathbf{w}_{k-1}) \tag{4.2}$$

$$\mathbf{y}_k = h_k(\mathbf{x}_k, \mathbf{v}_k) \tag{4.3}$$

where f_k and h_k are general functions, and \mathbf{v}_k are assumed to be zero mean GWN with known covariance matrices \mathbf{Q}_w and \mathbf{Q}_v , respectively.

A widely used model for ERP estimation is the linear additive noise model. The measurement equation (4.3) is then assumed to be of the form

$$\mathbf{y}_k = \mathbf{x}_k + \mathbf{v}_k \tag{4.4}$$

where the state \mathbf{x}_k corresponds to the approximation of the wavelet coefficients of the activity that is related to the measured ERPs. The noise \mathbf{v}_k can be either assumed as GWN or the background EEG independently distributed from the ERPs. The purpose is to estimate \mathbf{x}_k based on a set of available measurements $\mathbf{y}_{1:k} = \{\mathbf{y}_i, i = 1, \ldots, k\}$, up to kth trial. Thus, one can estimate the posteriori density function $p(\mathbf{x}_k|\mathbf{y}_{1:k})$ of state \mathbf{x}_k , and the estimation of state \mathbf{x}_k will be the expected value of the posteriori density. Via the Bayes rule, the available measurements \mathbf{y}_k are used to update the posterior density as

$$p(\mathbf{x}_k|\mathbf{y}_{1:k}) = \frac{p(\mathbf{y}_k|\mathbf{x}_k)p(\mathbf{x}_k|\mathbf{x}_{k-1})}{p(\mathbf{y}_k|\mathbf{y}_{1:k-1})}p(\mathbf{x}_{k-1}|\mathbf{y}_{1:k-1}). \tag{4.5}$$

Therefore the approximate wavelet coefficients of ERPs, which have been smoothed by zeroing the detail coefficients, are sequentially estimated. ERPs are then reconstructed by taking the inverse wavelet transform of the estimated approximate wavelet coefficients.

Since the transition from $p(\mathbf{x}_{k-1}|\mathbf{y}_{1:k-1})$ to $p(\mathbf{x}_k|\mathbf{y}_{1:k})$ is often analytically intractable, as mentioned in Chapter 3, KF and PF are two major approaches to solve

Algorithm 1 Pseudocode for particle filtering

Set k = 0 and generate random numbers $\mathbf{x}_0^{(n)}$ according to a random uniform distribution.

for k = 1 to T do $\{T \text{ is the number of trials}\}$

- Generate random numbers $\mathbf{w}_k^{(n)} \sim \mathcal{N}(\mathbf{0}, \mathbf{Q}_w)$ and set $\tilde{\mathbf{x}}_k^{(n)} = f(\mathbf{x}_{k-1}^{(n)}, \mathbf{w}_k^{(n)})$.
- Update new weights $w_k^{(n)} = \mathcal{N}(\mathbf{y}_k | \tilde{\mathbf{x}}_k^{(n)}, \mathbf{Q}_v)$.
 Normalize the weights $\sum_{n=1}^{N} w_k^{(n)} = 1$.
- Resample new N particles $\mathbf{x}_{k}^{(n)}$ from the $\tilde{\mathbf{x}}_{k}^{(n)}$ with replacement according to the importance weights $w_{k}^{(n)}$ (see text).
- $Set \ w_k^{(n)} = rac{1}{N}$. end for

In Algorithm 1, the pseudo-code of the PF for ST-ERP estimation is presented. Note that due to the resampling involved in each step of filtering, equation 3.33 is reduced to $w_k^{(n)} = p(\mathbf{y}_k | \mathbf{x}_k^{(n)})$. Since the measurement noise \mathbf{v}_k is zero mean GWN, the weights can be updated readily as $w_k^{(n)} = \mathcal{N}(\mathbf{y}_k|\mathbf{x}_k^{(n)},\mathbf{Q}_v)$, where $\mathcal{N}(\mathbf{a}|\boldsymbol{\mu},\mathbf{Q})$ denotes the Gaussian density function with mean vector μ and covariance matrix \mathbf{Q} , evaluated at a.

Experiments and Results 4.3

In this section, comparisons between PF and KF for simulated ERPs are given first. Then the results of applying both algorithms to real EEG measurements obtained in an *odd-ball* paradigm are reported.

4.3.1 Simulation Results

To generate a set of synthetic EEG data an approach similar to that introduced in [34] is employed. The simulated EEGs contained ERP components in the interval between 0.2sec and 0.5sec post-stimulus. The sampling frequency and the number of trials were respectively set to 250 Hz and 60. These values were chosen in order to match those for the real EEG data set to which the approach was applied subsequently. Two Gaussian functions (one positive and one negative) were used to simulate the ERPs. The amplitude, mean and variance of Gaussian functions represent the amplitude, latency, and width of the ERP components, respectively. The amplitude and latency of the positive peak were modeled to respectively decrease and increase linearly during the course of recording from trial to trial. GWN with different levels was added to both the amplitudes and the latencies. The amplitude and latency of the negative peak were assumed to vary according to a uniform random distribution which causes to have independent fluctuations from trial to trial. The widths of both positive and negative peaks were constant from trial to trial, however some normally distributed random variations were added to them.

For better assessment of the proposed algorithms, the GWN and real background EEG activities were considered as two different types of random noise. Hence, the signal-to-noise ratio (SNR) and the signal-to-background ratio (SBR) is defined as follows:

$$SNR = 10 \log \frac{P_{signal}}{P_{GWN}} \tag{4.6}$$

$$SNR = 10 \log \frac{P_{signal}}{P_{GWN}}$$

$$SBR = 10 \log \frac{P_{signal}}{P_{background}}$$

$$(4.6)$$

where P denotes the power of its subscript argument. The SNR represents the ratio

of the strength of the simulated ERPs to that of the added GWN. The SBR is the ratio of the strength of the desired signal to the added background EEG. Due to the non-Gaussian nature and non-stationarity of the EEGs, SBR is expected to serve as a realistic criterion. The performance of the algorithms in the presence of each source of noise separately will be discussed later.

The Daubechies-5 wavelet was chosen for its simplicity and general purpose applicability in a variety of time frequency representation problems [88]. Three wavelet decomposition levels empirically are found to be appropriate for synthetic and real data sets. In both algorithms, the covariance matrices for \mathbf{w}_{k-1} and \mathbf{v}_k in the KF were as $\mathbf{Q}_w = \sigma_w \mathbf{I}$ and $\mathbf{Q}_v = \sigma_v \mathbf{I}$, and in the PF were as $\mathbf{Q}_w = q_w \mathbf{I}$ and $\mathbf{Q}_v = q_v \mathbf{I}$, respectively (I is the identity matrix). σ_w , σ_v , q_w , q_v are free parameters which are adjusted experimentally. These parameters determine the performance of the estimator by a trade-off between the estimator's sensitivity and stability or by a trade-off between noise suppression and signal tracking. In the KF, only the σ_v/σ_w ratio is important, thus $\sigma_w = 0.1$ was chosen for computational convenience. In the PF q_v and q_w play different roles and their appropriate combinations can further reduce the error. The error is defined as the mean square error between the simulated and estimated ERPs. In this study, q_w was fixed to 5 and only q_v was adjusted. q_w also was fixed to simplify the search for the best set of values that optimizes the criterion. Note that the performance of the method is better when both q_v and q_w are tuned than when q_w is fixed.

The number of particles in the PF approach was set to 10000. Decreasing the number of particles deteriorates the performance of the PF, and increasing the number of particles causes the computational cost to increase. The computational complexity

of the PF is dependent on the number of particles, the number of trials and the number of samples in each trial. In contrast, the computational complexity of the KF is an order of the number of trials, and the number of samples in each trial. Therefore, the degree to which PF is slower than KF is approximately proportional to the number of particles. Both methods, however, can be applied successfully in real time processing (online) applications.

Fig. 4.1 shows a typical example for the simulated ERPs and their estimations using KF and PF methods. Fig. 4.1(a) depicts the superposition of noiseless ERPs in which the amplitude of the first peak increases while its latency decreases linearly. Fig. 4.1(b) shows the noisy ERPs (simulated EEG) when GWN and background EEG are added to the noiseless ERPs with SNR = -5dB and SBR = -10dB. Fig. 4.1(c) and Fig. 4.1 (d) show the ERPs extracted from the noisy data using KF and PF methods, respectively. The morphological features extracted by the PF were closer to the original noise-free ERPs than those extracted by the KF. For instance, notice the increase in signal fluctuations in the KF method around 0.25sec. In Fig. 4.2, three ST estimations for trial numbers 5, 35 and 55 are shown. Figures 4.2(a), (c) and (e) demonstrate three different noiseless (thick line) and noisy (solid line) simulated ERPs. The figures show that the ERPs are highly contaminated by the two sources of noise (SNR = -5dB and SBR = -10dB). Figures 4.2(b), (d) and (f) show the results of ST estimation of the noisy ERPs using the PF (solid line) and the KF (dashed line) methods. The PF presents more accurate estimates for the peaks and troughs of the noiseless ERP patterns (thick line) than the KF.

Since neurophysiologists are primarily interested in peak parameters (amplitude and latency) here these features are carefully modeled in the synthetic ERP data.

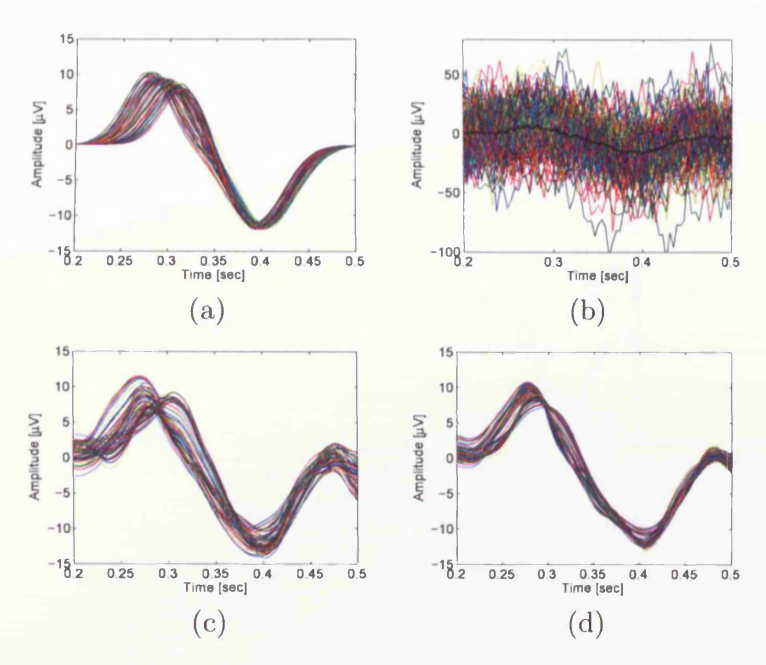


Figure 4.1: Superposition of simulated ERPs and their ST estimations SNR = -5dB and SBR = -10dB; (a) simulated ERPs, (b) noisy ERPs (average in thick black line), (c) extracted ERPs using the KF method, and (d) extracted ERPs using the PF method. Notice that the PF estimates the ERPs very closely with respect to the original ERPs shown in (a).

The results shown in Fig. 4.3 and Fig. 4.4 have been obtained by analysis of a set of synthetic data. Other simulations attained comparable or better results. Fig. 4.3 demonstrates the true and estimated values of amplitude and latency on a trial-by-trial basis. Fig. 4.3(a) shows the amplitude of the positive peak for the simulated (thick line) and the estimated amplitudes using the PF and KF methods (solid and dashed lines respectively). The errors, which are the absolute value of the difference between noiseless and estimated amplitudes in each trial are plotted in Fig. 4.3(c). The mean and variance of errors are plotted in a bar graph in Fig. 4.3(d), which

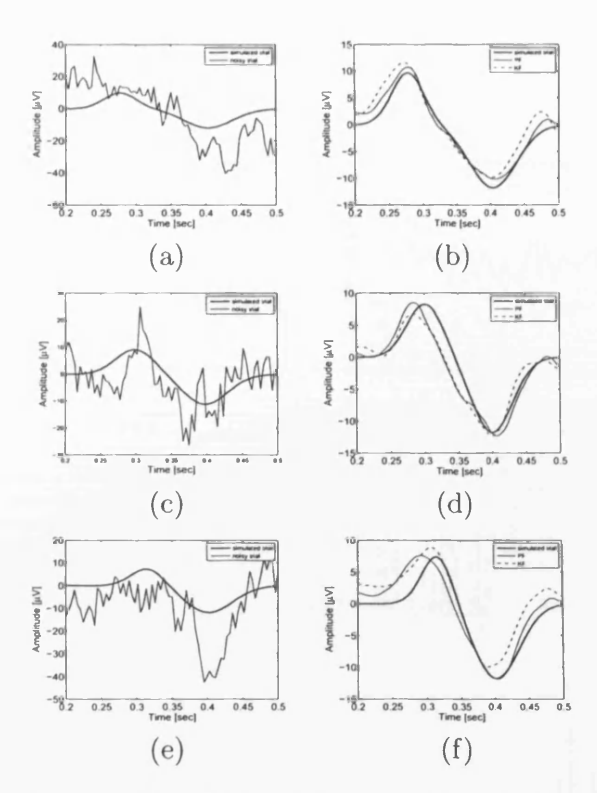


Figure 4.2: Three examples for ST estimation SNR = -5dB and SBR = -10dB; (a) simulated EEG and ERP for trial number 5, (b) simulated and estimated ERPs using PF and KF methods for trial number 5, (c) and (d) show the results for trial number 35, while (e) and (f) demonstrate the estimates for trial number 55.

shows that the PF has statistically better performance (p < 0.001). Figs. 4.3(b) and (e) depict the estimated amplitude and the estimated errors for the negative peak. Fig. 4.3(f) shows that the PF has also extracted the second peak amplitudes with statistically smaller error values than the KF (p < 0.01).

Fig. 4.4 shows the results of the latency estimation for the positive and negative peaks. The PF reveals the latencies more accurately for both peaks except for the positive peaks in the last few trials. Both algorithms, however, give reasonable and

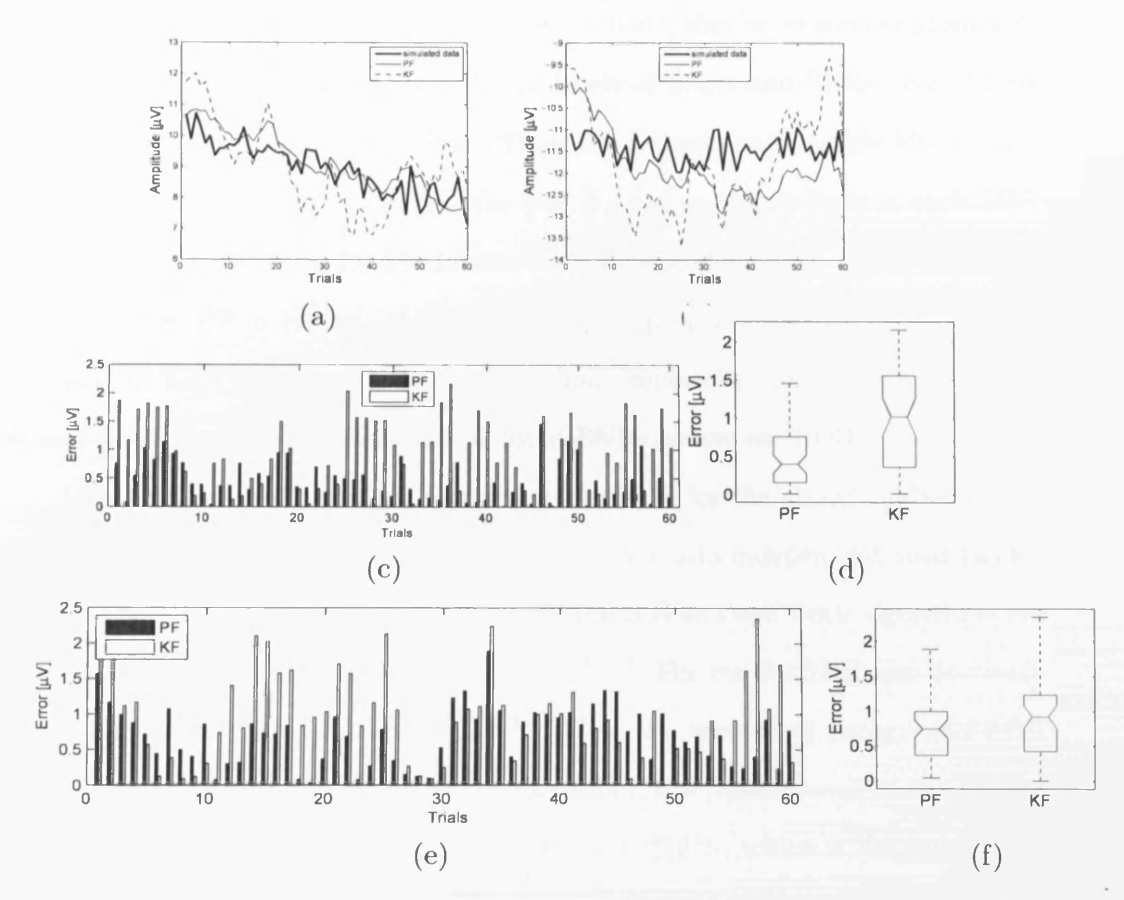


Figure 4.3: Amplitudes of the first and second peaks from trial to trial and their estimations SNR = -5dB and SBR = -10dB; (a) simulated (thick line), estimated using PF (solid line) and estimated amplitudes using KF (dashed line) for the positive peak, (b) estimated values for the negative peak, (c) the error between the simulated and estimated amplitudes for PF (black bar) and KF methods (white bar) for the first peak, (d) mean and standard deviation of errors for each method (e) the error between simulated and estimated amplitudes for PF (black bar) and KF methods (white bar) for the second peak, and (f) mean and standard deviation of errors for each method.

indeed similar estimates and there is no significant difference between their performances.

To further quantify the performance of the methods, they were compared numerically by root mean square error for different levels of SNRs and SBRs. Fig. 4.5(a) shows the output SNR vs. input SNR in dB for the Kalman and particle filters. The output SNRs were obtained by finding the best σ_w and q_w parameters in each SNR and executing the algorithms for 100 Monte Carlo independent runs. Using the DWT jointly with either PF or KF as a two-stage denoising process results in an acceptable performance in high input SNR. Both algorithms, especially the PF, are robust to GWN and their results are consistent for input SNRs as low as -10dB.

Fig. 4.5(b) shows the output SBR versus input SBR for the above methods. The output SBRs were obtained by executing 100 Monte Carlo independent runs (as for the SNR). The PF outperforms the KF for all input SBRs and both algorithms are more sensitive to background EEG noise than GWN. The output SBR also decreases rapidly in comparison with the output SNR. When the amount of background EEG increases and the noise becomes more non-Gaussian, the performance of the PF improves accordingly. Indeed, if the added noise is not GWN, which is the case in real EEG data, the PF is more robust than the KF to this violation. It is also noteworthy that, in the PF, any kind of noise with known distribution can be handled. This contrasts with the KF, where the noise should be GWN with a known covariance matrix.

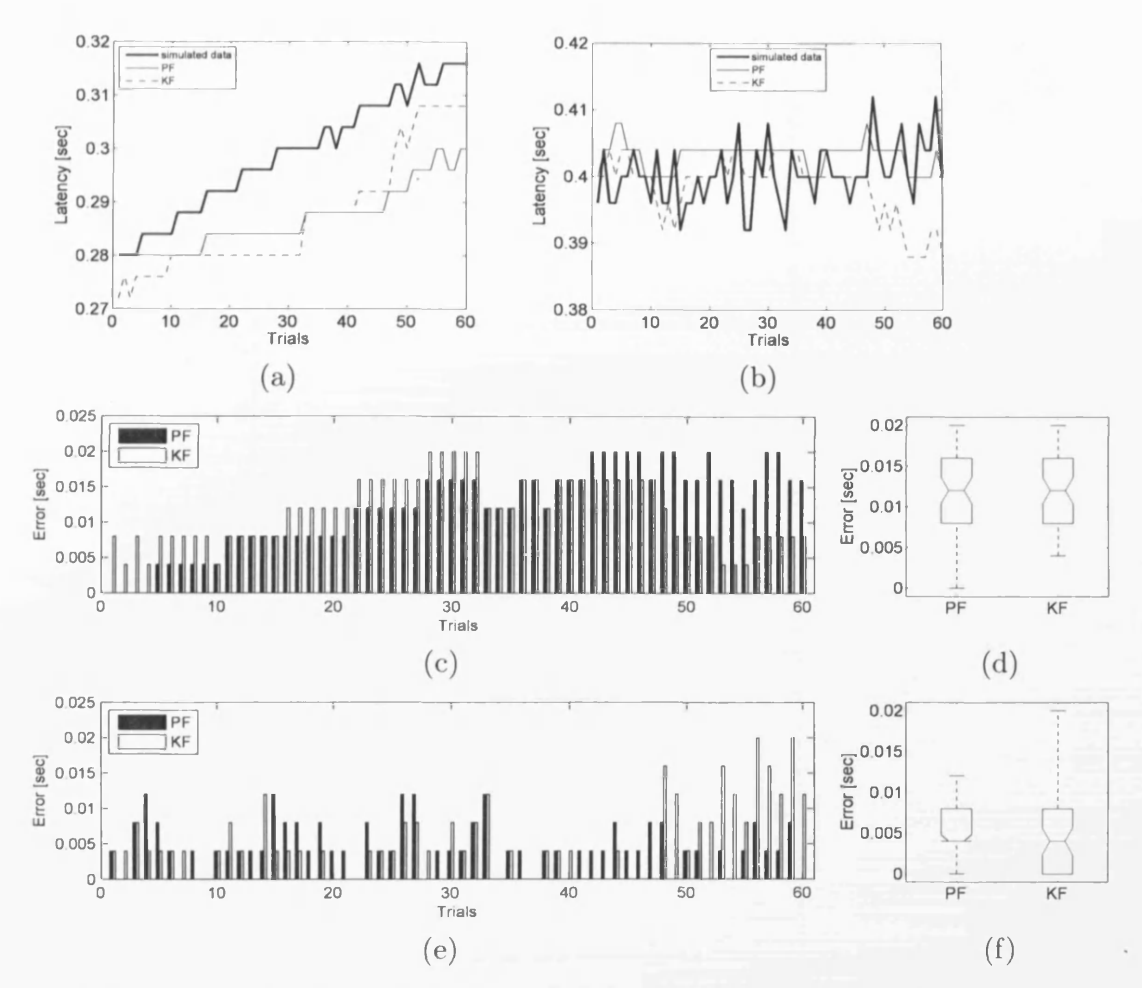


Figure 4.4: Latencies of the first and second peaks from trial to trial and their estimations for SNR = -5dB and SBR = -10dB; (a) simulated (thick line), estimated using PF (solid line), and estimated latencies using KF (dashed line) for the positive peak, (b) simulated (thick line), estimated using PF (solid line) and estimated latencies using KF (dashed line) results for the negative peak, (c) the error between simulated and estimated latencies for PF (black bar) and KF methods (white bar) for the first peak, (d) the error between simulated and estimated latencies for PF (black bar) and KF methods (white bar) for the second peak, (e) the error between simulated and estimated latencies for PF (black bar) and KF methods (white bar) for the second peak, and (f) mean and standard deviation of errors for each method.

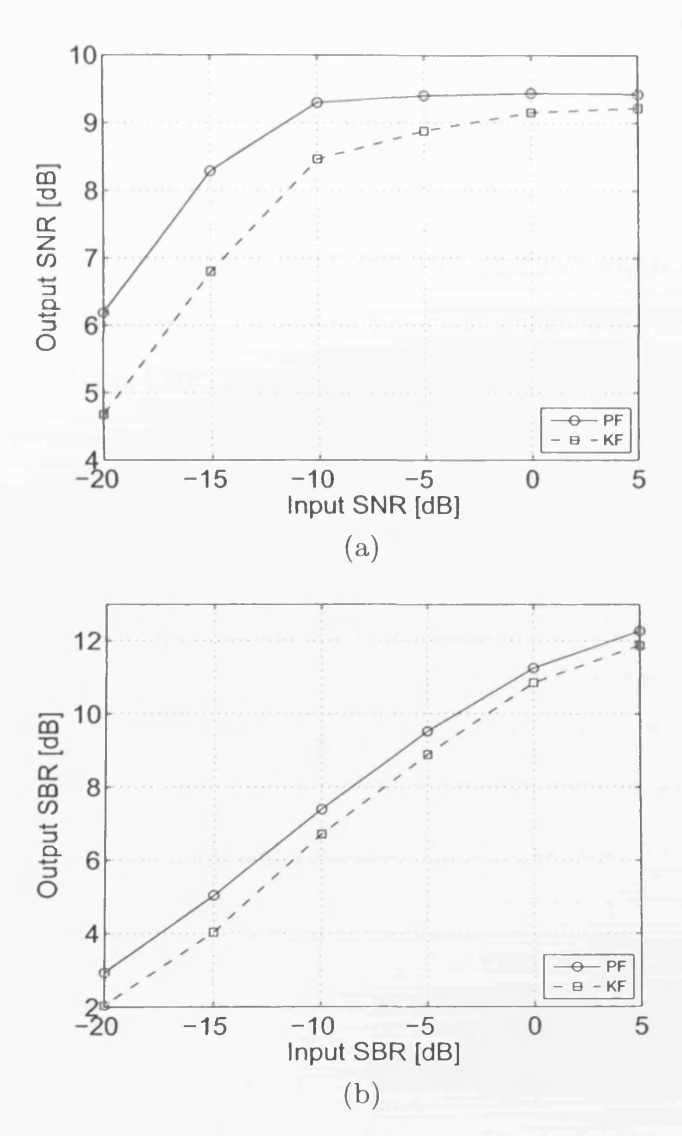


Figure 4.5: Performance of KF and PF methods as indexed by mean square error for 100 Monte Carlo trials (a) input SNR versus output SNR. Both methods, especially PF, are robust to high input SNR, and (b) input SBR versus output SBR. This decreases rapidly in comparison with SNR.

4.3.2 Real Data Results

Real data was obtained in an *oddball* paradigm. Four right-handed healthy individuals participated in the experiment. The experiment was run in a quiet, normally illuminated room. The participants were seated comfortably in an armchair. All gave informed consent.

Each participant heard in total 300 tones, 240 (80%) of which were at one pitch (the frequent tones) and 60 (20%) of which were at a different pitch (the infrequent tones). In this paradigm, ERPs elicited by infrequent tones are associated with a large positive-going wave - the P300 - which peaks approximately 0.3sec post-stimulus. Accordingly, epochs from 0.2sec to 0.5sec time-locked to stimulus onset for infrequent trials were extracted for analysis.

By dividing the power of the averaged signal to the mean of power of all trials, an input SBR of approximately -10dB was obtained. By using this SBR and the results obtained from the simulations, the values around $q_w = 5$ and $q_v = 40$ were deemed appropriate. The initial state of the filter was set to zero and, in order to accommodate the convergence of the filter, the first ten trials were excluded. The information contents of those ten first trials can be extracted by running the PF in the reversed trial order. Particle smoothers may also be used as an alternative [56].

Fig. 4.6 provides the results of the proposed algorithms for real data. The Cz site, at which the P300 component amplitude in the oddball paradigm is prominent, was chosen for analysis. Fig. 4.6(a) shows a superposition of all original trials and their average signal (solid line). Original trials are also presented in Fig. 4.6(b) in the form of ERP images, in which the ERPs are plotted vertically with time on the horizontal axis. Color represents the amplitudes of the trials, from blue to red corresponding to

transition from maximum negative to maximum positive. The second row of Fig. 4.6 shows the results of the PF approach for all of the trials (c), the ERP image (d), and the estimated amplitudes from trial to trial (e). Both the signal and the ERP images show that the P300 has been extracted from noisy ERP data. An increase in the latency and decrease in the amplitude of the P300 over successive trials is evident in Fig. 4.6(d) and Fig. 4.6(e), respectively. The results of the KF method are shown in Fig. 4.6(f), (g) and (h). The KF method does not show structural variation of the amplitude and latency across trials that was identified by the PF.

A primary application of such a single-trial ERP extraction approach can be an investigation of the likely induced correlates of the amplitude and latency of ERP components. Fig. 4.7 shows the estimated correlation between ERP amplitudes and latencies using PF (black dots) and KF (red dots) methods for the four subjects. The linear regression has been shown in all figures using black (for the PF) and red (for the KF) lines. There is a significant negative correlation between latency and amplitude of each of the four subjects obtained by the PF (r = -0.357 and p < 0.01, two tailed) but not by the KF (r = -0.0986, not significant (n.s.)).

These observations demonstrate the accuracy of the approach and its potential use in ST-ERP analysis, especially when trial to trial variation in ERPs is of major interest. Recently, such ERP estimation has also been proved to be very useful in single-trial correlation analysis between EEGs and functional magnetic resonance imaging signals [5].

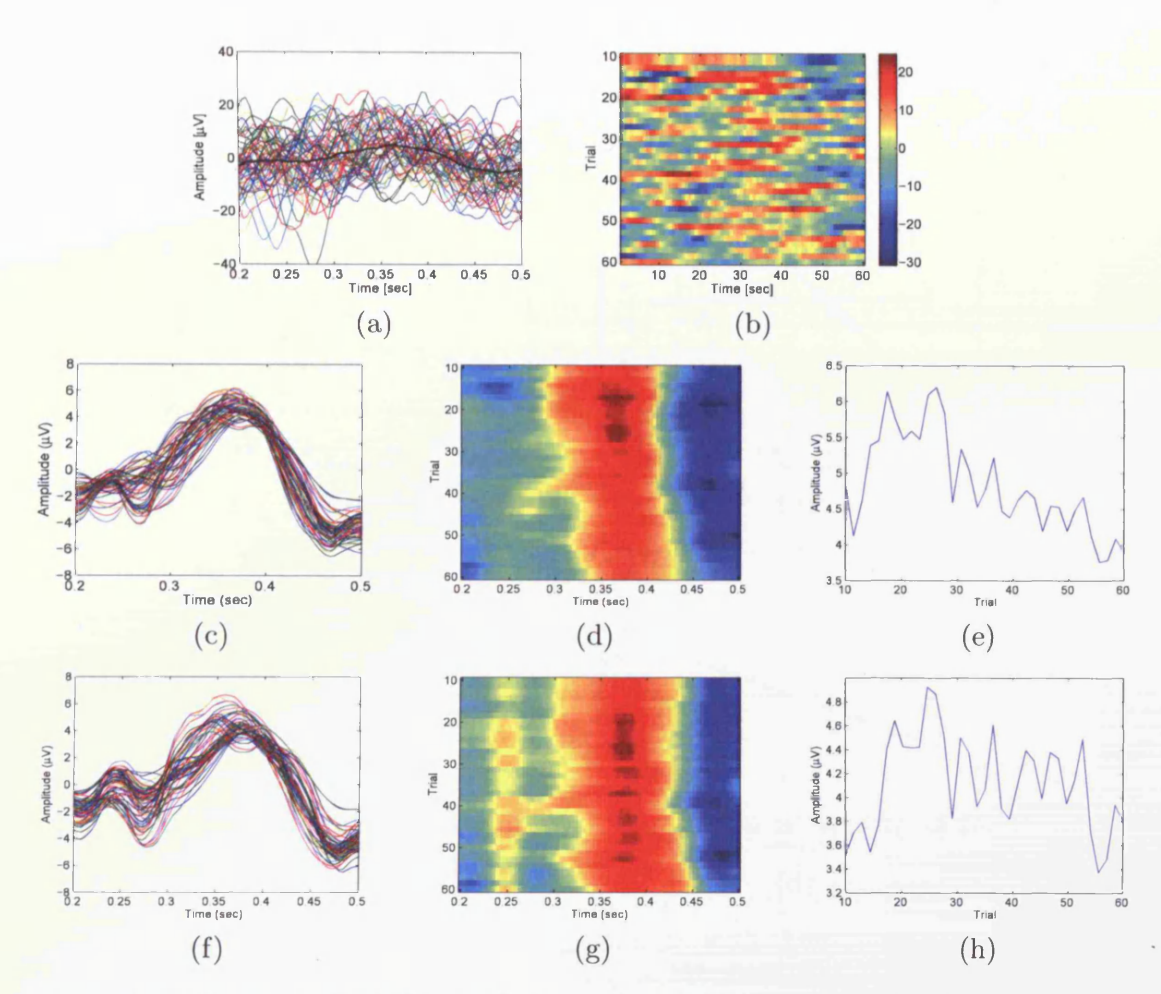


Figure 4.6: Estimation of P300 in real data using the proposed method (a) superposition of original trials with their average, (b) ERP image of original signals - there is no evident ERP signature in this image, (c) superposition of estimated ERPs using the PF method, (d) ERP image of estimated ERPs (P300 in red color) using the PF method, (e) estimated P300 filtered peak amplitude versus trials using PF. There is a decreasing trend across trials, (f) superposition of estimated ERPs using the KF method, (g) ERP image of estimated ERPs with (P300 in red) using the KF method, and (h) estimated P300 filtered peak amplitude versus trials using KF. Unlike PF (see (e) above) there is no directional trend across trials.

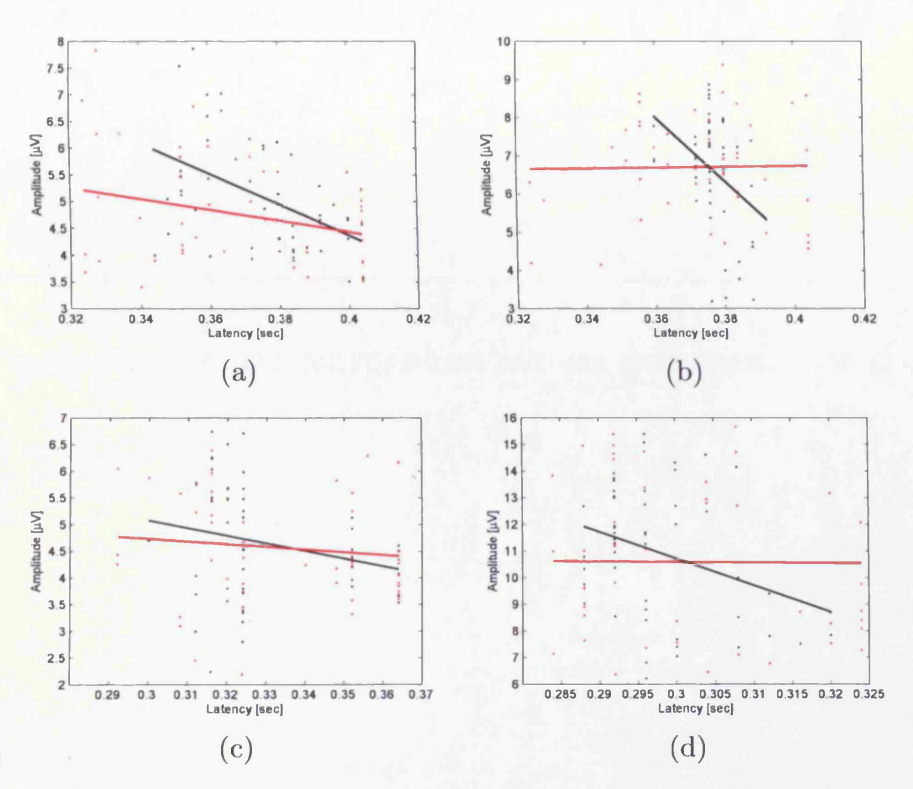


Figure 4.7: Latency vs. amplitude in four subjects with their linear regression obtained by PF shown by black and KF shown by red. A significant negative correlation between amplitude and latency with average r=-0.357~(p<0.01, two tailed) for four subjects can be seen only for the PF method (r=-0.0986, n.s.), (a) subject number one (PF: r=-0.472, p<0.001) (KF: r=-0.2864, p<0.05), (b) subject number two (PF: r=-0.400, p<0.005) (KF: r=0.0185, n.s.), (c) subject number three (PF: r=-0.227, p<0.05) (KF: r=-0.1182, n.s.), and (d) subject number four (PF: r=-0.327, p<0.05) (KF: r=-0.0102, n.s.).

4.4 Conclusions

A new approach for ST-ERP estimation based on particle filtering of discrete wavelet transformed ERPs is proposed. The main merits of the proposed method are in exploitation of the sequential importance sampling as well as the use of Bayesian theory, which promises high performance for non-Gaussian and non-stationary data like ERPs. This method uses only one EEG channel for ST-ERP extraction and, therefore, ignores spatial information contained in the EEG data. In addition, as no prior knowledge about the measurement has been considered, it may be more sensitive to the outliers than other methods such as MAP estimator.

The method was tested for simulated and real data. The simulation results demonstrate the improved accuracy of estimations by PF in comparison with KF, especially when the assumption about GWN is violated (background EEG is considered as noise). Application of the method to real data recorded in an oddball paradigm shows that the amplitude of the P300 decreases and its latency increases over trials during the task. These demonstrations emphasis the potential for this approach in ST analysis of ERP data.

The ability to extract reliably single trial ERP data would be of great benefit in several contexts. For example, for ERP researchers interested in using ERPs to isolate cognitive processes, the reliance on averaging introduces an inevitable degree of caution when making inferences about the onset times of processes. Caution is also necessary when inferring whether peak amplitude differences between averaged ERPs for different conditions do in fact reflect consistent peak amplitude differences at the level of individual trials. The alternative is that the amplitude differences emerge because of greater inter-trial variability in peak latencies for one condition in

comparison to the other.

Finally, in the next two chapters, we move from single trial estimation to dipole source localization and in Chapter 7 a robust framework is developed for single-trial dipole source localization based on PF. Preliminary results are reported in [75, 74] whereby considering the dipole locations as having a nonlinear relation with the measurements, the variational Bayes and maximum likelihood based methods estimate the amplitude, latency, and width of the ERPs after they have been localized.

Chapter 5

Deflation Beamforming for E/MEG Dipole Source Localization

5.1 Introduction

As it was mentioned in Chapter 2, scalp-recorded E/MEG with excellent temporal resolution suffers from relatively poor spatial resolution. The poor spatial resolution motivates research into methods that can accurately localize E/MEG sources.

In this study, the BF approach is generalized by adding two more terms to its formulation. The first term additionally reduces the noise power at the output of the BF. This method assumes the covariance matrix of the noise is known a priori. The second term places nulls at known locations to improve the detection of the unidentified dipoles. In this approach, a dipole is located by finding the grid cell which has the maximum power, while deflating the power of any dipoles that have already been identified. Using Lagrange multiplier method, the multiple constraint problem is converted to an unconstrained problem and solved via an optimization

process. At the same time the power of each location is estimated and normalized with respect to the power in the presence of noise only. The deflation BF method helps to overcome two main problems of multiple dipole source localization using the BF: restriction of dipole localization to the dominant sources, and inaccurate performance in the presence of highly correlated sources. In addition, to improve the performance of the method further, an iterative approach for deflation and localization of dipoles is proposed.

This chapter is organized as follows. The dipole source localization framework is given in the following section, and then the BF approach for dipole source localization is reviewed. The new method is presented in Section 5.2.3. Performance analysis of the method is presented in Section 5.2.4. Simulated results for two dipoles with Gaussian sequences are presented in 5.3.1, and then the results for the simulated MEG are presented. Section 5.4 is devoted to the assessment of the method in a real auditory ERF experiment.

5.2 Methods

5.2.1 Problem Formulation

Let y be a vector composed of the potentials measured from L electrodes. Each dipole is specified by its three dimensional location ρ and its three dimensional moment m. The medium between the sources and the electrodes is assumed to be homogeneous, and the potential at the scalp y to be a superposition of the potentials from q dipoles.

These assumptions result in

$$\mathbf{y} = \sum_{i=1}^{q} \mathbf{H}(\boldsymbol{\rho}_i) \mathbf{m}(\boldsymbol{\rho}_i) + \mathbf{v}$$
 (5.1)

Here, \mathbf{v} represents the noise which is uncorrelated with the source activities. \mathbf{H} is the gain or lead field matrix, which is a nonlinear function of the dipole's location, and can be calculated in a spherical head model or can be obtained using a realistic head model. In the latter case, the head is divided into a number of grid cells and for each grid cell the gain or lead field matrix \mathbf{H} is obtained according to the geometry of the head using imaging systems such as MRI. The aim is to estimate the dipole locations and moments based on the measurements and the prior knowledge about the number of dipoles. The source moments are assumed to vary but the locations are assumed to remain the same during the measurements. In addition, the *i*th dipole moment is assumed to be a random quantity and its behavior is described in terms of mean $\overline{\mathbf{m}}_i$ and covariance matrix \mathbf{C}_i .

Equation (5.1) can be written in a matrix form as $\mathbf{y} = \tilde{\mathbf{H}}\tilde{\mathbf{M}}$, where $\tilde{\mathbf{H}} = [\mathbf{H}(\rho_1) \dots \mathbf{H}(\rho_q)]$ is the matrix of all lead field matrices and $\tilde{\mathbf{M}} = [\mathbf{m}(\rho_1) \dots \mathbf{m}(\rho_q)]^T$ is the matrix of all moments. If the dipole locations are known, then the moments are obtained accordingly in an optimum way as $\tilde{\mathbf{M}} = \tilde{\mathbf{H}}^{\dagger}\mathbf{y}$, where $\tilde{\mathbf{H}}^{\dagger}$ is the pseudoinverse of $\tilde{\mathbf{H}}$. In the following, therefore, only estimation of the dipole locations is desired.

5.2.2 Beamforming

BF is a spatial filter which minimizes the output power of the filter while passing activity from a location of interest. Assuming each grid cell as a potential source of

interest, such a spatial filtering scheme provides a metric of source activity. Let \mathbf{W}^T denote the beamspace spatial linear filter weights for location ρ . The spatial filter is obtained by solving [111]:

$$\min_{\mathbf{W}^T} E\{|\mathbf{W}^T \mathbf{y}|^2\} \quad s.t. \ \mathbf{W}^T \mathbf{H}(\boldsymbol{\rho}) = \mathbf{I}$$
 (5.2)

where $\mathbf{I} \in \mathbb{R}^{3\times3}$ is the identity matrix and $|.|^2$ denotes Frobenius norm. Using the Lagrange multipliers method, the above constrained problem is converted to an unconstrained problem. By solving this problem, the variance or power at the beamspace spatial filter output at location $\boldsymbol{\rho}$ is expressed as [111]:

$$P(\boldsymbol{\rho}) = tr\{\left(\mathbf{H}^{T}(\boldsymbol{\rho})\mathbf{C}_{\mathbf{y}}^{-1}\mathbf{H}(\boldsymbol{\rho})\right)^{-1}\}\tag{5.3}$$

Here C_y is the covariance matrix of y and $tr\{.\}$ and $(.)^{-1}$ are trace and inverse operators, respectively.

The MEG lead field matrix varies as a function of location and has variable sensitivity to the noise gain of the filter. In order to overcome this problem, equation (5.3) is normalized and divided by the power of the corresponding noise spatial spectrum in the absence of the signal [92]:

$$P_n(\boldsymbol{\rho}) = \frac{tr\{\left(\mathbf{H}^T(\boldsymbol{\rho})\mathbf{C}_y^{-1}\mathbf{H}(\boldsymbol{\rho})\right)^{-1}\}}{tr\{\left(\mathbf{H}^T(\boldsymbol{\rho})\mathbf{C}_y^{-1}\mathbf{H}(\boldsymbol{\rho})\right)^{-1}\}}$$
(5.4)

where C_y is an estimate of the signal covariance and C_v is an estimate of the noise-only covariance. The localization of sources is performed by finding ρ that maximizes (5.4).

For the case of unknown C_y , a consistent estimate of this covariance matrix can be obtained as

$$\mathbf{C}_{y} = \frac{1}{M-1} \sum_{t=1}^{M} (\mathbf{y}_{t} - \overline{\mathbf{y}})(\mathbf{y}_{t} - \overline{\mathbf{y}})^{T}$$
(5.5)

where $\overline{\mathbf{y}} = \frac{1}{M} \sum_{t=1}^{M} \mathbf{y}_{t}$ is the sample mean and \mathbf{y}_{t} , t = 1, ..., M are observations of the phenomena to be localized. Note that these observations must all correspond to the same underlying spatial spectrum. That is, the data needs to be wide sense stationary.

5.2.3 Deflation Beamforming

In the absence of noise, the source powers are estimated perfectly and then the source locations are simply found as the global maximizers of (5.4). However, in a noisy environment, nonlinear search techniques may miss shallow or adjacent peaks and return to peaks with larger power. The best peaks also should be located rather than any local maxima. One technique to overcome this problem is to deflate the identified dipoles and perform another search to find the next dipole. This problem is formulated by adding another constraint to equation (5.2) to stop the activity from the known locations. Furthermore, the power of the noise at the output of the BF is minimized to improve the estimation. First, the number of dipoles is assumed to be two and then the solution for q dipoles is generalized. Based on the above assumptions, the following optimization problem is resulted:

$$\min_{\mathbf{W}^T} E\{|\mathbf{W}^T \mathbf{y}|^2\} + \lambda E\{|\mathbf{W}^T \mathbf{v}|^2\}$$
s.t. $\mathbf{W}^T \mathbf{H}(\boldsymbol{\rho}_1) = \mathbf{0}$, and $\mathbf{W}^T \mathbf{H}(\boldsymbol{\rho}_2) = \mathbf{I}$ (5.6)

where λ is a penalty factor, ρ_1 is the location of the first estimated dipole and ρ_2 is the location of the second dipole. The extra term $\lambda E\{|\mathbf{W}^T\mathbf{v}|^2\}$ minimizes the power of the noise at the output of the BF and the extra term $\mathbf{W}^T\mathbf{H}(\rho_1) = \mathbf{0}$ deflates the first source. In the following, to simplify the notation, \mathbf{H}_i is used instead of $\mathbf{H}(\rho_i)$.

The solution to (5.6) can be given as follow. By defining $\tilde{\mathbf{I}}_d^T = [\ \mathbf{0}\ \mathbf{I}\]$ and $\tilde{\mathbf{H}} = [\ \mathbf{H}_1\ \mathbf{H}_2\]$, the constraints in the second line of equation (5.6) can be written in matrix form as $\mathbf{W}^T \tilde{\mathbf{H}}^T = \tilde{\mathbf{I}}_d^T$. Using the method of Lagrange multipliers the closed-form solution for \mathbf{W}^T is:

$$\mathbf{W}^{T} = \tilde{\mathbf{I}}_{d}^{T} \left(\tilde{\mathbf{H}}^{T} (\mathbf{C}_{y} + \lambda \mathbf{C}_{v})^{-1} \tilde{\mathbf{H}} \right)^{-1} \tilde{\mathbf{H}}^{T} (\mathbf{C}_{y} + \lambda \mathbf{C}_{v})^{-1}.$$
 (5.7)

If the deflation term of equation (5.7) is ignored (dropping $\tilde{\mathbf{I}}_d^T$ and matrix tilde) and \mathbf{C}_v and \mathbf{C}_v are assumed to be unknown, the optimal solution will be $(\mathbf{H}^T\mathbf{H})^{-1}\mathbf{H}^T$, which is the pseudoinverse of matrix \mathbf{H} and has been effectively applied to \mathbf{E}/MEG dipole source localization [54, 41]. Moreover, if there is no knowledge about \mathbf{C}_v , and \mathbf{C}_v is known a priori, the optimal solution is $(\mathbf{H}^T\mathbf{C}_v^{-1}\mathbf{H})^{-1}\mathbf{H}^T\mathbf{C}_v^{-1}$. This is the maximum likelihood estimation and has also been employed in \mathbf{E}/MEG source localization (see [66, 27]). If there is no knowledge about \mathbf{C}_v , and \mathbf{C}_v is a priori known, the optimal solution is $(\mathbf{H}^T\mathbf{C}_v^{-1}\mathbf{H})^{-1}\mathbf{H}^T\mathbf{C}_v^{-1}$ which is the BF, and as mentioned before, it has been used for \mathbf{E}/MEG source localization in [111]. In addition, if the noise covariance matrix is assumed to be Gaussian white noise (GWN) (i.e. $\mathbf{C}_v = \lambda \mathbf{I}$), the result is the BF with loading factor $(\mathbf{H}^T(\mathbf{C}_v + \lambda \mathbf{I})^{-1}\mathbf{H})^{-1}\mathbf{H}^T(\mathbf{C}_v + \lambda \mathbf{I})^{-1}$. This is also a well-established method for \mathbf{E}/MEG source localization [92].

Considering the deflation terms of equation (5.7) and ignoring C_v , similar formulation in the eigenspace has been given in [20] for MEG source localization. In

summary, equation (5.7) is a generalized solution to the BF when the location and covariance matrix of the noise is known a priori.

We continue by expressing the output power of the deflation BF at location ρ_2 as:

$$P(\rho_2) = E\{|\mathbf{W}^T\mathbf{y}|^2\} + \lambda E\{|\mathbf{W}^T\mathbf{v}|^2\} = tr\{\mathbf{W}^T(\mathbf{C}_u + \lambda \mathbf{C}_v)\mathbf{W}\}$$
(5.8)

substituting \mathbf{W}^T from equation (5.7) into equation (5.8) and after some algebra, the following equation is obtained:

$$P(\boldsymbol{\rho}_2) = tr\{\tilde{\mathbf{I}}_d \left(\tilde{\mathbf{H}}^T (\mathbf{C}_y + \lambda \mathbf{C}_v)^{-1} \tilde{\mathbf{H}}\right)^{-1} \tilde{\mathbf{I}}_d^T\}$$
 (5.9)

The location of the second dipole is found by searching all grid cells which maximizes (5.9).

In practice the measurement \mathbf{y} is signal plus noise and minimizing $E\{|\mathbf{W}^T\mathbf{y}|^2\}$ also minimizes the extra term $E\{|\mathbf{W}^T\mathbf{v}|^2\}$. It may therefore seems that this term in equation 5.6 is unnecessarily. However, since the solution classical BF is not perfect, by choosing a proper value for λ in the noise power is more minimized and the result will be improved. As another clarification consider a special case when the noise is Gaussian white whereas the solution of the above problem is converted to the beamforming with diagonal loading (as described above). This beamformer improved the results and has been widely employed for E/MEG source localization.

Generalizing the above solution for q poles is straightforward. Assume the q-1 dipole locations have been found and the location of the qth dipole should be estimated. The location of the qth dipole is estimated as the location which maximizes

(5.9) using the following new definitions

$$\tilde{\mathbf{H}}^T = \begin{bmatrix} \mathbf{H}_1 & \dots & \mathbf{H}_q \end{bmatrix}^T, \quad \tilde{\mathbf{I}}_d^T = \begin{bmatrix} \mathbf{0} & \dots & \mathbf{0} & \mathbf{I} \\ \mathbf{0} & \dots & \mathbf{0} & \mathbf{I} \end{bmatrix}$$
 (5.10)

Similar to Section 5.2.2, equation (5.9) is normalized and divided by the power of the corresponding noise spatial spectrum in the absence of the signal as

$$P_n(\boldsymbol{\rho}_q) = \frac{tr\{\tilde{\mathbf{I}}_d^T \left(\tilde{\mathbf{H}}^T (\mathbf{C}_y + \lambda \mathbf{C}_v)^{-1} \tilde{\mathbf{H}}\right)^{-1} \tilde{\mathbf{I}}_d\}}{tr\{\tilde{\mathbf{I}}_d^T \left(\tilde{\mathbf{H}}^T (\lambda \mathbf{C}_v)^{-1} \tilde{\mathbf{H}}\right)^{-1} \tilde{\mathbf{I}}_d\}}$$
(5.11)

Therefore, the location of the qth dipole is obtained as ρ_q which maximizes (5.11). The neural activity index in (5.11) requires knowledge about the noise covariance matrix. \mathbf{C}_v can be estimated from the data that is known to be source free, such as pre-stimulus data in an event-related field (ERF) experiment. The noise of the channels is also can be assumed to be GWN (i.e. $\mathbf{C}_v = \lambda \mathbf{I}$), where the noise power λ can be chosen empirically and according to the available data set.

Equation (5.11) also needs a true estimation of q-1 first source locations. In the general case, the q-1 first source locations may not be known or correctly estimated, which negatively influence the performance of deflation BF. In Section 5.2.5, an iterative localization and deflation approach to cope with this problem is proposed.

5.2.4 Performance Analysis

In this section, the performances of BF and deflation BF are analytically evaluated. Performance of the methods for uncorrelated sources is discussed first, followed by discussion about the correlated sources.

For investigation of deflation BF, by ignoring the covariance matrix of the noise C_v , equation (5.9) is expanded for two sources as

$$P(\rho_{2}) = tr\left\{ \begin{bmatrix} 0 & \mathbf{I} \end{bmatrix} \begin{pmatrix} \mathbf{H}_{1}^{T} \\ \mathbf{H}_{2}^{T} \end{bmatrix} \mathbf{C}_{y}^{-1} \begin{bmatrix} \mathbf{H}_{1} & \mathbf{H}_{2} \end{bmatrix} \right\}^{-1} \begin{bmatrix} 0 \\ \mathbf{I} \end{bmatrix} \right\}$$

$$= tr\left\{ \begin{bmatrix} 0 & \mathbf{I} \end{bmatrix} \begin{bmatrix} \mathbf{H}_{1}^{T} \mathbf{C}_{y}^{-1} \mathbf{H}_{1} & \mathbf{H}_{1}^{T} \mathbf{C}_{y}^{-1} \mathbf{H}_{2} \\ \mathbf{H}_{2}^{T} \mathbf{C}_{y}^{-1} \mathbf{H}_{1} & \mathbf{H}_{2}^{T} \mathbf{C}_{y}^{-1} \mathbf{H}_{2} \end{bmatrix}^{-1} \begin{bmatrix} 0 \\ \mathbf{I} \end{bmatrix} \right\}$$

$$(5.12)$$

Using block matrix inversion the above expression is simplified to

$$P(\rho_2) = tr\{ (\mathbf{H}_2^T \mathbf{C}_v^{-1} \mathbf{H}_2 - (\mathbf{H}_2^T \mathbf{C}_v^{-1} \mathbf{H}_1) (\mathbf{H}_1^T \mathbf{C}_v^{-1} \mathbf{H}_1)^{-1} (\mathbf{H}_1^T \mathbf{C}_v^{-1} \mathbf{H}_2) \}^{-1} \}$$
 (5.13)

The first term in the right hand side of above equation is the output power of BF at location ρ_2 (see equation (5.3)). It is well known that BF is ideal if the noise power tends to zero (e.g. [45])¹. This means that as the noise power tends to zero, if the BF points to the source location, $(\mathbf{H}_2^T \mathbf{C}_y^{-1} \mathbf{H}_2)^{-1}$ tends to the identity matrix and otherwise tends to a matrix of zeros.

Following a similar method, in the presence of small added noise, if the column vectors of \mathbf{H}_1 are linearly independent from the column vectors of \mathbf{H}_2 , both $\mathbf{H}_2^T \mathbf{C}_y^{-1} \mathbf{H}_1$ and $\mathbf{H}_1^T \mathbf{C}_y^{-1} \mathbf{H}_2$ are matrices of zeros. Thus, the second expression in the right hand

Here the covariance matrix has been expanded as $C_y = \sigma \mathbf{I} + \sum_{i=1}^q \alpha_i \mathbf{H}_i \mathbf{H}_i^T$, where α_i are scalars representing power of the *i*th source and σ is the noise power.

side of the above equation will be zero. Moreover, if $\mathbf{H}_1^T \mathbf{H}_2 = 0$ (i.e. the column vectors of \mathbf{H}_1 are perpendicular to column vectors of \mathbf{H}_2) and noise and sources are spatially uncorrelated and identically distributed, the second expression on the right hand side of equation (5.13) is zero again (regardless of the noise power). Under these assumptions, therefore, the deflation BF is also ideal and exactly behaves like BF.

In most cases, however, the above strong assumptions do not hold and deflating any location will reduce the output power of deflation BF according to the available noise power. Therefore, the number of deflated sources should be kept as small as possible.

In general, the BF has moderate sensitivity to correlated sources [6]. However, if a correct estimation of the previous q-1 source locations be known, the correlation between the dipoles has no impact on the output power of the deflation BF for the qth dipole. Letting $C_{i,j} = E\{[\mathbf{m}(\rho_i) - \overline{\mathbf{m}}(\rho_i)][\mathbf{m}(\rho_j) - \overline{\mathbf{m}}(\rho_j)]^T\}$ be the cross covariance between the sources at locations ρ_i and ρ_j , the output power at location ρ_q is given by

$$tr\left\{\mathbf{W}^{T}\mathbf{C}_{y}\mathbf{W}\right\} =$$

$$tr\left\{\sum_{i=1}^{q}\mathbf{W}^{T}\mathbf{H}_{i}\mathbf{C}_{i,i}\mathbf{H}_{i}^{T}\mathbf{W} + \sum_{\substack{i,j=1\\i\neq j}}^{q}\left(\mathbf{W}^{T}\mathbf{H}_{i}\mathbf{C}_{i,j}\mathbf{H}_{j}^{T}\mathbf{W} + \mathbf{W}^{T}\mathbf{H}_{j}\mathbf{C}_{j,i}\mathbf{H}_{i}^{T}\mathbf{W}\right) + \mathbf{W}^{T}\mathbf{C}_{v}\mathbf{W}\right\}$$

$$= tr\left\{\mathbf{C}_{q,q} + \mathbf{W}^{T}\mathbf{C}_{v}\mathbf{W}\right\}$$
(5.14)

Note that $\mathbf{W}^T\mathbf{H}_i = \mathbf{0}$ for $i \neq q$ and $\mathbf{W}^T\mathbf{H}_i = \mathbf{I}$ for i = q are used to simplify (5.14), which can be justified by multiplying equation (5.7) by $\tilde{\mathbf{H}}$. Note that in BF without deflation, the other terms in equation (5.14) are not necessarily zero since

 $\mathbf{W}^T\mathbf{H}_i \neq \mathbf{0}$ for $i \neq q$. When this is the case, the estimated power of the source at location ρ_q can be less than its true value. Therefore, the output power of the deflation BF unlike the BF depends only on the power of the desired source and power of the noise. In practice, however, due to existence of the uncorrelated noise, as well as inaccurate estimation of the data covariance matrix and dependent lead field matrices, the output power of deflation BF may depend to some degree on the correlation between sources. The performance of the deflation BF method in the presence of correlated source activities is explored further in Section 5.3.1.

5.2.5 Iterative Localization and Deflation

In many practical cases, no prior knowledge about the true source locations is known. Under these circumstances, if the first source is incorrectly located, localization of other sources may also fail. To circumvent this problem, the sources are found via a number of iterations such that in each iteration the other sources are deflated while searching for the current source location. For example, suppose the number of dipoles is two. In the first iteration, the location of the first dipole is found and then whilst deflating the first dipole the location of the second dipole is found. In the next iteration, the first dipole is localized while deflating the second dipole. These iterations are performed until the dipole locations remain the same in each iteration. This algorithm can be generalized similarly for q dipoles. The pseudocode of the method for q dipoles is presented in Algorithm 2. In this pseudocode, ρ_i^j is the location of the ith source in the jth iteration and K represents the number of iterations. Based on our experience, in most cases the algorithm converges in less than 5 iterations, and K was set to 5. As it will be discussed in the numerical

results section, in the presence of moderate noise power this technique helps to find accurately the locations of all sources, even when the sources are highly correlated.

```
Algorithm 2 Pseudocode for the proposed deflation and localization method find \rho_1^1 using equation (5.4)

deflate \rho_1^1 and find \rho_2^1 using equation (5.11)

:

deflate \rho_1^1, \ldots, \rho_{q-1}^1 and find \rho_q^1 using equation (5.11)

for j=2 to K do

deflate \rho_2^{j-1}, \ldots, \rho_q^{j-1} and find \rho_1^j using equation (5.11)

deflate \rho_1^{j-1}, \rho_3^{j-1}, \ldots, \rho_q^{j-1} and find \rho_2^j using equation (5.11)

:

deflate \rho_1^{j-1}, \rho_3^{j-1}, \ldots, \rho_q^{j-1} and find \rho_q^j using equation (5.11)

end for
```

5.3 Numerical Results

Two different simulations are presented in order to show both the performance and the utility of the proposed deflation BF. In the first simulation, different effects of simulation on the performance of the methods are considered for the two dipoles whose moments are zero-mean Gaussian sequences. The second simulation is a MEG example, localizing three dipoles in a three-dimensional space.

A spherical head model was used to compute the forward model. The values of estimators were scanned within a discrete cubic grid with more than 6510 grid points and an inter-grid distance of 0.5cm. A sensor alignment of the 275-sensor array from

the Omega (VSM MedTech, Canada) neuromagnetometer was used. The data was sampled at the rate of 1000hz. The covariance matrix C_y was estimated from 500 data samples (0.5sec), and the covariance matrix of noise C_v was estimated from 200 samples of data free segments. The locations of the simulated sources are shown in Fig. 5.1 in axial and coronal views.

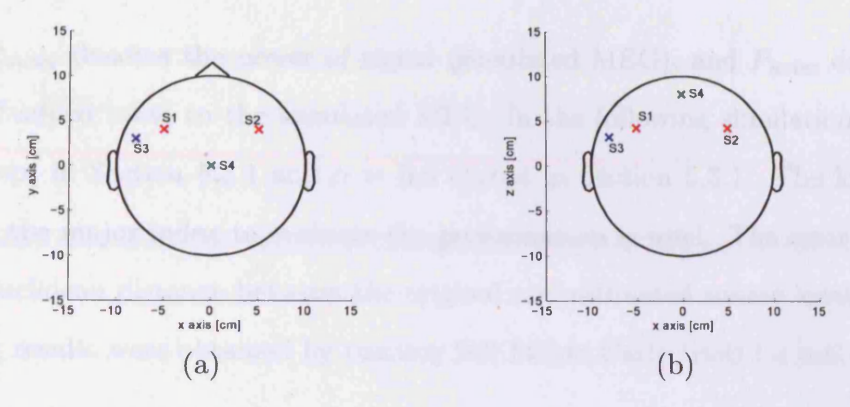


Figure 5.1: Location of sources used for different simulations; (a) axial view and (b) coronal view.

5.3.1 Two Dipoles Example

In this simulation, two sources were used to numerically evaluate the methods. Their moments were Gaussian sequences as follows

$$\mathbf{m}(\boldsymbol{\rho_1}) = \mathcal{N}(\mathbf{0}, \mathbf{I})$$

$$\mathbf{m}(\boldsymbol{\rho_2}) = \alpha \mathbf{m}(\boldsymbol{\rho_1}) + (1 - \alpha)\mathcal{N}(\mathbf{0}, \mathbf{I})$$
(5.15)

where $\mathcal{N}(\mathbf{0}, \mathbf{I})$ is a zero mean Gaussian sequence with covariance matrix \mathbf{I} . In equation (5.15), α is a scalar representing the correlation between sources. $\alpha = 0$ means the sources are uncorrelated, while $\alpha = 1$ means the sources are completely correlated.

After applying the lead field matrix to the simulated moments, GWN was added to the generated MEG. The available noise power in the simulated MEG is measured by SNR in dB units which is defined as

$$SNR = 10\log(\frac{P_{signal}}{P_{noise}}) \tag{5.16}$$

where P_{signal} denotes the power of signal (simulated MEG), and P_{noise} denotes the power of added noise to the simulated MEG. In the following simulations, SNR = 5dB except in Section 5.3.1 and $\alpha = 0.5$ except in Section 5.3.1. The localization error for the major index to evaluate the performances is used. The error is defined as the Euclidean distance between the original and estimated source locations. The following results were obtained by running 200 Monte Carlo trials for each input.

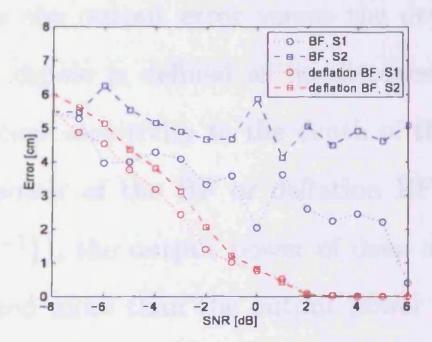


Figure 5.2: Output error vs. SNR when the sources are S1 and S2. The deflation BF (red lines) has considerably better performance compared to BF approach (blue lines) in the face of different value of SNRs.

Effects of Different SNR

Fig. 5.2 compares the effects of SNR on the performance of BF and deflation BF in terms of averaged localization error for the two sources. The source locations (S1 and

S2) are shown in Fig. 5.1. The deflation BF technique shows acceptable performance for high input SNRs and has perfect performance for SNR>2dB with an error close to zero. The BF approach failed to detect the dipoles, even in high input SNRs, due to the partial correlation between the sources. In high input SNRs, BF located both dipoles near to one dipole and in lower SNRs, it located the dipoles somewhere between the actual locations.

Effects of Depth

To investigate the effects of dipole depth, one source is assumed to be fixed on S3 and another source is assumed to move from start point S4 away from superficial location. The locations of S3 and S4 are shown in Fig. 5.1. The x and y coordinates of the second source are fixed and the same as those of S4, while its z coordinate decreases. Fig. 5.3 shows the output error versus the depth of the second dipole. The depth of the second dipole is defined as its distance from S4. Both BF and deflation BF techniques show sensitivity to the depth of the dipole. This is because by dividing the output power of the BF or deflation BF by the output power of the noise (i.e. $tr\{(\mathbf{H}^T\mathbf{H})^{-1}\}$), the output power of deep sources, which have larger $tr\{(\mathbf{H}^T\mathbf{H})^{-1}\}$, is attenuated more than the output power of the superficial sources. Therefore, deep sources show larger output error compared to the superficial sources. In E/MEG source localization this may be acceptable, since the observed data are mostly generated from the cortex (outer layer of the brain) rather than deep sources (this is especially true for MEG). Furthermore, Fig. 5.3 shows that the deflation BF method outperforms the BF method regardless of the depth of the source.

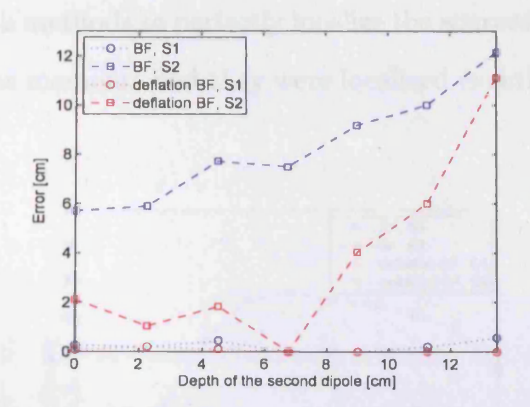


Figure 5.3: Investigation of depth of the source. The first source is fixed at S3. The second source has the same x and y coordinates as those of S4, while its z coordinate is decreasing. The horizontal axis is the distance between second source and S4. Both BF and deflation BF are sensitive to the depth of the source, however, deflation BF shows better performance.

Effects of Source Correlation

In Fig. 5.4, the effect of different levels of source correlation on localization accuracy for deflation BF and BF is shown. The source locations are S1 and S2 (see Fig. 5.1) and the SNR value was fixed to 5dB. The α value was varied from 0 to 1, which means the sources are uncorrelated first and then become completely correlated. Deflation BF has much lower sensitivity to the correlation between the sources and its error increases monotonically for both sources as the correlation increases.

When $0 < \alpha < 0.5$ the first source is accurately localized by the BF while the estimated location of the second source moves away from actual location and more towards the first source, as a result of which the error increases. When $0.5 < \alpha < 1$ the BF located the two sources between the original locations, and the error of the first source increases while the error of the second source decreases. This phenomenon is seen mainly because of the available noise in the data. In noise free data and for

 α < 1, we expect both methods to perfectly localize the sources. When α = 1, the two sources have the same moments and they were localized exactly between the original source locations.

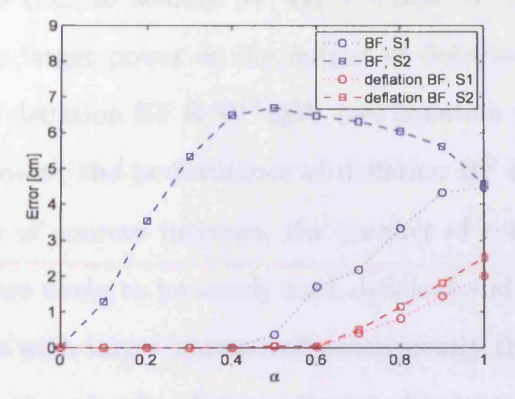


Figure 5.4: Output error vs. α for investigation of correlation between sources. $\alpha=0$ means two sources are uncorrelated and $\alpha=1$ means two sources have exactly the same moments (i.e. completely correlated). Deflation BF (red lines) has much less sensitivity to the correlation between sources in comparison with the BF (blue lines), and its error is monotonically increasing.

Effects of Distance Between Sources

Fig. 5.5 presents the localization errors of BF and deflation BF while the distance between the two simulated sources varies. The SNR level was 5dB and α was set to 0.3. The location of the first dipole is fixed at S3 and the location of the second dipole was moving in the y axis direction, whilst its x and z coordinates were fixed to those of S3. When the distance between dipoles is more than 4cm the deflation BF has better performance than BF. When the sources are closely spaced, however, BF outperforms deflation BF.

A possible reason for poorer performance of the deflation BF compared to BF in

this simulation would be amplifying the noise power at the output of deflation BF. As the sources are moved closer to each other, their lead field matrices also become closer in a linear algebraic sense. Therefore, \mathbf{W}^T takes weights with large norms to salsify both constraints (i.e. to achieve $\mathbf{W}^T\mathbf{H}_1=\mathbf{I}$ and $\mathbf{W}^T\mathbf{H}_2=\mathbf{0}$). Larger \mathbf{W}^T leads to a noise with a larger power at the output of deflation BF, since the noise power at the output of deflation BF is $\mathbf{W}^T\mathbf{Q}\mathbf{W}$ (see equation (5.14)). As a result of amplifying the noise power, the performance of deflation BF deteriorates compared to BF. As the number of sources increase, the number of constraint increases and $\tilde{\mathbf{H}}=[\mathbf{H}_1\ldots\mathbf{H}_q]$ is more likely to be nearly rank deficient and raising the possibility that \mathbf{W}^T takes weights with larger norms and consequently the poorer performance of the deflation BF. On the other hand, when the two dipoles are very close, they may behave as one dipole and the BF locates both dipoles near to the actual locations. In this case, the BF shows more precise localization than when the dipoles are far from each other. We may conclude here that the BF method outperforms the deflation BF method only when the sources are closely spaced.

Effects of Real Noise

The behavior of the algorithms in the presence of additive non-Gaussian noise was investigated. To study the effect of real noise, background MEG signals were added to the simulated data. The locations of dipoles are S1 and S2 as shown in Fig. 5.1. The results as a function of signal to background ratio (SBR) are displayed in Fig. 5.6. The SBR is defined as the ratio of power of the simulated data to the power of added background MEG in dB units. Both algorithms are robust for the first source in the face of real noise. For SBR>-4dB the deflation BF outperforms the BF method: the

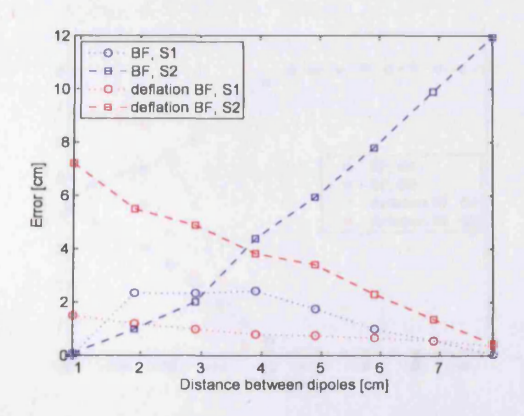


Figure 5.5: Investigation of distance between sources. The first source is fixed at S3 and the second source has the same x and z coordinates as those of S3, while its y coordinate is increasing. The horizontal axis is the distance between two sources. When the distance between sources is more than 4cm, deflation BF (red lines) has better performance than BF (blue lines), however, when the sources have distance less than 3cm the BF outperforms deflation BF.

BF again failed to detect the second dipole, while the deflation BF detected both dipoles successfully.

5.3.2 Simulated MEG Localization

To simulate MEG signals, three dipoles were used. Their locations are shown in Fig. 5.7. All sources have the same z coordinate, and this enables us to illustrate the output powers of BF and deflation BF on a two-dimensional graph. Here, two examples which have different moments are given. In the first example, three sources are correlated and a large peak between the three sources in the BF power profile is seen. In the next example, one source has larger power and a peak near the location of the strongest source in the BF power profile is seen. In both examples, however, the deflation BF could successfully localize the three sources with less than four iterations

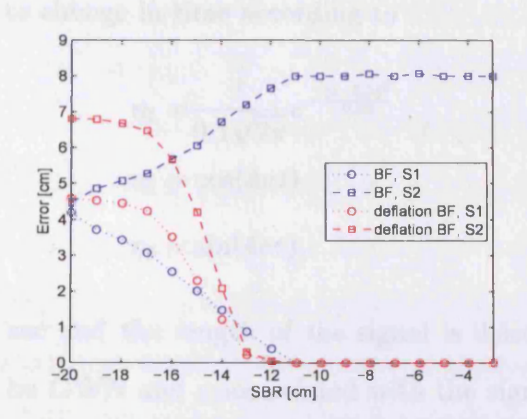


Figure 5.6: Output error vs. SBR for investigation of effect of real noise. Real background MEG has been added to the simulated data. Deflation BF (red lines) outperforms BF method (blue lines), and indeed is robust to the non-Gaussian noise.

(K < 4).

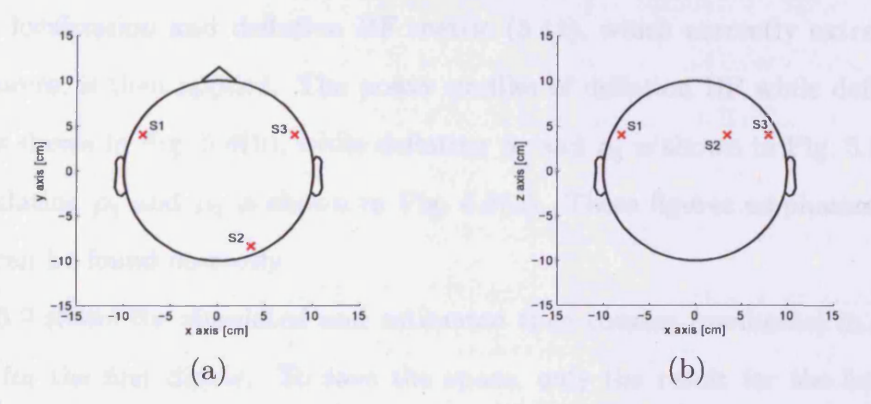


Figure 5.7: Location of three dipoles used for MEG simulation in (a) axial view and (b) coronal view.

In the first example, the dipole components are defined as $\mathbf{m}_t(\boldsymbol{\rho_1}) = [0.4\eta_1, \ \eta_2, \ \eta_3]^T$, $\mathbf{m}_t(\boldsymbol{\rho_2}) = [\eta_2, \eta_3, \ 0.4\eta_1]^T$ and $\mathbf{m}_t(\boldsymbol{\rho_3}) = [\eta_3, \ 0.4\eta_1, \eta_2]^T$ where the magnitudes of η_1 ,

 η_2 and η_3 are allowed to change in time according to

$$\eta_1 = \frac{1}{0.1\sqrt{2\pi}} e^{-\frac{(t-0.3)^2}{0.02}}
\eta_2 = \cos(4\pi t)
\eta_3 = \sin(4\pi t)$$
(5.17)

The time unit t is in sec and the length of the signal is 0.5sec. Again, the added noise was assumed to be GWN and uncorrelated with the signal with SNR = 5dB. The standard BF metric (5.4) for each grid point was computed and the result is shown in Fig. 5.8(a). Note that since the sources are correlated, one peak (which is the cumulative result of all dipoles) represents all of the sources. Hence, the BF approach locates the three dipoles between the three actual dipole locations. The iterative localization and deflation BF metric (5.11), which correctly extracted the three sources, is then applied. The power profiles of deflation BF while deflating ρ_2 and ρ_3 is shown in Fig. 5.8(b), while deflating ρ_1 and ρ_3 is shown in Fig. 5.8(c), and while deflating ρ_1 and ρ_2 is shown in Fig. 5.8(d). These figures emphasize that all sources can be found correctly.

Fig. 5.9 shows the simulated and estimated time courses (moments) in three directions for the first dipole. To save the space, only the result for the first dipole is shown. Fig. 5.9(a) shows the result obtained by the BF method and Fig. 5.9(b) shows the result for the deflation BF method. The simulated and estimated moments are depicted by dotted and solid lines, respectively. Since the BF method was unsuccessful in localizing the sources, the estimated moments do not correspond with the simulated moments. However, the deflation BF shows accurate albeit noisy variation of the moments over time.

In the next example, the dipole components were defined as $\mathbf{m}_t(\boldsymbol{\rho}_1) = [0, 0.3\eta_1, 0.7\eta_3]^T$, $\mathbf{m}_t(\boldsymbol{\rho}_2) = [0, 0.3\eta_2, 0]^T$ and $\mathbf{m}_t(\boldsymbol{\rho}_3) = [0, \eta_3, 0.3\eta_1]^T$, where η_1 , η_2 and η_3 are given in equation (5.17). SNR and α values were set to 5dB and 0.5, respectively. The standard BF metric (5.4) for each grid point was computed and the result is shown in Fig. 5.10(a). In this figure, only one peak was allocated to $\boldsymbol{\rho}_1$ which has the largest power. Thus, the BF approach misallocates the two other dipole locations to the dominant dipole location. The iterative localization and deflation BF metric (5.11) is also applied to data and could extract the three sources successfully. The power profiles of deflation BF while deflating all possible pairing of $\boldsymbol{\rho}_1$, $\boldsymbol{\rho}_2$ and $\boldsymbol{\rho}_3$ is shown in Figs. 5.10(b), (c) and (d). In these figures, the power profiles for the three sources show perfect peaks for localization.

Fig. 5.11 (similar to Fig. 5.9) shows the simulated and estimated moments in three directions for the first dipole. The BF method again was unsuccessful in revealing correct variation of moments in all directions. In contrast, the deflation BF accurately tracks the variation in the moments over time.

These examples were included to demonstrate the high potential of deflation BF in higher dimensional source localization problems, and to emphasize that the method can cope when there are correlated sources, as well as when one source dominates the others.

5.4 Application to Auditory ERF

In order to assess the proposed technique for real data, event-related fields (ERFs) were recorded in an auditory paradigm. 1500 auditory stimuli were delivered every 0.5sec bilaterally to the subject. The stimulus was a broadband noise lasting 0.1sec.

This data set was selected because the stimulus train generates activity in the left and right primary auditory cortices. The data was acquired from a 28 year old male subject. Whole head MEG recordings were made using a 275-channel radial gradiometer system (VSM MedTech, Canada). An additional 29 reference channels were recorded for noise cancellation purposes and the primary sensors were analyzed as synthetic third order gradiometers [114]. The sampling rate was 1000Hz and recordings were filtered off-line with a bandpass of 0.03 to 40Hz. Intra-individual head movement was kept to a minimum, and head position was localized at the start and finish of the study. ERFs were epoched off-line with a 0.1sec pre-stimulus baseline correction. After visual rejection of trials containing eyeblink and movement artifacts, the remaining trials were averaged and the result is shown in Fig 5.12. The estimated noise covariance matrix C_v , which was used in both the BF and the deflation BF approaches, was calculated from the 0.1sec pre-stimulus segments.

In this experiment, the number of dipoles was assumed to be two (one in the right and one in the left hemisphere of the brain). Figs. 5.13(a) and (b) show the power profile of the BF and the estimated locations in axial and coronal views. The estimated locations are shown with cross markers. The estimated power profile and the estimated locations using the deflation BF method are shown in Figs. 5.13(c)-(f). Figs. 5.13(c) and (d) show the location of the first dipole while deflating the second dipole, and Figs. 5.13(e) and (f) show the location of the second dipole while deflating the first dipole. The deflation BF method converged after three iterations (K = 3).

For BF, Figs. 5.13(a) and (b) show that the sources are bleeding towards the center of the head due to the partial correlation between the sources. On the other hand, the deflation BF places the sources at biologically plausible locations in the

primary auditory cortices in the left and right hemisphere. The power obtained using the deflation BF is also more focal than the power obtained using the BF approach. Furthermore, no spurious activations near the center of the sphere model were observed implementing the deflation BF method.

Fig. 5.14 depicts the estimated moments in three directions for both dipoles. The results using BF and deflation BF are denoted by dotted and solid lines, respectively. Since the BF method mis-localizes the sources between the actual source locations, its moments have bigger amplitudes compared to those obtained by deflation BF.

These observations verify superior performance for the deflation BF method over the BF method, emphasizing that the deflation BF is likely to be a better choice than BF in practical applications.

5.5 Conclusions

A new approach for multiple dipole E/MEG source localization based on the BF approach was developed. A new constraint, which minimizes the noise power at the output of the filter, was included within the BF formulation. Another constraint was also added to the BF formulation as a result of which identified locations are deflated and other sources are, as a consequence, located more precisely. The multiple constrained problem was solved using the Lagrange multiplier method and the results were normalized to the power profile of noise only. Furthermore, an iterative deflation and localization method was proposed to improve the performance of the method. It was shown that the proposed deflation BF method has no dependency on the correlation between the sources. The method is also useful when the classical BF identifies all the locations around the dominant source. Several metrics affected by

SNR, correlation, depths of dipoles, distance between dipoles, and finally real noise, were discussed to show the superior performance of the proposed deflation BF over BF. Only when the sources are very close does the BF outperform the deflation BF. Unfortunately, both BF and deflation BF are still sensitive to the depth of sources.

In the next chapter a new method for dipole source localization is also proposed. The method is based on PF and in contrast to the current method, it can deal with non-stationarity of the E/MEG data.

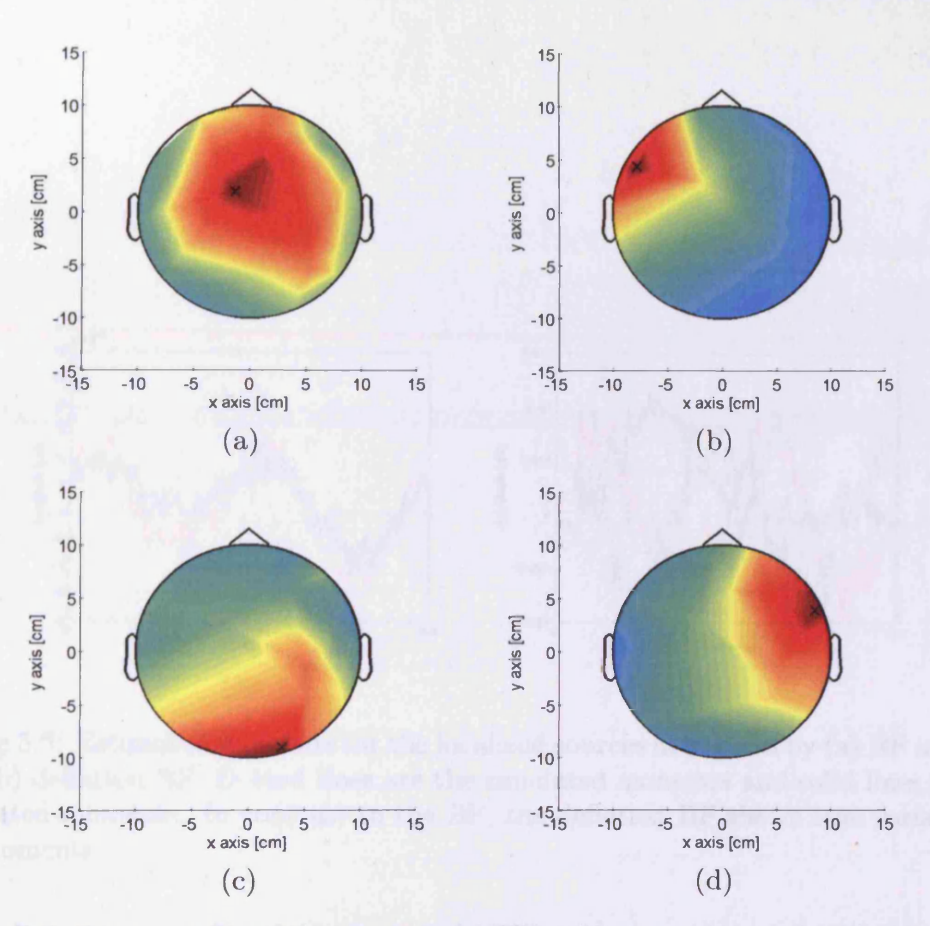


Figure 5.8: Power profile of the simulated MEG, when sources are strongly correlated using (a) BF method, (b) deflation BF method while deflating the second and third dipoles, (c) deflation BF method while deflating the first and third dipoles, and (d) deflation BF method while deflating the first and second dipoles. Due to correlation between the sources, BF method shows activation between three actual sources. Three power profiles obtained by deflation BF show that deflation BF has been successful to identify the three sources.

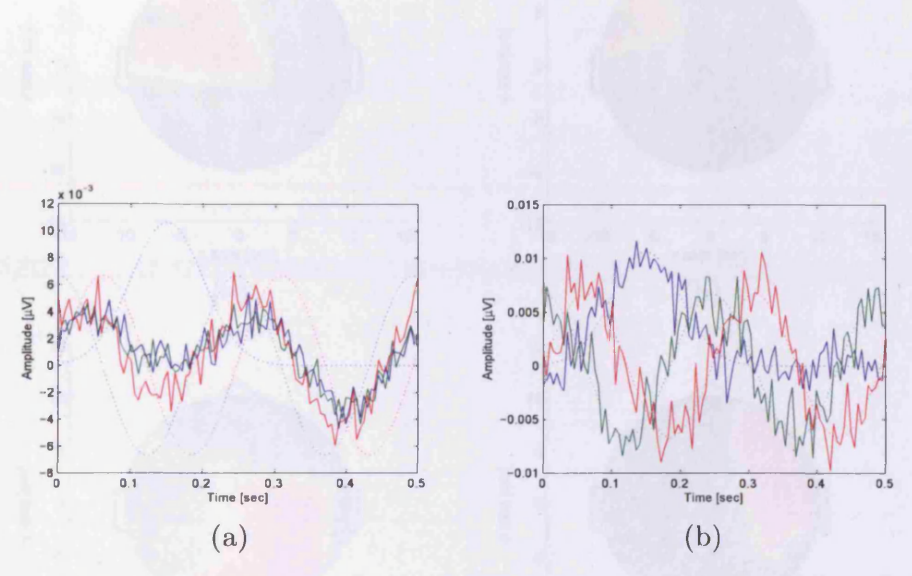


Figure 5.9: Estimated moments for the localized sources in Fig. 5.8 by (a) BF method, and (b) deflation BF. Dotted lines are the simulated moments and solid lines are the estimated moments. In contrast to the BF, the deflation BF shows true variation of the moments.

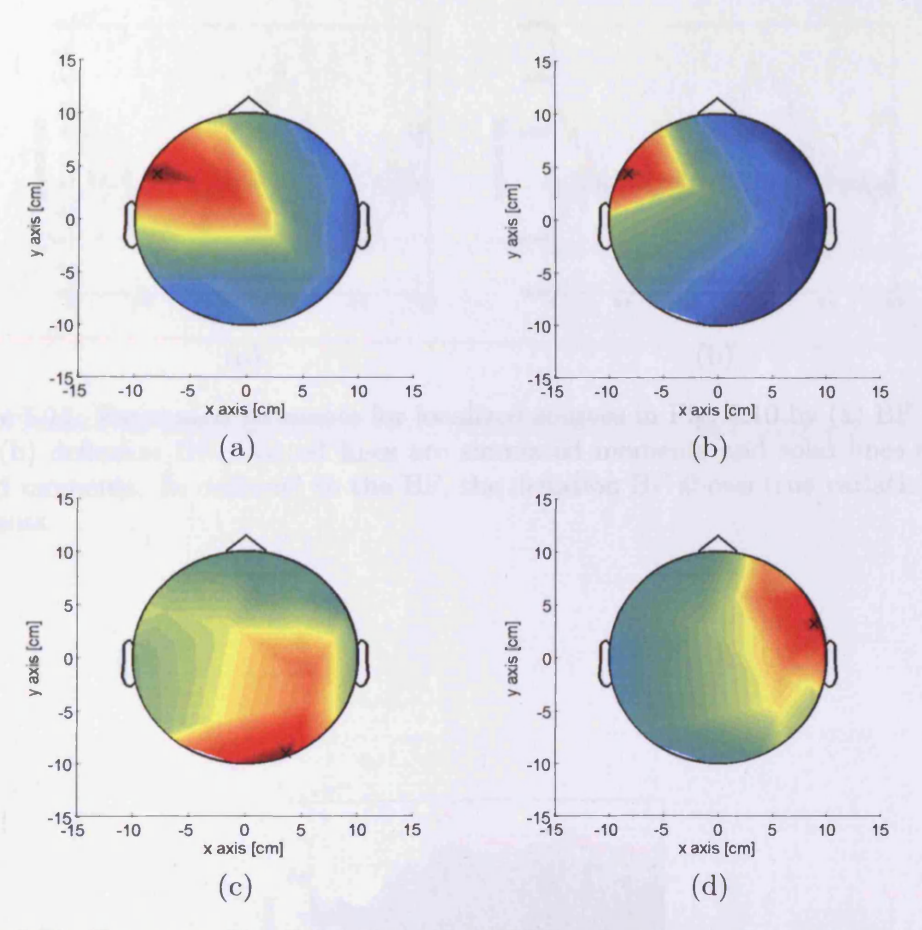


Figure 5.10: Power profile of the simulated MEG, when one source dominates others using (a) BF method, (b) deflation BF method while deflating the second and third dipoles, (c) deflation BF method while deflating the first and third dipoles, and (d) deflation BF method while deflating the first and second dipoles. In the BF approach one source dominates others and other sources are not reconstructed. The deflation BF method, however, reconstructs all the sources in three power profile images successfully.

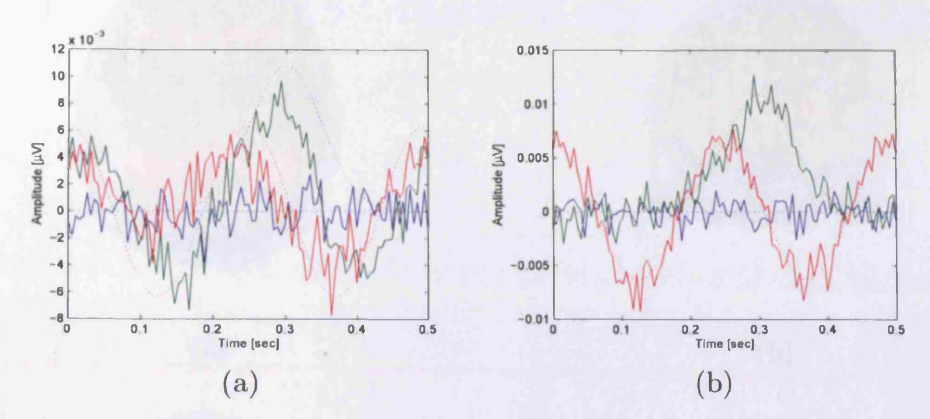


Figure 5.11: Estimated moments for localized sources in Fig. 5.10 by (a) BF method and, (b) deflation BF. Dotted lines are simulated moments and solid lines are estimated moments. In contrast to the BF, the deflation BF shows true variation of the moments.

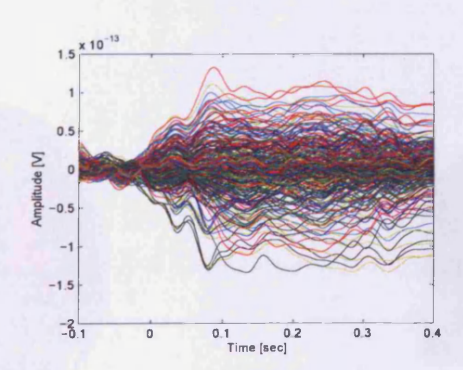


Figure 5.12: The averaged auditory ERFs over 1500 trials. A 0.1sec pre-stimulus was used for baseline corrections.

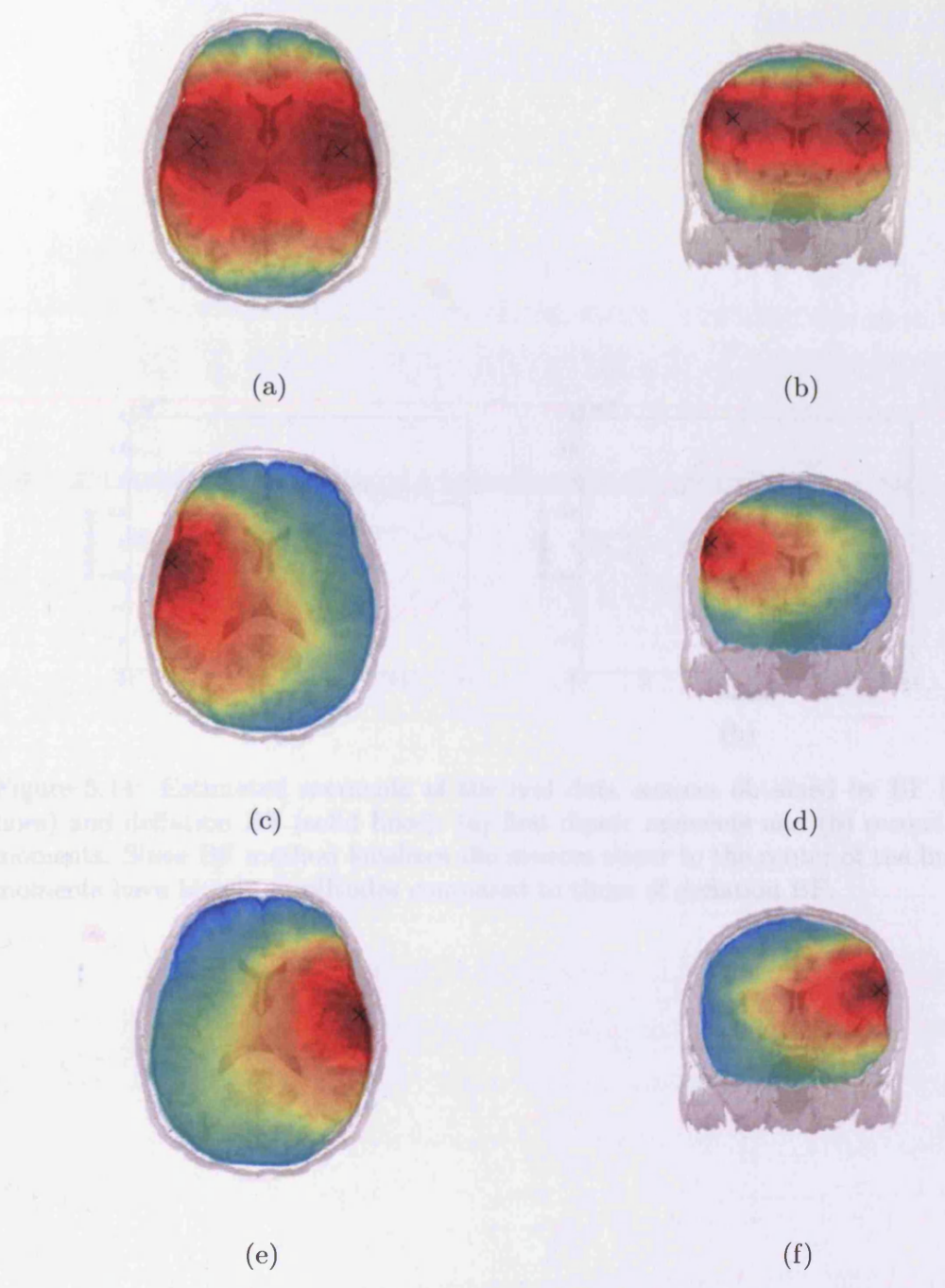


Figure 5.13: Power profile of real data obtained using (a) BF method in axial view, (b) BF method in coronal view, (c) deflation BF while deflating the second source in axial view, (d) deflation BF while deflating the second source in coronal view, (e) deflation BF while deflating the first source in axial view, and (f) deflation BF while deflating the first source in coronal view. The estimated source locations are shown by cross markers. Due to partial correlation between the sources, the BF method shows that the location of dipoles are bleeding towards the center of the head. The deflation BF, however, shows the true location of dipoles on the primary auditory cortex.

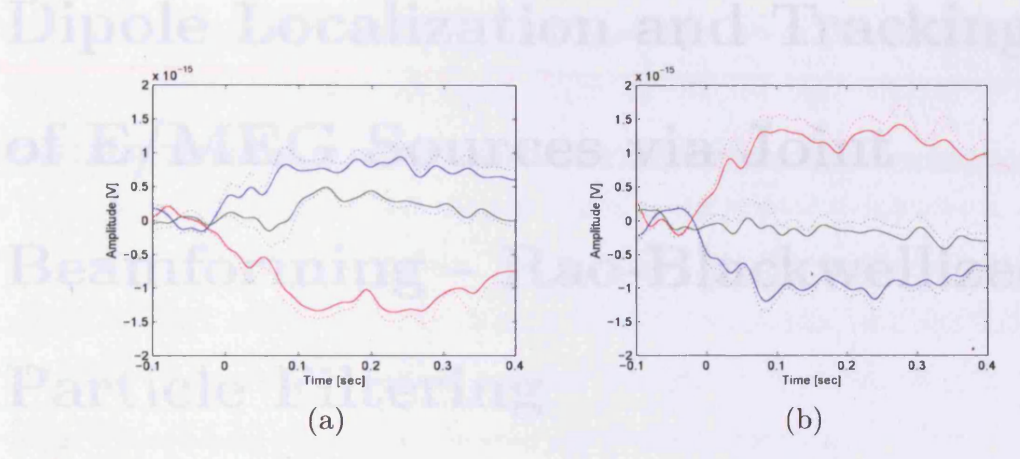


Figure 5.14: Estimated moments of the real data sources obtained by BF (dotted lines) and deflation BF (solid lines); (a) first dipole moments and (b) second dipole moments. Since BF method localizes the sources closer to the center of the brain, its moments have bigger amplitudes compared to those of deflation BF.

Chapter 6

Dipole Localization and Tracking of E/MEG Sources via Joint Beamforming - Rao-Blackwellized Particle Filtering

6.1 Introduction

In the previous chapter the BF method for dipole source localization was generalized. In this chapter it is intended to present a method based on Rao-Blackwellized particle filtering (RBPF) for E/MEG dipole source localization. The RBPF improves the performance of PF by marginalizing out and estimating the linear part (the moments) using KF and estimating the nonlinear part (locations) using PF. As long as

the moments have a linear relation to the measurements, KF is an optimum solution. Therefore Rao-Blackwellization is an improvement to PF not only in terms of accuracy, but also in terms of computational time and memory usage. Utilization of RBPF for E/MEG dipole source localization can be found in [12, 75].

In addition, a linear BF (similar to the LCMV-BF) that can be employed in combination with RBPF is proposed. The BF is a linear spatial filter which passes the activity at a desired location while stopping the activity at other locations at each time sample. The combined BF and RBPF method, which is called beamforming RBPF (B-RBPF) is particularly useful for coping with the main deficiency of RBPF, which is its sensitivity to the assumed number of dipoles.

The methods are grid based methods which can be applied to spherical as well as geometrically realistic head models. The grid based methods can decrease considerably the computational time and memory usage in comparison with non grid based methods. The grid based methods can also be applied to a realistic head model for which a closed-form solution for forward problem does not exist.

In the following sections the inverse problem is first formulated in state space and then the RBPF is established for multiple dipole localization. In Section 6.2.2 the proposed joint PF and BF method based on subspace denoising and BF is explained. Various simulations are presented in Section 6.3.2 and the results for B-RBPF, RBPF, RAP-MUSIC and BF methods are given. This section also contains same simulated examples for tracking of moving dipoles using the RBPF and B-RBPF methods.

6.2 Methods

6.2.1 Problem Formulation in State Space

Let \mathbf{y}_t be a $L \times 1$ vector composed of the electric potentials measured from L electrodes at time t. The measured potential at the scalp \mathbf{y}_t is assumed to be a superposition of potentials from q source dipoles. Let the medium between the dipoles and the electrodes be homogeneous. Therefore \mathbf{y}_t can be modeled as:

$$\mathbf{y}_t = \sum_{i=1}^q \mathbf{H}(\boldsymbol{\rho}_t(i))\mathbf{m}_t(i) + \mathbf{v}_t.$$
 (6.1)

where $\rho_t(i)$ is the three-dimensional location and $\mathbf{m}_t(i)$ is the three-dimensional moment of the *i*th dipole at time *t*. Here, \mathbf{v}_t represents the additive noise, which is uncorrelated with the source activities and \mathbf{H} is the gain or lead field matrix, which is a nonlinear function of dipole locations. The gain matrix \mathbf{H} can be calculated in a spherical head model with three skull, scalp and skin layers, or can be obtained using a realistic head model. The aim is to estimate the dipole locations and moments based on the measurements and upon prior knowledge about the number of dipoles.

For the sake of convenience, a $3 \times q$ matrix of locations $\mathbf{R}_t = [\boldsymbol{\rho}_t(1) \dots \boldsymbol{\rho}_t(q)]$, a $3q \times 1$ vector of moments $\underline{\mathbf{m}}_t = [\mathbf{m}_t(1) \dots \mathbf{m}_t(q)]^T$ and an $L \times 3q$ matrix of gain matrices $\underline{\mathbf{H}}(\mathbf{R}_t) = [\mathbf{H}(\boldsymbol{\rho}_t(1)) \dots \mathbf{H}(\boldsymbol{\rho}_t(q))]$ are defined. Equation (6.1), therefore, can be reformulated in matrix form as

$$\mathbf{y}_t = \mathbf{H}(\mathbf{R}_t)\mathbf{m}_t + \mathbf{v}_t. \tag{6.2}$$

The aim is to find filtered estimations of dipole locations and dipole moments.

Thus, the state \mathbf{x}_t is defined as $\mathbf{x}_t = [\mathbf{R}_t \ \underline{\mathbf{m}}_t]^T$ and since the location part is nonlinear, the distribution of the state variables \mathbf{x}_t can be estimated by PF. However, by increasing the number of dipoles q, the number of parameters to be estimated is increased (six parameters for each dipole) and therefore, the estimation using only PF can be inefficient since a large number of particles are needed to represent the posteriori distribution. A standard technique to increase the efficiency of the PF, which is called Rao-Blackwellization [29], reduces the state space by marginalizing out some of the variables. The idea of RBPF is to estimate some of the state's variables using PF and to estimate the rest using other estimators such as KF. Therefore, in RBPF the state \mathbf{x}_t is partitioned into \mathbf{R}_t and \mathbf{m}_t subspaces. By assuming that the moments and locations are independent, using the chain rule of probability it can be written

$$p(\mathbf{x}_t|\mathbf{y}_{1:t}) = p(\mathbf{m}_t|\mathbf{R}_t, \mathbf{y}_{1:t})p(\mathbf{R}_t|\mathbf{y}_{1:t})$$
(6.3)

Since the moments are linearly related to the measurements (see equation (6.2)) only the distribution of the nonlinear part $p(\mathbf{R}_t|\mathbf{y}_{1:t})$ needs to be estimated using standard PF, and the distribution of the linear part $p(\mathbf{\underline{m}}_t|\mathbf{R}_t,\mathbf{y}_{1:t})$ is updated analytically and efficiently using KF.

For estimating the locations, using equation (6.2), the state space formulations for dipole locations \mathbf{R}_t have the forms

$$\mathbf{R}_{t} = \mathbf{R}_{t-1} + \mathbf{w}_{t-1}^{\rho} \tag{6.4}$$

$$\mathbf{y}_t = \mathbf{H}(\mathbf{R}_t)\mathbf{m}_t + \mathbf{v}_t^{\rho} \tag{6.5}$$

where \mathbf{w}_t^{ρ} and \mathbf{v}_t^{ρ} are zero mean GWN location noises with empirically known covariance matrices \mathbf{Q}_w^{ρ} and \mathbf{Q}_v^{ρ} , respectively. In equation (6.4), the transition of the state is assumed to be a random walk process. This means that the estimation of current dipole location depends on those estimated from the previous samples. This is an acceptable assumption, since the state of the brain does not have extensive variability from one time sample to another.

For estimating the moments, the state space equations for subspace $\underline{\mathbf{m}}_t$ are given as

$$\underline{\mathbf{m}}_t = \underline{\mathbf{m}}_{t-1} + \mathbf{w}_{t-1}^m \tag{6.6}$$

$$\mathbf{y}_t = \mathbf{\underline{H}} \ \mathbf{\underline{m}}_t + \mathbf{v}_t^m \tag{6.7}$$

where \mathbf{w}_{t-1}^m and \mathbf{v}_t^m are zero mean GWN moment noises with empirically known covariance matrices \mathbf{Q}_w^m and \mathbf{Q}_v^m , respectively. To simplify the notation, $\underline{\mathbf{H}}$ is used instead of $\underline{\mathbf{H}}(\mathbf{R}_t)$ and in the rest of the chapter the same notation is employed. Again the transition of the moments is assumed to be a random walk process. Given the dipole location \mathbf{R}_{t-1} (hence, $\underline{\mathbf{H}}$) and measurement \mathbf{y}_t , the mean vector $\boldsymbol{\mu}_t^m$ and the covariance matrix \mathbf{P}_t^m of moments $\underline{\mathbf{m}}_t$ are updated using Kalman updates [40]. Rewriting the Kalman equation for state space (6.6) and (6.7) results:

$$\mathbf{P}_{t|t-1}^{m} = \mathbf{P}_{t-1}^{m} + \mathbf{Q}_{w}^{m} \tag{6.8}$$

$$\mathbf{K}_{t} = \mathbf{P}_{t|t-1}^{m} \underline{\mathbf{H}}^{T} (\underline{\mathbf{H}} \mathbf{P}_{t|t-1}^{m} \underline{\mathbf{H}}^{T} + \mathbf{Q}_{v}^{m})^{-1}$$

$$(6.9)$$

$$\boldsymbol{\mu}_t^m = \boldsymbol{\mu}_{t-1}^m + \mathbf{K}_t(\mathbf{y}_t - \underline{\mathbf{H}}\boldsymbol{\mu}_{t-1}^m)$$
(6.10)

$$\mathbf{P}_{t}^{m} = \mathbf{P}_{t|t-1}^{m} - \mathbf{K}_{t} \underline{\mathbf{H}} \mathbf{P}_{t|t-1}^{m} \tag{6.11}$$

where $\mathbf{P}_{t|t-1}^m$ is the covariance matrix of the conditional pdf $p(\underline{\mathbf{m}}_t|\mathbf{R}_{t-1},\mathbf{y}_{t-1})$, and \mathbf{K}_t is called Kalman gain.

In RBPF, each particle maintains not only a sample from $p(\mathbf{R}_t|\mathbf{y}_{1:t})$, which is denoted by $\mathbf{R}_t^{(n)}$, but also a parametric representation of the distribution $p(\underline{\mathbf{m}}_t|\mathbf{R}_t,\mathbf{y}_{1:t})$, which is denoted by mean vector $\boldsymbol{\mu}_t^{m(n)}$ and covariance matrix $\mathbf{P}_t^{m(n)}$ of the moments.

The proposed method is a grid based method, which means the brain is divided into sufficiently small three-dimensional grid cells and the location of each dipole is restricted to one of these cells. Therefore, before updating the weights, the locations indicated by each particle may not be one of those grid cells and they are replaced by the nearest cells. The grid based method helps the use of real head model and any form of forward solution. Moreover, depending on the number of grid cells, the computational complexity decreases considerably compared to non grid based methods. The pseudo-code for this algorithm is presented in Algorithm 3. In this algorithm, generating random vectors according to the uniform distribution means producing or drawing random vectors that have the same distribution as the uniform distribution.

6.2.2 A Beamforming - RBPF in Time and Space Domains (B-RBPF)

In this section a method to improve the RBPF approach in time and space domains is established. In the time domain the measurement is denoised using SVD and in the space domain the LCMV-BF is reformulated to spatially denoise the measurement at each time sample.

The algorithm is implemented as follows. First, the data is windowed around time

Algorithm 3 Pseudo-code of RBPF for localizing multiple dipoles

set t = 0 and generate random vectors $\mathbf{R}_0^{(n)}$ according to random uniform distribu-

set $\mu_0^{m(n)} = \mathbf{o}$ and $\mathbf{P}_0^{m(n)} = \mathbf{I}$. {o is a vector of zeros and \mathbf{I} is the identity matrix} for t = 1 to T do {T is the length of the signals}

- generate random numbers $\mathbf{w}_t^{\rho(n)} \sim \mathcal{N}(\mathbf{0}, \mathbf{Q}_w^{\rho})$ and set $\mathbf{R}_t^{(n)} = \mathbf{R}_{t-1}^{(n)} + \mathbf{w}_t^{\rho(n)}$.

 replace column of $\mathbf{R}_t^{(n)}$ with the coordinate of nearest grid cell.

 update new weights $\mathbf{w}_t^{(n)} = \mathbf{w}_{t-1}^{(n)} \mathcal{N}(\mathbf{y}_t | \tilde{\mathbf{R}}_t^{(n)}, \mathbf{Q}_v^{\rho})$.

 normalize the weights $\mathbf{w}_t^{(n)} = \mathbf{w}_t^{(n)} / \sum_{n=1}^{N} \mathbf{w}_t^{(n)}$.

 update $\boldsymbol{\mu}_t^{m(n)}$ and $\mathbf{P}_t^{m(n)}$ given $\mathbf{R}_t^{(n)}$ and \mathbf{y}_t for each particle using equation
- resample new N particles $\mathbf{R}_t^{(n)}$ from the $\tilde{\mathbf{R}}_t^{(n)}$ with replacement according to their importance weights $w_t^{(n)}$.

end for

t using a window of length M which results in an $M \times L$ matrix Y_t . The mth row of \mathbf{Y}_t is given by $h_m \mathbf{y}_{t-\frac{M+1}{2}+m}$, where $h_m = 0.54 - 0.46 \cos(\frac{2\pi m}{M-1})$ is the mth point of a Hamming window. To stabilize and denoise the measurements, y_t is replaced by

$$\mathbf{y}_t^d = \mathbf{Y}_t^T \mathbf{u}_{max} \tag{6.12}$$

where \mathbf{u}_{max} is the $M \times 1$ left singular vector corresponding to the maximum singular value obtained by SVD. This method is similar to subspace methods in which the signal subspaces are chosen according to the largest singular values. The length of the window M can be chosen according to the data as long as it is stationary. In most cases, E/MEG can be assumed to be stationary during a small window length since the state of the brain does not vary extensively.

Another improvement is made by applying a narrowband BF to the RBPF and so the method is called beamformer RBPF (B-RBPF). BF is a spatial filter that passes signals originating from a small passband volume while attenuating those originating from other locations.

Consider the signals coming from locations $\check{\rho} = \{\rho_t(i)|i=1,\ldots,q\}$ as the signal of interest and the rest as noise. In addition, suppose the recorded windowed E/MEG can be decomposed as:

$$\mathbf{y}_t^d = \sum_{\boldsymbol{\rho}_t(i) \in \check{\boldsymbol{\rho}}} \mathbf{H}(\boldsymbol{\rho}_t(i)) \mathbf{m}_t(i) + \sum_{\boldsymbol{\rho}_t(i) \notin \check{\boldsymbol{\rho}}} \mathbf{H}(\boldsymbol{\rho}_t(i)) \mathbf{m}_t(i). \tag{6.13}$$

We are looking for an $L \times L$ linear spatial filter $\mathbf{W}_{\check{p}}$ which passes signals coming from \check{p} and suppresses the rest. Therefore, the filter $\mathbf{W}_{\check{p}}$ should have the following ideal response:

$$\mathbf{W}_{\check{\rho}}^{T}\mathbf{y}_{t}^{d} = \sum_{\boldsymbol{\rho}_{t}(i)\in\check{\rho}} \mathbf{W}_{\check{\rho}}^{T}\mathbf{H}(\boldsymbol{\rho}_{t}(i))\mathbf{m}_{t}(i) + \sum_{\boldsymbol{\rho}_{t}(i)\not\in\check{\rho}} \mathbf{W}_{\check{\rho}}^{T}\mathbf{H}(\boldsymbol{\rho}_{t}(i))\mathbf{m}_{t}(i) = \sum_{\boldsymbol{\rho}_{t}(i)\in\check{\rho}} \mathbf{H}(\boldsymbol{\rho}_{t}(i))\mathbf{m}_{t}(i)$$
(6.14)

equation (6.14) results in

$$\mathbf{W}_{\check{\rho}}^{T}\mathbf{H}(\boldsymbol{\rho}_{t}(i)) = \begin{cases} \mathbf{H}(\boldsymbol{\rho}_{t}(i)) & \boldsymbol{\rho}_{t}(i) \in \check{\boldsymbol{\rho}} \\ \mathbf{O} & \boldsymbol{\rho}_{t}(i) \notin \check{\boldsymbol{\rho}} \end{cases}$$
(6.15)

where O is a $L \times 3q$ null matrix. The linear filter $\mathbf{W}_{\tilde{\rho}}$ cannot exactly satisfy both conditions simultaneously unless $M + 3q \leq N$. One solution, therefore, could be finding a $\mathbf{W}_{\tilde{\rho}}$ that satisfies a linear response constraint $\mathbf{W}_{\tilde{\rho}}^T\mathbf{H}(\rho_t(i)) = \mathbf{H}(\rho_t(i))$ based on the first condition and minimizes the power at the filter output $\|\mathbf{W}_{\tilde{\rho}}^T\mathbf{y}_t^d\|$ based on the second condition. The constraint ensures that the signals of interest are passed through the filter. Minimization of the output power of the filter optimally

allocates the stop band response of the filter to minimize the contribution of sources from other locations. The solution is given in Appendix A and the result is

$$\mathbf{W}_{\tilde{\boldsymbol{\rho}}}^{T} = \underline{\mathbf{H}} \left[\underline{\mathbf{H}}^{T} \mathbf{C}_{\boldsymbol{y}}^{-1} \underline{\mathbf{H}} \right]^{-1} \underline{\mathbf{H}}^{T} \mathbf{C}_{\boldsymbol{y}}^{-1}$$
(6.16)

where C_y is the covariance matrix of the data which may be obtained using matrix \mathbf{Y}_t at each sample time t. By applying this filter to the measured E/MEG, the spatial noise is reduced and as a result a better estimations of the dipole locations and moments is obtained. Since PF is a Monte Carlo method, it employs any combination of the sources with large likelihood to compute the posteriori distribution. Therefore, in multiple source localization the $\mathbf{H}^T \mathbf{C}_y^{-1} \mathbf{H}$ may not be full rank for some locations and then will not be invertible. Thus, $\mathbf{H}^T \mathbf{C}_y^{-1} \mathbf{H} + \lambda \mathbf{I}$, where λ is a small scalar, can be used to compute the inverse. If the subspace spanned by the original gain matrices of sources can be spanned by that of other source combinations, there will be an ambiguity and the sources can not be distinguished.

After applying the BF to the measurements, the available noise may not be GWN. Fortunately, the PF has the ability to employ any kind of noise with known distribution. However, for estimation of the moments using KF, the noise should be considered as GWN with a known covariance matrix. In this case if the noise distribution is known or estimated, the PF could be employed instead of KF.

The fundamental objective of the B-RBPF is to use the spatially filtered data instead of the original measurements to estimate the moment vector $\underline{\mathbf{m}}_t$ using Kalman updates. The matrix $\mathbf{W}_{\tilde{\rho}}^T$ in equation (6.16) is constructed for each particle using the locations indicated by particles provided from the previous step. The pseudo-code for this algorithm is presented in Algorithm 4.

Algorithm 4 Pseudo-code of B-RBPF for localizing multiple dipoles

```
set t=0 and generate random numbers \mathbf{R}_0^{(n)} according to the random uniform distribution.

set \boldsymbol{\mu}_0^{m(n)} = \mathbf{o} and \mathbf{P}_0^{m(n)} = \mathbf{I}.

for t=1 to T do \{T is the length of the signals\}

- generate random vectors \mathbf{w}_t^{(n)} \sim \mathcal{N}(\mathbf{0}, \mathbf{Q}_w^{\rho}) and set \mathbf{R}_t^{(n)} = \mathbf{R}_{t-1}^{(n)} + \mathbf{w}_t^{(n)}.

- replace column of \mathbf{R}_t^{(n)} with the coordinate of nearest grid cell.

- calculate \mathbf{y}_t^d using equation (6.12).

- compute \mathbf{W}_{\tilde{\rho}}^T using equation (6.16) for each particle.

- update \boldsymbol{\mu}_t^{m(n)} and denoised measurements \mathbf{P}_t^{m(n)} given \mathbf{R}_t^{(n)} and \mathbf{W}_{\tilde{\rho}}^T\mathbf{y}_t^d for each particle using equation (14)-(17).

- update new weights \mathbf{w}_t^{(n)} = \mathbf{w}_{t-1}^{(n)} \mathcal{N}(\mathbf{y}_t^d | \tilde{\mathbf{R}}_t^{(n)}, \mathbf{Q}_v^{\rho}).

- normalize the weights \mathbf{w}_t^{(n)} = \mathbf{w}_{t-1}^{(n)} \mathcal{N}(\mathbf{y}_t^d | \tilde{\mathbf{R}}_t^{(n)}, \mathbf{Q}_v^{\rho}).

- resample new N particles \mathbf{R}_t^{(n)} from the \tilde{\mathbf{R}}_t^{(n)} with replacement according to their importance weights \mathbf{w}_t^{(n)}.
```

The proposed filter has a similar formulation to the LCMV-BF. In the LCMV-BF the search is for a filter that estimates the power of the source at each location, thus $\mathbf{W}^T \underline{\mathbf{H}} = \mathbf{I}$ is used as the constraint (see equation (6.19)). In the proposed method, a filter that denoises the data without changing its dimension is desired. Only after applying this filter can KF be used subsequently. Therefore, $\mathbf{W}^T \underline{\mathbf{H}} = \underline{\mathbf{H}}$ is employed as the constraint.

6.3 Simulation Results

In this section, the results of the proposed methods are compared with those obtained using RAP-MUSIC and BF algorithms. These are well established methods in dipole source localization and often used as benchmarks. Both of them use second order statistics of the data which assume that the E/MEG data is temporally

and spatially stationary. There is, however, evidence that E/MEG is not generally stationary [95]. In the following sections, a brief review of the RAP-MUSIC and beamforming approaches is given prior to description of the comparisons carried out for several different simulations.

6.3.1 MUSIC, RAP-MUSIC, and BF

In the MUSIC method, the measured E/MEG is partitioned into noise-only and signal subspaces using SVD. The MUSIC algorithm [79] defines the source locations as those for which the corresponding gain vector $\alpha(\rho_i) = \mathbf{H}(\rho_i)\mathbf{m}_i$ is nearly orthogonal to the noise-only subspace or, equivalently, projects almost entirely into the signal subspace. The implementation of the algorithm is straightforward, and the first dipole location with Schmidt's metric is obtained as follows [79]:

$$\rho_1 = \arg\max_{\rho} \ subcorr(\mathbf{H}(\rho), \Phi_s) = \lambda_{max}(\mathbf{U}_{\mathbf{H}(\rho)}^T \Phi_s \Phi_s^T \mathbf{U}_{\mathbf{H}(\rho)})$$
(6.17)

where $subcorr(\mathbf{A}, \mathbf{B})$ refers to the largest correlation between the subspaces spanned by the columns of \mathbf{A} and \mathbf{B} . Φ_s contains the q eigenvectors corresponding to the largest eigenvalues, $\mathbf{U}_{\mathbf{H}(\rho)}$ contains the left singular vectors of $\mathbf{H}(\rho)$, and $\lambda_{max}(.)$ is the maximum eigenvalue of the enclosed expression.

Identification of the remaining local maxima becomes more difficult since MUSIC scanning may miss shallow or adjacent peaks and provide solutions that are restricted to dominant peaks. In RAP-MUSIC the component of the signal subspace that is spanned by the first source is removed and then another search is performed to find the next source over this modified subspace. The modified subspace is obtained by

applying the orthogonal projector to the gain vector and signal subspace [78]. The second source is then found as the global maximizer:

$$\rho_2 = \arg\max_{\rho} \ subcorr(\Pi_{\alpha(\rho_1)}^{\perp} \mathbf{H}(\rho), \Pi_{\alpha(\rho_1)}^{\perp} \mathbf{\Phi}_s)$$
 (6.18)

where $\Pi^{\perp}_{m{lpha}(m{
ho}_1)}$ is the orthogonal projector to the gain vector $m{lpha}(m{
ho}_1)$.

The BF approach localizes the source based on minimizing the output power of the filter while passing activity from a location of interest. The location of interest is scanned on all of the grid cells to produce a metric of source activity. Let $\mathbf{W}(\rho)$ denote the beamspace spatial linear filter weights for location ρ . The spatial filter is obtained by solving:

$$\min E\{|\mathbf{W}(\boldsymbol{\rho})\mathbf{y}|^2\} \quad subject \ to \ \mathbf{W}(\boldsymbol{\rho})\mathbf{H}(\boldsymbol{\rho}) = \mathbf{I}$$
 (6.19)

By using Lagrange multipliers the above constrained problem is solved and the solution is then normalized and divided by the power of the corresponding noise spatial spectrum in the absence of the signal [92]:

$$P_n(\boldsymbol{\rho}) = \frac{tr\{\mathbf{H}^T(\boldsymbol{\rho})\mathbf{C}_y^{-1}\mathbf{H}(\boldsymbol{\rho})\}}{tr\{\mathbf{H}^T(\boldsymbol{\rho})\mathbf{C}_n^{-1}\mathbf{H}(\boldsymbol{\rho})\}}$$
(6.20)

where C_y is an estimate of the measured signal covariance and C_n is an estimate of the noise-only covariance. C_n may be estimated from data that is known to be noise only, such as pre-stimulus data in an ERP experiment. In the following section the noise is assumed to be GWN and temporally and spatially uncorrelated (i.e. $C_n = I$). The localization of sources is then performed by finding ρ that maximizes (6.20).

6.3.2 Comparison Studies

Various computer simulations were conducted to show the performances of the methods under different assumptions. A three-shell spherical head model is employed. The conductivity ratio used for forward solution computation was 1, 0.0125, and 1 for scalp, skull and brain respectively. The values of estimators were scanned on a discrete cubic grid with more than 6510 grid cells and an inter-grid distance of 5mm. There were 25 electrodes placed on the scalp using the standard 10-20 system [84]. Without loss of generality a larger number of electrodes can be selected to improve the performance of the method while the computational complexity increases only slightly. These signals were sampled every 4ms, thus obtaining 250 samples for each second in the computer simulation.

The localization error, which is defined as the three-dimensional geometrical distance between the estimated and simulated locations, is used as the major criterion for the assessment of the methods. The results were obtained by averaging over 100 Monte Carlo trials for each noise level. The available noise power is measured by SNR in dB units which is defined as

$$SNR = 10\log(\frac{P_{signal}}{P_{noise}}) \tag{6.21}$$

where P_{signal} and P_{noise} denote respectively the powers of signal and noise. In the RBPF and B-RBPF approaches, the noise covariance matrices \mathbf{Q}_w^{ζ} and \mathbf{Q}_v^{ζ} (ζ denotes location ρ or moment m) are simply assumed to be in the forms of $\sigma_w^{\zeta}\mathbf{I}$ and $\sigma_v^{\zeta}\mathbf{I}$. Different values of σ_w^{ζ} and σ_v^{ζ} were empirically used to obtain the best results. The σ_w^{ζ} and σ_v^{ζ} parameters determine the performance of the estimators by a trade-off between

the estimators' sensitivity and stability or by a trade off between noise suppression and signal tracking. The number of particles N was set to 3000 during all experiments. The length of the Hamming window M was set to 25 during the B-RBPF run. In practice, M should be chosen according to the data as long as it is stationary or at least if the location of the dipole remains the same.

Fig. 6.1 shows the locations of six different dipoles used for the following simulation studies. They are located in different parts of the brain to better assess the performance of the methods. S1 and S2 are in superficial (cortical) regions, from which most elements of scalp-recorded E/MEG are generated. S3 and S4 are in the temporal lobe in the regions of left- and right-auditory cortices. S5 and S6 are deep sources located near the thalamus.

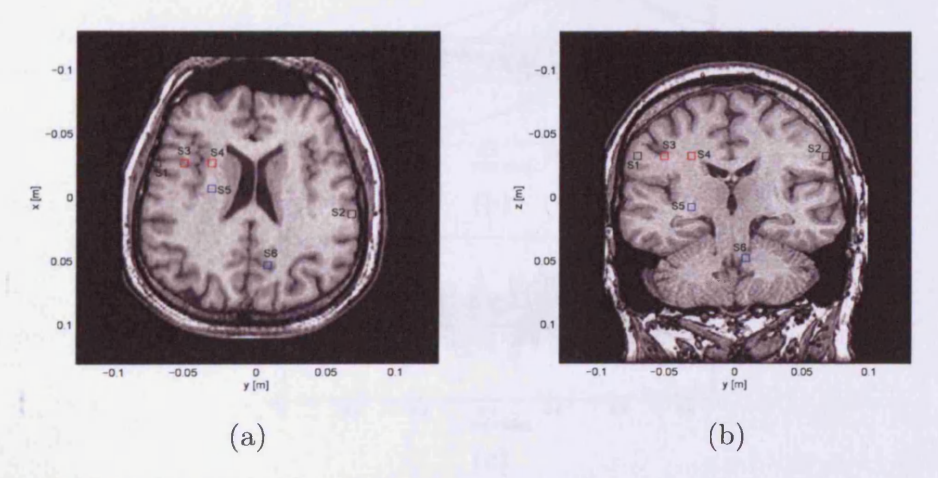


Figure 6.1: Dipole locations used in simulation studies for (a) locations in axial view, and (b) the same locations in coronal view.

The moments of dipoles used for simulations were assumed to be constant, sinusoidal and Gaussian functions of time. An example of moments, noiseless and noisy simulated E/MEG is shown in Fig. 6.2. The length of the signals was assumed to be

0.65s. The frequency of the sine wave was set to 1.54Hz and the mean and standard deviation of the Gaussian wave were set to 0.37s and 0.13s, respectively. GWN was added to the moments and to the simulated E/MEG after multiplying the forward matrix by the moments. The values of SNR were controlled only by the power of the GWN that was added to the simulated E/MEG. The same functions and procedures were used for all other simulations that are described below.

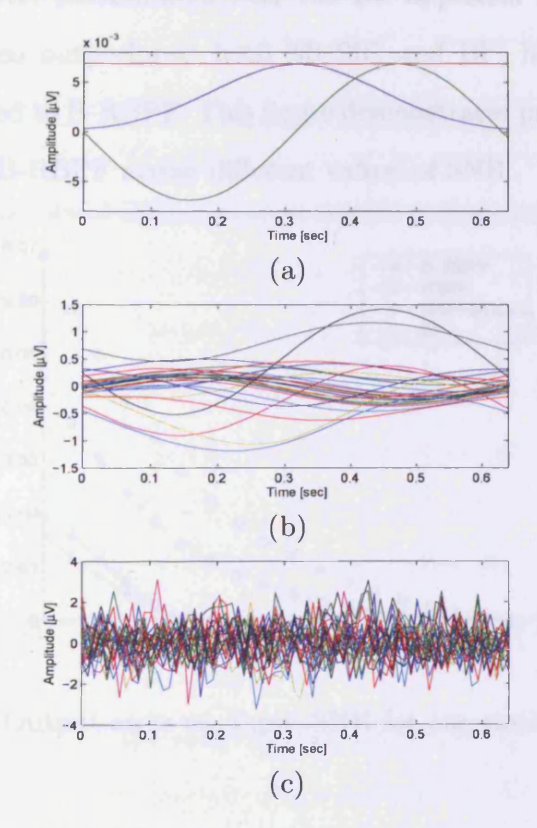


Figure 6.2: Examples of simulated data: (a) noiseless moments in x, y and z directions, (b) simulated noiseless E/MEG for 25 electrodes, and (c) simulated noisy E/MEG with SNR=-5dB. The GWN was added to the moments and the signals obtained after applying the forward matrix.

Effects of SNR

In this simulation, one stationary dipole located in a superficial region of the brain is considered. The location of the dipole is S1 in Fig. 6.1, where axial and coronal views are provided. The errors of the estimated dipole locations for different SNR values are shown in Fig. 6.3. For such a single dipole system, the MUSIC algorithm has considerably better performance over the BF approach for different values of SNR. The RBPF also outperforms both MUSIC and BF, however, it has poorer performance compared to B-RBPF. This figure demonstrates promising performances for both RBPF and B-RBPF across different values of SNR.

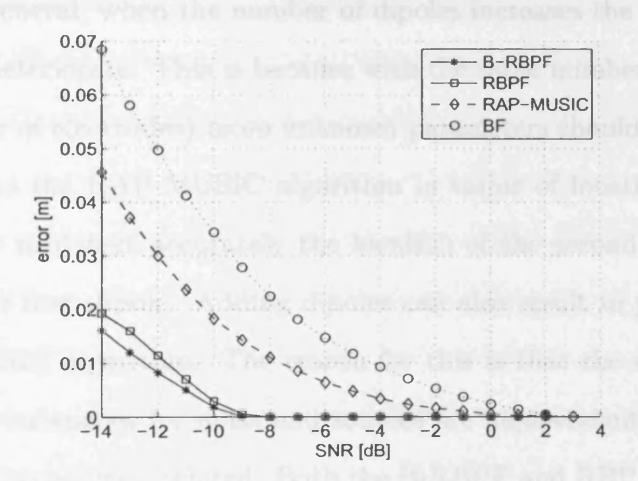


Figure 6.3: Output error vs. input SNR for one stationary dipole.

Effects of Dipole Location

In the next simulation, two spatially stationary dipoles were used to simulate the data. The moments of the first dipole were sinusoidal, constant, and Gaussian functions of time in x, y and z directions, respectively, and the moments of the second

dipole were constant, Gaussian, and sinusoidal functions of time in the x, y, and z directions, respectively. These two sources can be considered as partially temporally correlated sources (the mean correlation coefficient over each direction is 0.0423). To investigate the effect of dipole location on the performance of the methods three examples are considered; first, for two superficial dipoles with a large distance between them, second, for two close superficial dipoles, and third, for two deep sources.

The locations of the two superficial sources at a reasonable distance from each other are S1 and S2 shown in Fig. 6.1. The estimation error for the first dipole is depicted in Fig. 6.4(a) and the estimation error for the second dipole is shown in Fig. 6.4(b). In general, when the number of dipoles increases the performances of all the algorithms deteriorate. This is because with the same number of known parameters (the number of electrodes) more unknown parameters should be estimated. The BF is superior to the RAP-MUSIC algorithm in terms of locating the first dipole. However, it fails to detect accurately the location of the second dipole and gives a location near the first dipole. Adding dipoles can also result in poorer performance of the RAP-MUSIC algorithm. The reason for this is that the method assumes all of the projected subspaces for noise and sources are independent, which means that the sources need to be uncorrelated. Both the B-RBPF and RBPF outperformed the RAP-MUSIC and BF algorithms and they were successful at detecting both sources accurately.

Fig. 6.5 shows the performances of the methods for the two simulated closely spaced sources. The locations of sources are S3 and S4 as depicted in Fig. 7.1 in axial and coronal views. Fig. 6.5(a) shows the localization error versus SNR for the first dipole (S3). RAP-MUSIC has better performance than the BF approach for the first

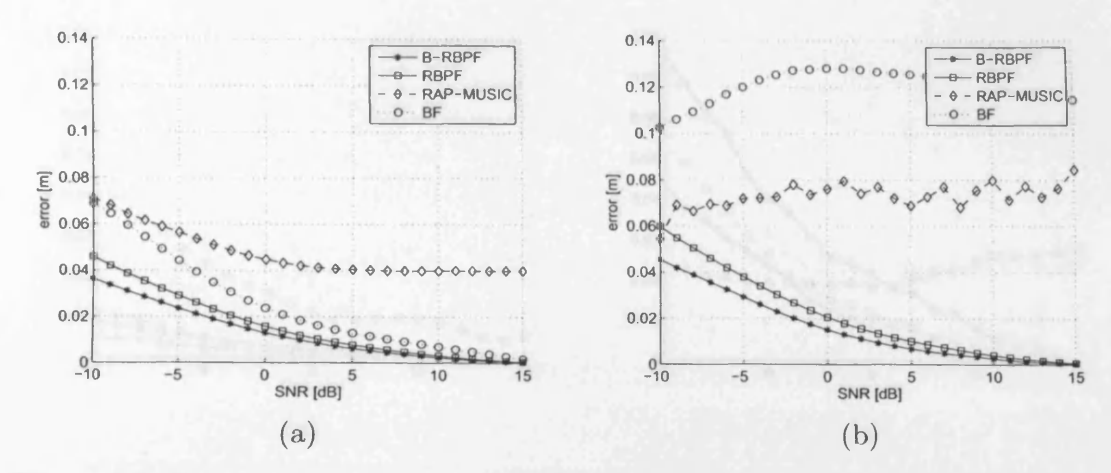


Figure 6.4: Output SNR vs. input SNR for two distal sources for (a) the first source (S1) and (b) the second source (S2).

source. The RBPF outperforms RAP-MUSIC and BF, however it remains inferior to the B-RBPF algorithm, independent of which SNR value is employed. RBPF and B-RBPF have acceptable performances even in SNRs as low as -5dB. Fig. 6.5(b) displays the localization error for the second dipole (S4). RAP-MUSIC locates the second source between the two original source locations and shows approximately constant error. The correlation between the sources has less impact on localization using the BF method compared to the RAP-MUSIC approach and it shows a roughly monotonic increasing error as SNR decreases. Although the RBPF localizes the first source precisely, its performance is poorer than those of the other methods for the second dipole. This occurs because close sources have similar gain matrices and the RBPF approach localizes the sources simultaneously, so it localizes one of the dipoles and localizes another source with a different gain matrix. B-RBPF, however, still has superior performance in comparison to the other methods.

The next simulation uses one source in the middle of the brain and one deep

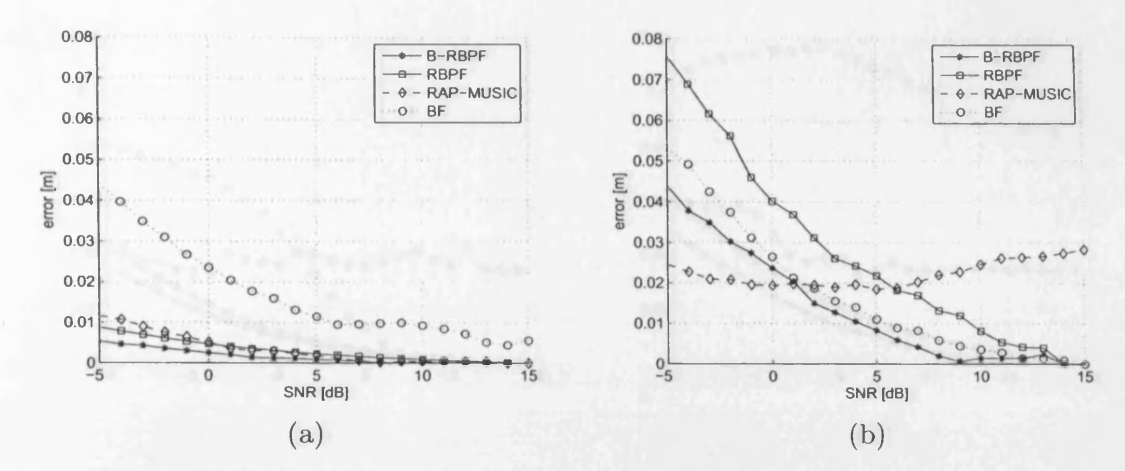


Figure 6.5: Output error vs. input SNR for two proximal sources for (a) the first source (S3), and (b) the second source (S4).

source (locations S5 and S6 in Fig. 6.1). The results are shown in Fig. 6.6 for both sources. The BF performance deteriorates markedly for deep sources and is likely to localize the sources in superficial locations. This comes about because, by dividing the output power of BF to the corresponding noise power only, the power of deep sources (which have smaller gain matrix power $tr\{\mathbf{H}^T(\rho)\mathbf{H}(\rho)\}$) is attenuated more than the power of superficial sources. RAP-MUSIC is a subspace method and only uses the eigenvectors and consequently has no sensitivity to the gain matrix power (i.e. deep sources). Both RBPF and B-RBPF have robust results in the case of deep sources and better performance than the other methods. B-RBPF again outperforms all other methods regardless of the dipole locations.

Effects of Correlations Between Sources

To investigate the effects of correlations between sources, two sources with locations S1 and S2 in Fig. 6.1 are considered. The moment of the first source in all directions

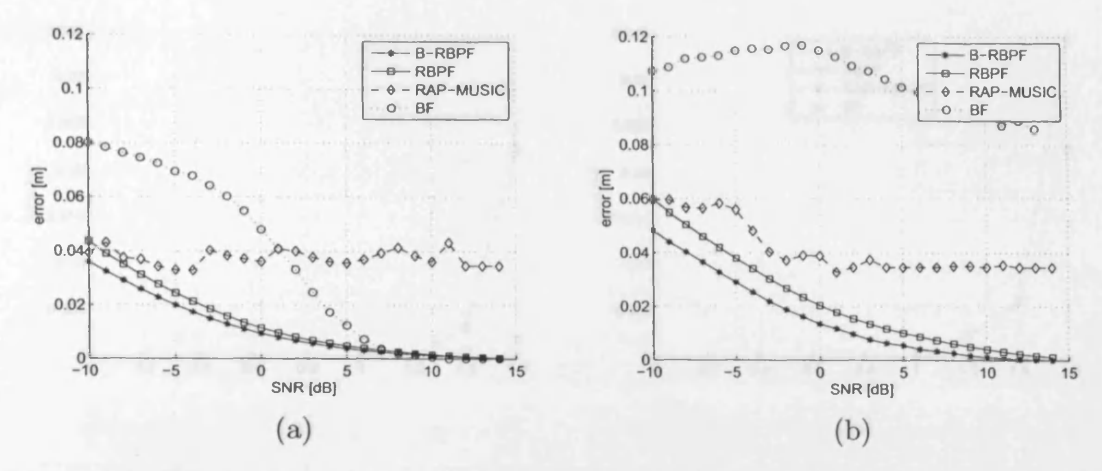


Figure 6.6: Output error vs. input SNR for two deep sources for (a) the first source (S5) and (b) the second source (S6).

is assumed to be a sine signal as $\sin(2\pi t)$ and the moment of the second dipole in all directions is assumed to be a cosine signal as $\cos(2\pi t + \alpha)$, where α is a parameter which indicates the correlation between the sources. When $\alpha = 0$ the sources are completely uncorrelated and when $\alpha = \frac{\pi}{2}$ the sources are strongly correlated. SNR was fixed at 15dB to investigate only the effect of correlation between the sources. The output error for different values of α has been shown in Fig. 6.7. This example shows that BF has moderate sensitivity to the correlation between sources and RAP-MUSIC is more sensitive than the other approaches to the correlation between the sources. Fig. 6.7 also indicates that RBPF and B-RBPF have no sensitivity to correlations between the sources, and they can find the sources using only gain matrices (i.e. locations) regardless of their moments.

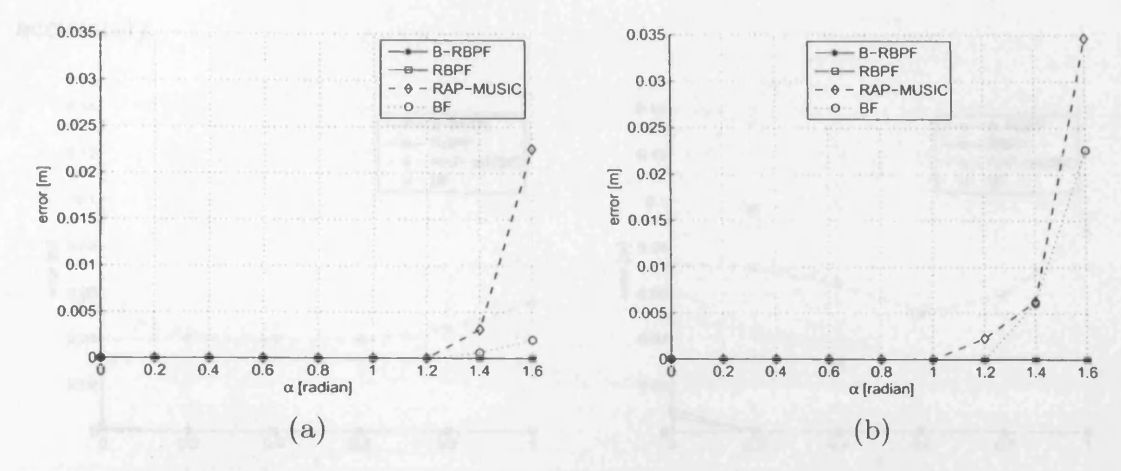


Figure 6.7: Effect of correlation between sources on the output location error for (a) the first source, and (b) the second source.

Effects of Colored Noise

There are different ways of generating colored noise and they may have different effects on the performance of the algorithms. For the current study, a similar model of the noise to that used in [2] was employed. The noise is zero mean additive colored Gaussian noise with covariance matrix \mathbf{Q}_v^{ρ} whose element at its *i*th row and *j*th column is given by $\mathbf{Q}_v^{\rho}(i,j) = \eta^2 r^{|i-j|/2}$, where η and r are the variance of total noise per sensor and the spatial covariance factor of noise, respectively.

Two sources at locations S1 and S2 as shown in Fig. 6.1 with SNR = 15 are considered. Fig. 6.8 displays the localization error as a function of the noise spatial covariance factor r while $\eta=1$. RAP-MUSIC and RBPF as well as B-RBPF assume that the noise is additive and GWN, and as Fig. 6.8 shows only the RAP-MUSIC approach is sensitive to the spatially colored noise and theoretically requires a perfect knowledge of the noise covariance [99]. The other algorithms are insensitive to Gaussian spatial colored noise regardless of its color and they all localized the sources

accurately.

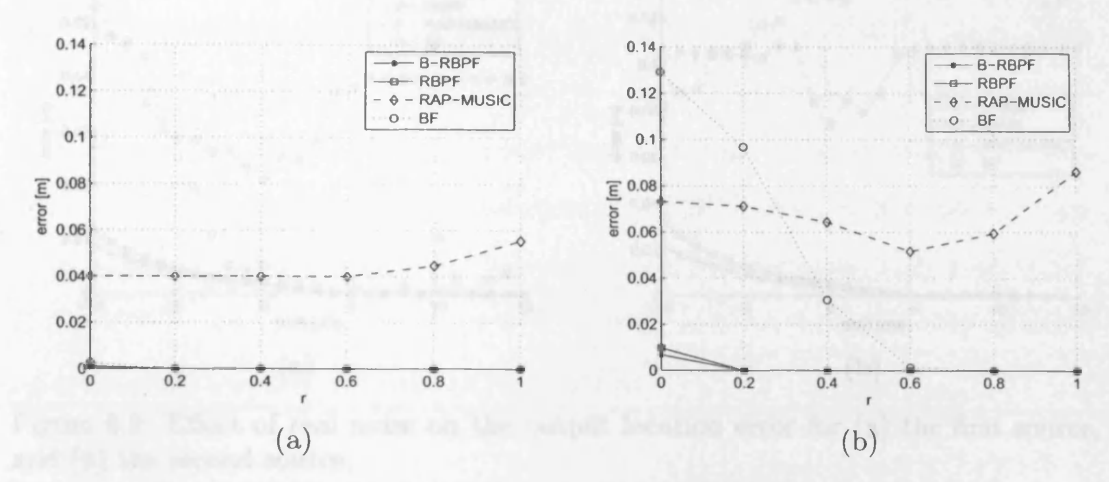


Figure 6.8: Effect of colored noise on the output location error for (a) the first source, and (b) the second source.

Effects of Real Noise

The behavior of the algorithms in the presence of additive non-Gaussian noise was studied. For this purpose, background E/MEG signals were added to the simulated data. The results as a function of SBR are displayed in Fig. 6.9. The SBR is defined as the ratio of the power of the simulated data to the power of the added background E/MEG in dB units. Similar to spatially colored noise, RAP-MUSIC is more sensitive to the real noise than other algorithms. Both RBPF and B-RBPF have better performance across different values of SBR than those of for SNRs, while the B-RBPF is superior to the RBPF.

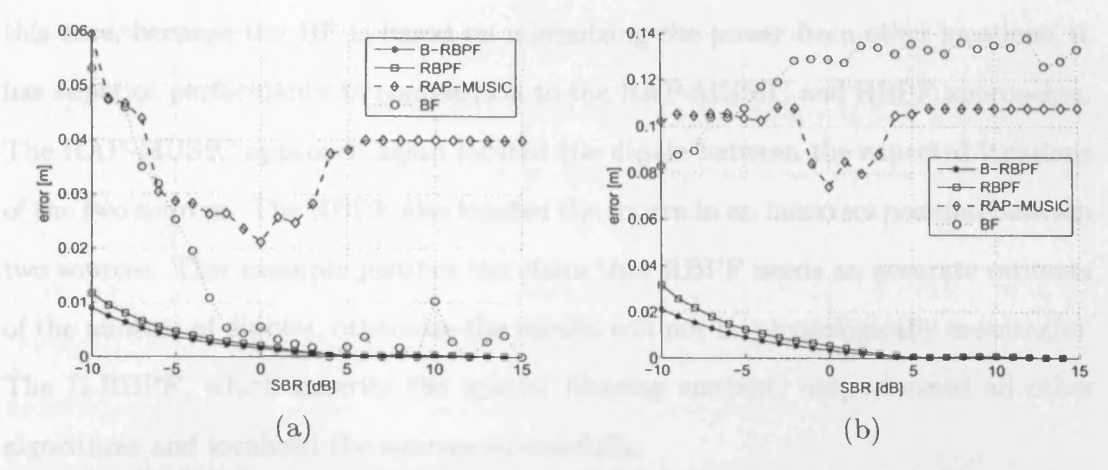


Figure 6.9: Effect of real noise on the output location error for (a) the first source, and (b) the second source.

Effect of Assumptions About the Number of Dipoles q

Assumptions about the number of sources have no impact on the performance of the RAP-MUSIC and BF approaches, since they localize the sources sequentially. These assumptions can, however, have a major effect on the performance of the RBPF. The RBPF finds sources by maximizing the likelihood and finding the location of the source which produces results that are most similar to the observation. Therefore, to localize the activity originating from two sources using only one source, it is likely to identify a location between the two original sources that can maximize the likelihood to a greater degree than one of the original sources. To explain this phenomenon further, consider the data obtained by the mixture of two dipoles located in S1 and S2 in Fig. 6.1. All approaches are employed to localize the two dipoles by assuming the number of dipoles was one. The output error for different SNRs is shown in Fig. 6.10. The output error is defined as the three dimensional geometrical distance between the estimated dipole location and the simulated strongest dipole location. In

this case, because the BF is based on minimizing the power from other locations, it has superior performance in comparison to the RAP-MUSIC and RBPF approaches. The RAP-MUSIC approach again located the dipole between the expected locations of the two sources. The RBPF also located the source in an incorrect position between two sources. This example justifies the claim that RBPF needs an accurate estimate of the number of dipoles, otherwise the results will not be physiologically meaningful. The B-RBPF, which inherits the spatial filtering concept, outperformed all other algorithms and localized the sources successfully.

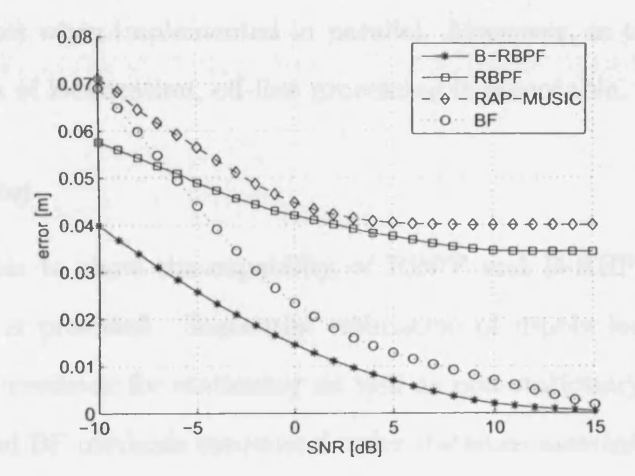


Figure 6.10: Output location error vs. SNR for two simulated sources. In this example it is assumed that only one source is generating the data.

Execution Time

The single run execution times for BF, RAP-MUSIC, RBPF and B-RBPF were 0.052, 0.065, 67.115 and 96.782 sec, respectively. Simulations were performed on a 2.4-GHz Intel Pentium IV processor using MATLAB software. As expected, the execution times for RBPF and B-RBPF are considerably longer than the execution time for the other algorithms. The execution time is related to the number of particles and number of grid cells. These times indicate those obtained on a serial computer and a marked reduction in computation times can be expected for the RBPF and B-RBPF approaches when implemented in parallel. Moreover, in the vast majority of implementations of localization, off-line processing is acceptable.

Dipole Tracking

Here, an example to show the capability of RBPF and B-RBPF for tracking two moving dipoles is provided. Sequential estimation of dipole locations enables use of the proposed methods for stationary as well as non-stationary signals. Since the RAP-MUSIC and BF methods use second order statistics associated with the signals, they cannot be applied to the estimation of time-varying dipole locations.

In this simulation, two moving dipoles (the first one located in the right and the second in the left hemisphere) are considered. The SNR was set to 5dB. The initial states of the filters were set to zero for the moments and set to the center of the brain space for locations. The original and estimated locations are shown in Fig. 6.11. The original tracking of the movements is displayed by black solid lines and the estimated locations using RBPF and B-RBPF are shown by the blue and red lines, respectively. The methods located the dipoles with a time delay, which is related to the covariance

Table 6.1: Errors of two moving dipoles' locations and moments using the RBPF and B-RBPF methods. The error of locations and moments are in meter and μV units, respectively.

	first location	second location	first moment	second moment
RBPF	0.0303	0.0273	0.0028	0.0023
B-RBPF	0.0138	0.0192	0.0017	0.0026

matrices of the noise (i.e. proportional to the σ_w^ρ and σ_v^ρ parameters). Therefore, the first segments of movement tracking before the convergence of the filters (before 0.01 sec) are eliminated. In these highly noisy signals, both RBPF and B-RBPF detect and track dipole locations with an acceptable degree of accuracy. The original (solid lines), noisy (dotted lines) and estimated moments using RBPF (blue lines) and B-RBPF (red lines) are shown in Fig. 6.12 for two dipoles in x, y and z directions. Both methods, and especially RBPF, have some inconsistency in moment estimation before 0.01 sec, due to the convergence of the filters in this period. In general, B-RBPF has slightly better performance over all others. Finally, in order to better highlight the differences between performances for the RBPF and the B-RBPF approaches, the mean errors over all time samples for the locations and moments are presented in Table 6.1. Except for the second dipole moments, the B-RBPF outperforms the RBPF. This example demonstrates the use of RBPF and especially B-RBPF in dipole tracking in practical applications.

6.4 Conclusions

In this chapter, an E/MEG dipole source localization method based on RBPF and BF was presented. The LCMV-BF was reformulated to be used jointly with RBPF.

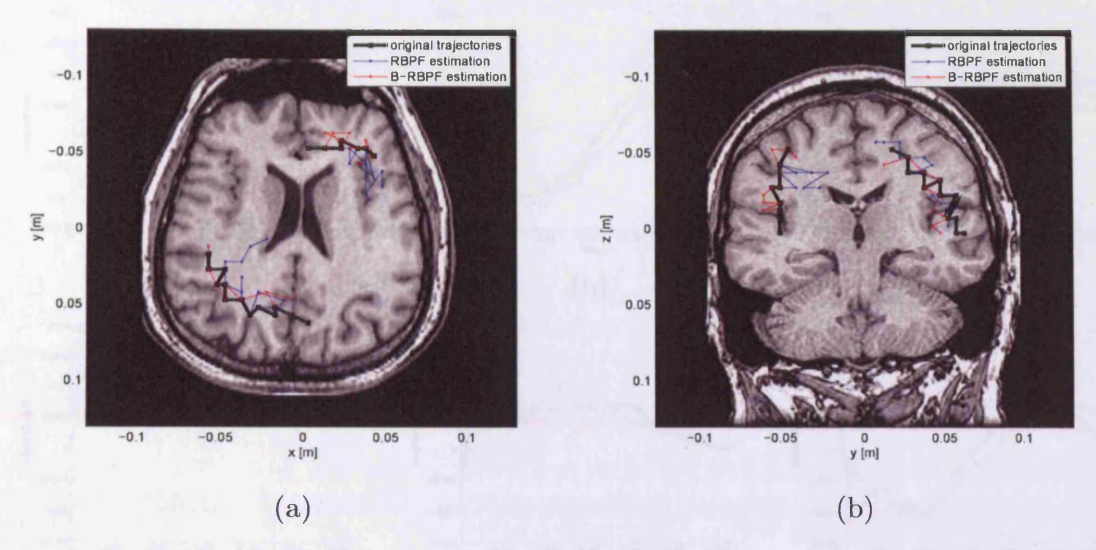


Figure 6.11: Original and estimated dipole trajectories using the RBPF and B-RBPF methods in (a) axial view and (b) coronal view.

The results were compared with those obtained using RBPF, RAP-MUSIC and BF approaches, and they are discussed below.

RAP-MUSIC is a method that is robust in the face of GWN. It is, however, very sensitive to other kinds of noise, including Gaussian colored noise and real E/MEG background noise. The approach also needs an accurate estimation of the covariance matrix of the data. RAP-MUSIC is also more sensitive than the other approaches to the correlation between sources.

BF is a powerful source localization method in a number of different situations. In the simulation studies, BF showed consistency to different kinds of noise and was robust with respect to the number of dipoles that were used in the simulations. BF also has the ability to operate in distributed or tomographic source localization methods. Its limitations compared to the other algorithms are: (i) sensitivity to the power of noise, (ii) moderate sensitivity to correlations between sources, and (iii) its

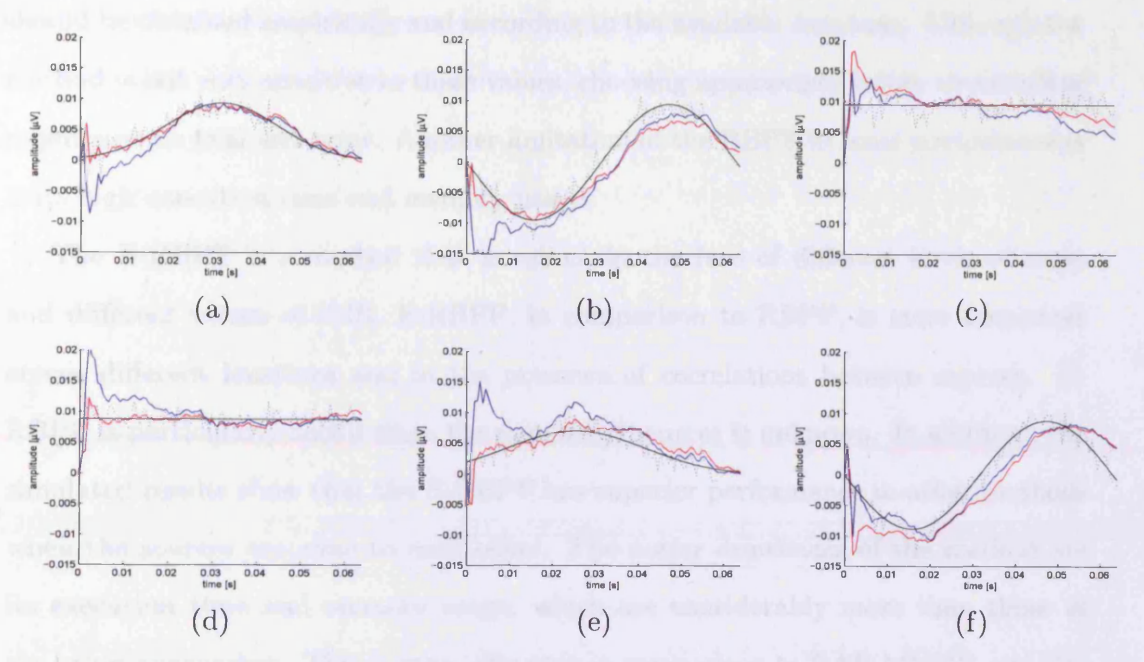


Figure 6.12: Original and estimated moments using RBPF and B-RBPF: (a) moment of the first dipole in x direction, (b) moment of the first dipole in y direction, (c) moment of the first dipole in z direction, (d) moment of the second dipole in x direction, (e) moment of the second dipole in y direction, and (f) moment of the second dipole in z direction.

failure to detect deep sources in noisy data.

RBPF shows robustness to noise power and is suitable when different kinds of noise such as spatially colored noise and real E/MEG background noise. RBPF performed consistently for superficial as well as deep sources and had superb performance when the sources were correlated. Unlike BF and RAP-MUSIC, the RBPF is capable of dipole tracking and can be applied to stationary as well as non-stationary data. The major drawbacks of the RBPF are its sensitivity to the assumed number of dipoles and its poor performance when the sources are close to each other. In addition, choosing appropriate noise covariance matrices for the state and measurement equations for both location and moments is crucial for the approach. The noise covariance matrices

should be obtained empirically and according to the available database. Although the method is not very sensitive to these values, choosing appropriate values nevertheless requires some trial and error. Another limitation of the RBPF in some circumstances is its high execution time and memory usage.

The B-RBPF is a method that is robust in the face of different kinds of noise and different values of SNR. B-RBPF, in comparison to RBPF, is more consistent across different locations and in the presence of correlations between sources. B-RBPF is particularly useful when the number of sources is unknown. In addition, the simulated results show that the B-RBPF has superior performance to other methods when the sources are close to each other. The major drawbacks of the method are its execution time and memory usage, which are considerably more than those of the other approaches. This is especially true in comparison to RAP-MUSIC and BF. Furthermore, for B-RBPF, along with choosing appropriate noise covariance matrices, we need to choose a proper window length M. The data in this window should be stationary to have a true estimation for the covariance matrix of the data. For real E/MEG data in many cases it can be assumed that the data around a short window is stationary, since the brain state does not change substantially over short periods. Note, moreover, that this assumption is much weaker than that required by the BF and RAP-MUSIC approaches, which need the signal to be stationary over the whole data length.

In conclusion, these observations demonstrate significant potential for the deployment of the B-RBPF approach for source localization of real-time measures of neural activity that are recorded at the scalp. In subsequent work we will extend the assessments and comparisons across the methods described here to real data obtained in paradigms where the likely sources of scalp-recorded real-time measures of neural activity (both EEG and MEG signals) are well-known. Moving on from these assessments based upon real data, satisfactory endpoints for the development of these approaches would include (but certainly not restricted to) their use in applications such as brain computer interfacing (BCI), localizing seizure activities, and characterizing neural dysfunction associated with conditions such as dementia and schizophrenia.

Appendix

A Derivation of Solution for Equation (6.15)

The first part of equation (6.15) can be written in a matrix form as $\mathbf{W}^T \underline{\mathbf{H}} = \underline{\mathbf{H}}$ and the second part can be satisfied by minimizing the output power of the filter, so the following optimization problem is obtained:

$$\min_{\mathbf{W}^T} E\{|\mathbf{W}^T \mathbf{y}|^2\} \text{ subject to} : \mathbf{W}^T \underline{\mathbf{H}} = \underline{\mathbf{H}}$$
 (A1)

A closed-form solution to the above constrained problem can be given as follows. Using the method of Lagrange multipliers, the following unconstrained problem is resulted:

$$\min_{\mathbf{W}^T} f = tr\{\mathbf{W}^T \mathbf{y} \mathbf{y}^T \mathbf{W} + (\mathbf{W}^T \underline{\mathbf{H}} - \underline{\mathbf{H}}) \mathbf{\Gamma}\}$$
 (A2)

The minimum can be found by finding zero of the gradient equation $\frac{\partial f}{\partial \mathbf{w}} = \mathbf{0}$, therefore:

$$\frac{\partial f}{\partial \mathbf{W}} = 2\mathbf{W}^T \mathbf{y} \mathbf{y}^T + \mathbf{\Gamma}^T \underline{\mathbf{H}}^T = \mathbf{0}$$
(A3)

which means:

$$\mathbf{W}^T = -\frac{1}{2} \mathbf{\Gamma}^T \underline{\mathbf{H}}^T \mathbf{C}_y^{-1} \tag{A4}$$

Substituting \mathbf{W}^T from (A4) into the right-hand side of equation (A1) and after some algebra:

$$\Gamma = -2\underline{\mathbf{H}} \left(\underline{\mathbf{H}}^T \mathbf{C}_y^{-1} \underline{\mathbf{H}} \right)^{-1}$$
 (A5)

using equations (A4) and (A5), W^T is obtained as:

$$\mathbf{W}^{T} = \underline{\mathbf{H}} \left[\underline{\mathbf{H}}^{T} \mathbf{C}_{y}^{-1} \underline{\mathbf{H}} \right]^{-1} \underline{\mathbf{H}}^{T} \mathbf{C}_{y}^{-1}. \tag{A6}$$

which is equivalent to equation (6.16).

Chapter 7

Variational Bayes for

Spatiotemporal Identification of

ERP Subcomponents

7.1 Introduction

In the previous chapters, a method for single trial estimation and dipole source localization was proposed. Here, the principal interest is in developing a spatiotemporal method to reliably both localize and estimate the single trial variability of ERP subcomponent parameters during the course of a recording session. In other words, a novel method for tracking of ERP subcomponent parameters including location, amplitude, latency and width is proposed. In this approach, the location of dipoles can vary from trial to trial in a realistic head model. ERPs are assumed to be the superposition of a number of ECDs whereas their temporal bases are modeled by Gaussian

waves. The amplitudes, means, and variances of the Gaussian waves can be interpreted as the amplitudes, latencies, and widths of ERP subcomponents, respectively. Variational Bayes shows that when the prior distribution is unknown, maximizing the likelihood of each parameter (via separate estimation of each parameter) is equivalent to minimizing the Kullback-Liebler distance between the estimated and the true posterior distributions [100].

The locations are estimated using PF. Many studies have shown that PF is one of the best methods when the relation between the desired parameter (states) and the measurement is nonlinear [29]. A closed-form solution for the amplitude is also given using the ML approach. The solutions to the latency and width are given recursively by the Newton-Raphson technique which has a rapid convergence. One challenge for this approach is that a very low SNR on some trials can result in the divergence of filtering for the estimation of amplitudes, latencies, and widths of Gaussian functions. To compensate for this failure and obtain a robust solution recursive methods are introduced, which guarantee the stability of the filtering from trial to trial.

The rest of the chapter is organized as follows. In Section 7.2.1, the spatio-temporal ERP modeling is presented. Section 7.2.2 contains a new approach based on variational Bayes for estimation of the ERP model parameters. PF, ML and Newton-Raphson methods to estimate the ECD locations and parameters are also given in Section 7.2.2. Simulations for tracking of the ERP subcomponents are provided in Section 7.3.1 and the effectiveness of the method in a simple oddball paradigm is demonstrated in Section 7.3.2. Finally, a detailed discussion of the proposed method is presented.

7.2 Methods

7.2.1 Problem Formulation

Let the measured ERP data $\mathbf{Y}_k \in \mathbb{R}^{L \times M}$ be a matrix composed of the potentials acquired from L electrodes and M time samples at the kth trial. Also, suppose that the ERP is generated from q ECDs whose three dimensional locations are specified by $\{\rho_{k,i}; i=1,\ldots,q\}$. The potential at the scalp \mathbf{Y}_k is assumed to be the superposition of the potentials from q dipoles. Based on these assumptions, it may be written

$$Y_{k} = \sum_{i=1}^{q} H(\rho_{k,i}) a_{k,i} \psi_{k,i} + N_{k}$$
 (7.1)

where $\mathbf{H} \in \mathbb{R}^{L \times 3}$ is the forward matrix and is a nonlinear function of the ECD location. \mathbf{N}_k represents additive Gaussian zero mean noise with unknown positive definite spatial covariance \mathbf{Q}_k and known temporal covariance matrix \mathbf{I} which is an identity matrix. Hence, the covariance matrix of the noise can be written as $\mathbf{I} \otimes \mathbf{Q}_k$, where \otimes represents the Kronecker product. Noise is assumed to be independent of the source activities and identically distributed across time (temporally), but not necessarily across the sensors (spatially). These assumptions provide a quick and simple estimation of the noise covariance matrix from trial to trial. In equation (7.1), $\mathbf{a}_{k,i} \in \mathbb{R}^{3\times 1}$ is the amplitude of the ECD moment in x, y and z directions and $\psi_{k,i} = [\psi_{k,i}(1) \dots \psi_{k,i}(M)] \in \mathbb{R}^{1\times M}$ represents the temporal basis of the ith ECD moment. Each $\psi_{k,i}(t)$ is given by a Gaussian wave as:

$$\psi_{k,i}(t) = \frac{1}{\sigma_{k,i}\sqrt{2\pi}} \exp(-\frac{(t-\mu_{k,i})^2}{2\sigma_{k,i}^2})$$
 (7.2)

Note that the dipole amplitudes are different in x, y and z directions, but have the same temporal bases in all three directions (i.e. same $\sigma_{k,i}$ and $\mu_{k,i}$ in three directions). For simplicity, and without loss of generality, the normalizing factor $\frac{1}{\sigma_{k,i}\sqrt{2\pi}}$ is ignored and it is assumed that it has been embedded in the amplitude vector $\mathbf{a}_{k,i}$. Modeling the temporal bases of ERP subcomponents using parametric functions has been exploited in many studies (e.g. see [97, 27]) and across them the Gaussian waveform modeling is the most common approach [103]. Although real ERP subcomponents do not have the exact shape of Gaussian waveforms, this modeling allows a robust and quick estimation of the peak parameters (latency and amplitude) with which neurophysiologists and cognitive scientists are primarily concerned.

The primary aim is to recursively estimate the model parameters $\theta_{k,i} = \{\rho_{k,i}, a_{k,i}, Q_k, \mu_{k,i}, \sigma_{k,i}\}$ based on their previous estimations $\hat{\theta}_{k-1,i}$ and the available measurements \mathbf{Y}_k . Therefore, the evolution of the model parameters $\theta_{k,i}$ is assumed to be a Marokovian process and does not vary extensively across trials. This assumption has been exploited in many ERP analyses (e.g. [51, 102, 34, 62]). It can be explicitly justified by Mocks et al. observation [73] that consecutive responses to repeated stimuli vary slowly since brain states change gradually over time in this context, although responses throughout the experiment can differ significantly. This assumption, however, may limit the deployment of the method in some applications where there is extensive electrophysiological variability from trial to trial. In this case, as it will be shown in the simulation results section, the method may at least reveal some trend of parameters changing during the course of a recording session. For instance, it can observed whether ERP parameters increase or decrease with time on task.

7.2.2 Parameter Estimation by Variational Bayes

Instead of estimating θ , the posteriori distribution $p(\theta|\mathbf{Y})$, which fully describes the knowledge regarding the model parameters θ^1 , is estimated. Estimation of the posteriori distribution is the central quantity of interest in Bayesian estimation and is typically expanded using Bayes rule as:

$$p(\theta|\mathbf{Y}) \propto p(\mathbf{Y}|\theta)p(\theta)$$
 (7.3)

where the dependence upon the model is implicitly assumed. $p(\mathbf{Y}|\boldsymbol{\theta})$ is calculated from the model and $p(\boldsymbol{\theta})$ incorporates prior knowledge of the parameter values and their variabilities. In nonlinear models, however, the posteriori distribution is often difficult to analytically estimate using equation (7.3). In this case, it might be approximated in a simpler form $r(\boldsymbol{\theta})$, which can be determined using the variational method.

A criterion to determine the goodness of fit of $r(\theta)$ to the true posterior distribution $p(\theta)$ is given via free energy which defined as [100]:

$$F = \int_{all \ \theta} r(\theta) \log \left[\frac{p(\mathbf{Y}, \theta)p(\theta)}{r(\theta)} \right] d\theta$$
 (7.4)

Derivation of the posterior distribution $p(\theta|\mathbf{Y})$ depends on correct estimation of $r(\theta)$, which is achieved by maximizing the free energy over $r(\theta)$. By such maximization, the best approximation to the true posterior is found. This also establishes the tightest lower bound on the true marginal likelihood. Moreover, the maximization of F is equivalent to minimizing the Kullback-Liebler distance between $r(\theta)$ and the true

¹For the sake of convenience in this section the variable indices are omitted.

posterior [100].

In variational Bayes, it is also assumed that [100]

$$r(\boldsymbol{\theta}) = \prod_{i} r(\boldsymbol{\theta}_i) \tag{7.5}$$

where the parameters in θ have been factorized into different independent groups θ_i , each with their own approximate posterior distribution $r(\theta_i)$. This is the key restriction in the variational Bayes method. The groupings are performed logically according to their appearance in the model. For example, in the proposed model the locations are grouped in one group and the latencies and the widths in another group. Using calculus of variations, $r(\theta_i)$ is obtained by maximization of (7.4) as

$$\log r(\boldsymbol{\theta}_i) \propto \int_{all \; \boldsymbol{\theta}_{/i}} r(\boldsymbol{\theta}_{/i}) \log \left[p(\mathbf{Y}|\boldsymbol{\theta}) p(\boldsymbol{\theta}) \right] d\boldsymbol{\theta}_{/i}$$
 (7.6)

where $\theta_{/i}$ refer to all the parameters except the *i*th group. If the prior is assumed to be known, equation (7.6) implies MAP estimation: $r(\theta_i)$ is the likelihood function:

$$r(\boldsymbol{\theta}_i) \propto p(\boldsymbol{\theta}_i)p(\mathbf{Y}|\boldsymbol{\theta}_i)$$
 (7.7)

If the prior is assumed to be unknown, equation (7.6) implies that $r(\theta_i)$ is the likelihood function:

$$r(\theta_i) \propto p(\mathbf{Y}|\theta_i)$$
 (7.8)

The prior is assumed to be unknown and so equation (7.8) is the central key in estimation of the parameters in the rest of the chapter. θ is partitioned into ρ , \mathbf{a} , \mathbf{Q} , μ , and σ and different methods can be employed for estimation of posteriori distribution

of each sub-parameter $r(\theta_i)$ according to (7.8).

7.2.2.1 Estimation of Dipole Locations

To estimate the dipole locations, all the ECD locations for trial k are augmented in a matrix $\mathbf{R}_k = [\rho_{k,1} \dots \rho_{k,q}] \in \mathbb{R}^{3\times q}$. The dipole locations \mathbf{R}_k have a nonlinear relation through forward matrix \mathbf{H} to the measurements, and if the real head model is used, no exact closed-form solution for \mathbf{H} exists. Therefore, nonlinear filtering is required to estimate the locations. Similar to the previous proposed method, PF for estimating $p(\mathbf{R}_k|\mathbf{Y}_{1:k})$ is used. In PF, the posteriori distribution is approximated by discrete random measures defined by particles $\{\mathbf{R}_k^{(n)}; n=1,\dots,N\}$ and their associated weights $\{w_k^{(n)}; n=1,\dots,N\}$. The posteriori distribution based on these particles and weights is approximated as:

$$p(\mathbf{R}_k|\mathbf{Y}_{1:k}) \approx \sum_{n=1}^{N} w_k^{(n)} \delta(\mathbf{R}_k - \mathbf{R}_k^{(n)})$$
(7.9)

where $\delta(.)$ is the Dirac delta function. Suppose at trial k the approximation of the posteriori distribution $p(\mathbf{R}_k|\mathbf{Y}_{1:k})$ subject to having $p(\mathbf{R}_{k-1}|\mathbf{Y}_{1:k-1})$ is desired. This means that, given the discrete random measure $\{\mathbf{R}_{k-1}^{(n)}, w_{k-1}^{(n)}; n=1,\ldots,N\}$ and the observation \mathbf{Y}_k , the weights $\{w_k^{(n)}; n=1,\ldots,N\}$ should be approximated. By using SIR-PF the weights are simply updated as

$$w_k^{(n)} \propto w_{k-1}^{(n)} p(\mathbf{Y}_k | \mathbf{R}_k^{(n)})$$
 (7.10)

In this method, the state space is explored without any knowledge of the observations. Hence, this filter can be inefficient and sensitive to any outliers. This choice, however, does have the advantage that the weights are easily evaluated. In equation (7.10), $p(\mathbf{Y}_k|\mathbf{R}_k^{(n)})$ is the likelihood function and has an equivalent distribution to the noise distribution $p(\mathbf{N}_k)$, which has already been assumed to be zero mean Gaussian with unknown covariance matrix \mathbf{Q}_k .

The resampling, which eliminates particles with small weights and replicates those with large weights is conducted in each iteration - please see Section 3.3.3 for resampling procedure.

7.2.2.2 Estimation of Dipole Amplitudes and Noise Covariance

Here, an ML estimator for the ECD amplitudes $\mathbf{a}_{k,i}$ and noise covariance matrix \mathbf{Q}_k are derived. It follows from (7.1) that the negative log-likelihood function of the observed data samples is

$$f(\boldsymbol{\theta}; \mathbf{Y}_k) = tr \left\{ [\mathbf{Y}_k - \sum_{i=1}^q \mathbf{H}(\boldsymbol{\rho}_{k,i}) \mathbf{a}_{k,i} \boldsymbol{\psi}_{k,i}]^T \mathbf{Q}_k^{-1} [\mathbf{Y}_k - \sum_{i=1}^q \mathbf{H}(\boldsymbol{\rho}_{k,i}) \mathbf{a}_{k,i} \boldsymbol{\psi}_{k,i}] \right\}$$

$$+ M \ln |\mathbf{Q}_k| + constant$$

$$(7.11)$$

By equating the gradient of $f(\theta; \mathbf{Y}_k)$ with respect to the parameter of interest $\mathbf{a}_{k,i}$, to zero, the estimation of amplitude is given by (see Appendix A)

$$\mathbf{a}_{k,i} = \left(\mathbf{H}^{T}(\boldsymbol{\rho}_{k,i})\mathbf{Q}_{k}^{-1}\mathbf{H}(\boldsymbol{\rho}_{k,i})\right)^{-1}\mathbf{H}^{T}(\boldsymbol{\rho}_{k,i})\mathbf{Q}_{k}^{-1}\left[\mathbf{Y}_{k} - \sum_{j=1,j\neq i}^{q}\mathbf{H}(\boldsymbol{\rho}_{k,j})\mathbf{a}_{k,j}\boldsymbol{\psi}_{k,j}\right]\boldsymbol{\psi}_{k,i}^{T}/\parallel\boldsymbol{\psi}_{k,i}\parallel_{2}^{2}$$
(7.12)

where $\| \cdot \|_2$ denotes the Frobenius norm. The noise covariance matrix is also estimated by minimizing the negative log-likelihood function (7.11) with respect to \mathbf{Q}_k ,

which yields (see Appendix B)

$$Q_{k} = \frac{1}{M} [Y_{k} - \sum_{i=1}^{q} H(\rho_{k,i}) a_{k,i} \psi_{k,i}] [Y_{k} - \sum_{i=1}^{q} H(\rho_{k,i}) a_{k,i} \psi_{k,i}]^{T}$$
(7.13)

If all other parameters are estimated correctly, the likelihood monotonically increases at each iteration and, therefore, convergence of the above algorithm to a local maximum is guaranteed. However, due to inaccurate estimation of the other parameters and the presence of large noise power in individual trials, $\mathbf{a}_{k,i}$ and noise covariance matrix \mathbf{Q}_k may not be truly estimated, or the filtering may diverge. To prevent these possibilities, the evolution of the parameters is assumed to be Markovian and then it can be written

$$\tilde{\mathbf{a}}_{k,i} = \tilde{\mathbf{a}}_{k-1,i} + \lambda_a (\mathbf{a}_{k,i} - \tilde{\mathbf{a}}_{k-1,i})$$

$$\tilde{\mathbf{Q}}_k = \tilde{\mathbf{Q}}_{k-1} + \lambda_Q (\mathbf{Q}_k - \tilde{\mathbf{Q}}_{k-1})$$
(7.14)

where $0 < \lambda_a, \lambda_Q \le 1$ are constant forgetting factors, and $\tilde{\mathbf{a}}_{k,i}$ and $\tilde{\mathbf{Q}}_k$ are final estimations which are updated by $\mathbf{a}_{k,i}$ and \mathbf{Q}_k . It is noteworthy that in the above equations, it is implicitly assumed that $p(\tilde{\mathbf{a}}_{k,i}|\tilde{\mathbf{a}}_{k-1,i})$ and $p(\tilde{\mathbf{Q}}_k|\tilde{\mathbf{Q}}_{k-1})$ are Gaussian zero mean distributions. These recursive equations prevent sudden changes of amplitude and noise covariance because of some highly noisy individual trials, and guarantee the stability of the filtering for sufficiently small values of λ_a and λ_Q .

7.2.2.3 Estimation of Temporal Basis Parameters

Dipole temporal basis parameters are the mean $\mu_{k,i}$ and the variance $\sigma_{k,i}$ of Gaussian waveforms. They have nonlinear relations to the measurements. In general, the optimization problem in (7.11) does not appear to provide a closed-form solution

for $\mu_{k,i}$ and $\sigma_{k,i}$. Iterative methods, therefore, may be employed to estimate the temporal basis parameters. Newton-Raphson technique is a well established method that can be used to solve this problem approximately [55]. The main benefit of Newton-Raphson's method is its fast convergence, especially if the iteration begins sufficiently near to the minimum point. Hence, this method is suitable to be coupled with the other methods for simultaneous estimation of parameters.

In the Newton-Raphson technique, the following formulation is used to estimate the temporal basis parameters θ_k based on θ_{k-1} at each iteration [55]:

$$\theta_k = \theta_{k-1} - \lambda_{\theta} \left[\frac{\partial^2 f(\theta; \mathbf{Y}_k)}{\partial \theta_k^2} \right]^{-1} \frac{\partial f(\theta; \mathbf{Y}_k)}{\partial \theta_k}$$
 (7.15)

For the same reason mentioned in the previous section, a forgetting factor $0 < \lambda_{\theta} \le 1$ to the original Newton-Raphson equation was added. This guarantees the stability of the filtering in the case of very low SNRs. Equation (7.15) needs the first and second order gradients of log-likelihood function $f(\theta; \mathbf{Y}_k)$ with respect to $\mu_{k,i}$ and $\sigma_{k,i}$. By defining $\boldsymbol{\xi}(t) = \mathbf{y}_k(t) - \sum_{i=1}^q \mathbf{H}(\boldsymbol{\rho}_{k,i}) \mathbf{a}_{k,i} \psi_{k,i}(t)$ and $\boldsymbol{\alpha}_{k,i} = \mathbf{H}(\boldsymbol{\rho}_{k,i}) \mathbf{a}_{k,i}$, the gradients with respect to $\mu_{k,i}$ can be calculated and simplified as (see Appendix C)

$$\frac{\partial f(\boldsymbol{\theta}; \mathbf{Y}_k)}{\partial \mu_{k,i}} = \frac{2}{\sigma_{k,i}^2} \sum_{t=1}^{M} (\mu_{k,i} - t) \psi_{k,i}(t) \boldsymbol{\alpha}_{k,i}^T \mathbf{Q}_k^{-1} \boldsymbol{\xi}(t)$$
 (7.16)

$$\frac{\partial^2 f(\boldsymbol{\theta}; \mathbf{Y}_k)}{\partial \mu_{k,i}^2} = \frac{2}{\sigma_{k,i}^2} \sum_{t=1}^M (1 - \frac{1}{\sigma_{k,i}^2} (\mu_{k,i} - t)^2) \psi_{k,i}(t) \boldsymbol{\alpha}_{k,i}^T \mathbf{Q}_k^{-1} \boldsymbol{\xi}(t) + \frac{1}{\sigma_{k,i}^2} (\mu_{k,i} - t)^2 \psi_{k,i}(t)^2 \boldsymbol{\alpha}_{k,i}^T \mathbf{Q}_k^{-1} \boldsymbol{\alpha}_{k,i}$$
(7.17)

Similarly, the first and second order gradients of the likelihood function with respect

to $\sigma_{k,i}$ are as follows:

$$\frac{\partial f(\boldsymbol{\theta}; \mathbf{Y}_k)}{\partial \sigma_{k,i}} = -\frac{2}{\sigma_{k,i}^3} \sum_{t=1}^M (\mu_{k,i} - t)^2 \psi_{k,i}(t) \boldsymbol{\alpha}_{k,i}^T \mathbf{Q}_k^{-1} \boldsymbol{\xi}(t)$$
 (7.18)

$$\frac{\partial^2 f(\boldsymbol{\theta}; \mathbf{Y}_k)}{\partial \sigma_{k,i}^2} = \frac{2}{\sigma_{k,i}^4} \sum_{t=1}^M (3 - \frac{1}{\sigma_{k,i}^2} (\mu_{k,i} - t)^4) \psi_{k,i}(t) \boldsymbol{\alpha}_{k,i}^T \mathbf{Q}_k^{-1} \boldsymbol{\xi}(t) + \frac{1}{\sigma_{k,i}^2} (\mu_{k,i} - t)^4 \psi_{k,i}(t)^2 \boldsymbol{\alpha}_{k,i}^T \mathbf{Q}_k^{-1} \boldsymbol{\alpha}_{k,i}.$$
(7.19)

It is evident that to model the ERP waveforms, any other parametric function that has first and second order continuous derivations can be employed instead of a Gaussian function.

The temporal basis parameters of ERP subcomponents estimated by the above formulation may not be the optimum values related to the global minimum of the algorithm, and they depend on the initial points. Due to nonlinearity of the latency and width, the Newton-Raphson method is more sensitive to the initialization than the PF and ML methods (both PF and ML can be considered as global minimizers). As a result, equation (7.15) needs an accurate estimate of the initial points, which can be chosen according to the latency and width of the fitted Gaussian waveforms to the ensemble average over all trials. The procedure of selecting initial points will be explained further in the real data section.

Although PF can again be employed to estimate the nonlinear parameters $\mu_{k,i}$ and $\sigma_{k,i}$, it requires extensive memory and computational time, which limits its application. Especially in the presence of multiple ECDs, it may be intractable to use PF for estimation of all of the parameters.

7.2.2.4 Overall Algorithm

The aim of the overall algorithm is to update the parameters recursively based on the available measurements. The pseudo-code of the method is presented in Algorithm 5. In this method, each particle not only holds a parameter for location $\rho_{k,i}^{(n)}$, but holds parameters for amplitude $\mathbf{a}_{k,i}^{(n)}$, width $\sigma_{k,i}^{(n)}$, and latency $\mu_{k,i}^{(n)}$ of the ERP subcomponents. Note that, in this algorithm the estimated noise covariance matrix \mathbf{Q}_k is used to update the weights using the likelihood function in equation (7.10).

In this method, the evolution of the locations (i.e. states in PF) is assumed to be a first order Markovian process as

$$\mathbf{R}_k = \mathbf{R}_{k-1} + \mathbf{W}_k \tag{7.20}$$

where \mathbf{W}_k is GWN with known covariance matrix $\lambda_{\rho}\mathbf{I}$. Here, \mathbf{I} is the identity matrix and λ_{ρ} is a scalar that represents the noise power. Hence, the distribution $p(\mathbf{R}_k|\mathbf{R}_k^{(n-1)},\mathbf{Y}_k)$ in Algorithm 5 has Gaussian zero mean distribution with covariance matrix $\lambda_{\rho}\mathbf{I}$.

The proposed method is a grid based method by which the brain is divided into sufficiently small three-dimensional grid cells and the location of each ECD is restricted to one of these cells. Therefore, before updating the weights, if the location indicated by each particle is not one of those grid cells, it is replaced by the nearest cell. The grid based method helps the use of the real head model and any form of forward solution. Moreover, depending on the number of grid cells, the computational complexity considerably decreases compared to non grid based methods.

Algorithm 5 Pseudo-code for the proposed method used for identifying ERP subcomponents

 $set \ k = 0$ and generate random matrices $\mathbf{R_0^{(n)}}$ according to Gaussian distribution with mean in the initial ECD locations.

set $\mu_{0,i}^{(n)}$ and $\sigma_{0,i}^{(n)}$ equal to the parameters of Gaussian waveforms fitted to the average of ERPs over all trials.

for k = 1 to K do $\{K \text{ is the number of trials}\}$

- draw $R_k^{(n)}$ according to $p(R_k|R_k^{(n-1)}, Y_k)$. replace each column of $R_k^{(n)}$ with the nearest grid cell.

- update new weights $w_k^{(n)}$ according to equation (7.10). normalize the weights $w_k^{(n)} = w_k^{(n)} / \sum_{n=1}^N w_k^{(n)}$. update $\tilde{\mathbf{a}}_{k,i}^{(n)}$ for each particle and $\tilde{\mathbf{Q}}_k$ given $\rho_{k,i}^{(n)}$, $\sigma_{k,i}^{(n)}$, $\mu_{k,i}^{(n)}$ and \mathbf{Y}_k using equa-
- tions (7.12) (7.14). update $\sigma_{k,i}^{(n)}$ and $\mu_{k,i}^{(n)}$ given $\mathbf{a}_{k,i}^{(n)}$, $\boldsymbol{\rho}_{k,i}^{(n)}$ and \mathbf{Y}_k for each particle using equations (7.15) (7.19).
- resample N particles $\mathbf{R}_{k}^{(n)}$ with replacement according to their importance weights $w_k^{(n)}$.

end for

7.3 Results

In this section, the proposed method is applied to synthetic and real EEG data to validate the approach and demonstrate its application in an empirical setting.

7.3.1 Simulated Data Results

A set of EEG data is generated containing ERP waves in the interval between 200ms and 500ms post-stimulus which contains a P300 component. The sampling frequency was set to 250Hz and the number of trials to 60. These characteristics were chosen in order to match those for the real EEG data set to which the approach was applied subsequently. Two moving sources, one in frontal and one in parietal loci, were used for simulating the ERP subcomponents. Gaussian waves, for which their amplitudes, latencies, and widths were varied across trials, were employed. The amplitude profile of the frontal source (first source) was assumed to decrease linearly, but its latency and width were assumed to be approximately constant across trials. The amplitude profile of the parietal source (second source) was assumed to be approximately constant, but its latency and width to decrease linearly across trials. GWN with different levels was added to the amplitudes, latencies, and widths of both sources. Spatially correlated Gaussian noise is added to the simulated EEG signal to achieve a realistic SNR. The available noise power in the simulated multichannel EEG is measured by SNR in dB unit, which is defined as

$$SNR = 10\log(\frac{P_{signal}}{P_{noise}}) \tag{7.1}$$

where P_{signal} and P_{noise} denote, respectively, the power of the simulated EEG and noise.

Fig. 7.1 shows a typical example of the noiseless and noisy simulated ERPs. Noiseless trial numbers 5 and 55 are shown in Fig. 7.1(a) and (b), and the noisy trials are shown in Fig. 7.1(c) and (d), respectively (for SNR = -5dB). Note that the signal waveform is not visible in the noisy single trial data.

Fig. 7.2 shows the simulated and estimated amplitude, latency, and width of the frontal (red lines) and the parietal (blue lines) sources for the data with SNR = 5dB. Fig. 7.3 depicts the simulated and estimated locations in axial and sagittal views for the same data. Because of the small amount of noise, $\lambda_{\rho} = 0.001$, $\lambda_{a} = 1$, $\lambda_{Q} = 1$, $\lambda_{\mu} = 1$ and $\lambda_{\sigma} = 1$ was chosen. These values preserve the Markovian assumption for the parameters. The number of particles N was set to 1000 during all experiments. Figs. 7.2 and 7.3 imply that in the presence of moderate noise power, the proposed method can detect the ERP subcomponent parameters and track their variability

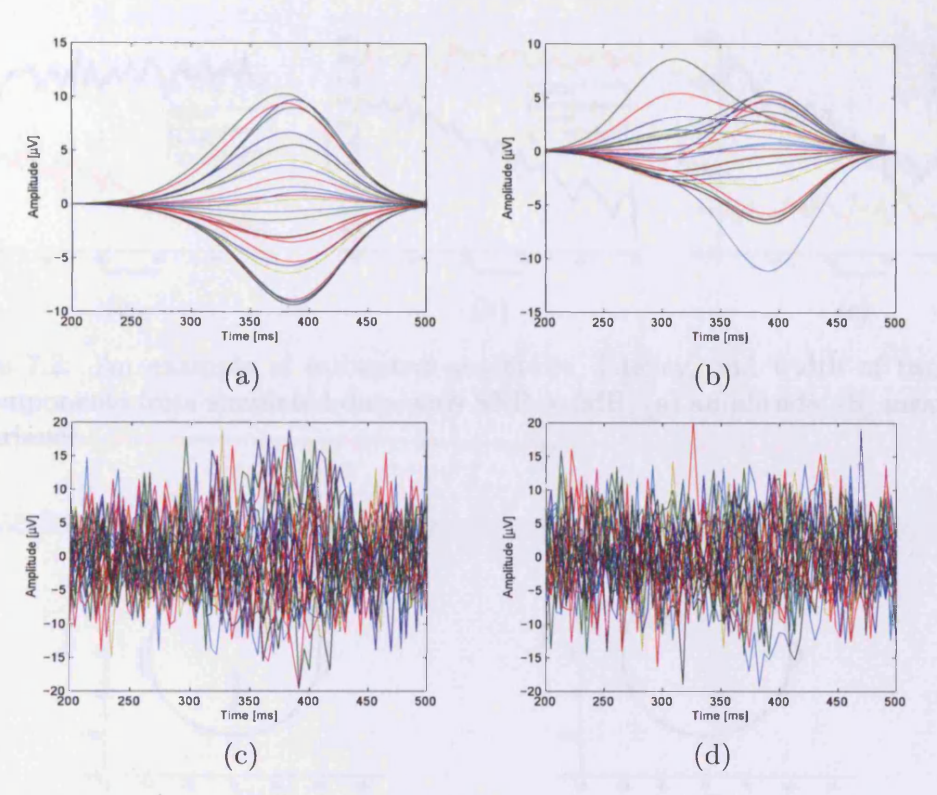


Figure 7.1: An example of simulated EEG data with SNR = -5dB, (a) original number 5 trial for multichannel EEG, (b) original number 55 trial, (c) noisy number 5 trial, and (d) noisy number 55 trial.

accurately.

Similar results for the simulated data with SNR = -5dB are shown in Figs. 7.4 and 7.5. The forgetting factors were set as $\lambda_{\rho} = 0.001, \lambda_{a} = 0.9, \lambda_{Q} = 0.9, \lambda_{\mu} = 0.8$ and $\lambda_{\sigma} = 0.8$. If these values are chosen to be the same as those employed for the previous simulation, the algorithm will diverge on some of the trials. In practice, these values should be chosen empirically and according to the SNR of the available data set. Note Figs. 7.4 and 7.5 imply that although the errors for some of the individual trials are large, the proposed approach at least reveals the trends for the temporal

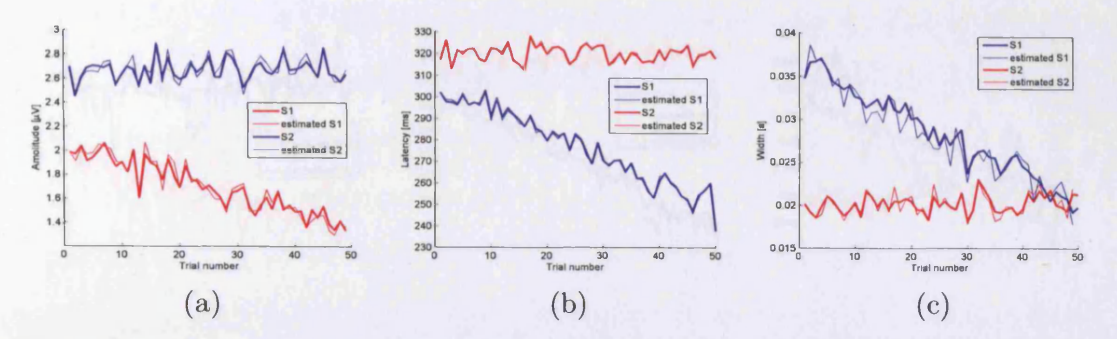


Figure 7.2: An example of estimated amplitude, latency, and width of two ERP subcomponents from simulated data with SNR = 5dB, (a) amplitude, (b) mean, and (c) variance.

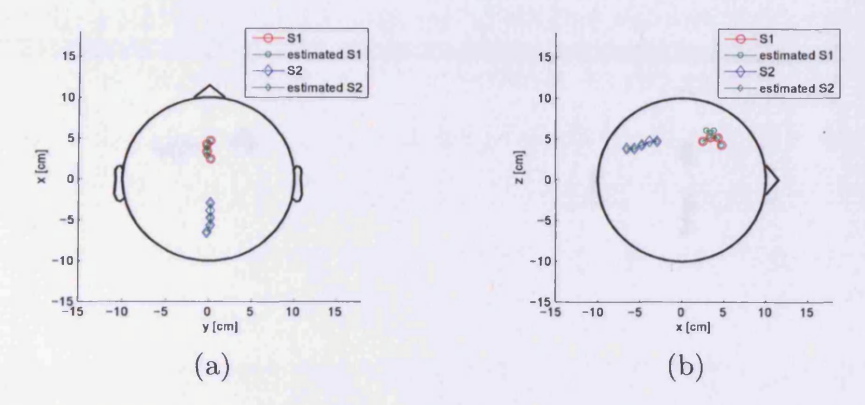


Figure 7.3: Estimated locations using the proposed method for Fig. 7.2 in (a) axial and (b) sagittal views.

basis parameters and locations.

The proposed method for identification and separation of ERP subcomponent is fundamentally different from the other approaches for ERP analysis (see equation (7.1)), and to the best of our knowledge, there is no method that can simultaneously estimate all ERP subcomponent parameters and localize and track their locations as this method does. Therefore, the above simulation results were not compared with those of the other methods.

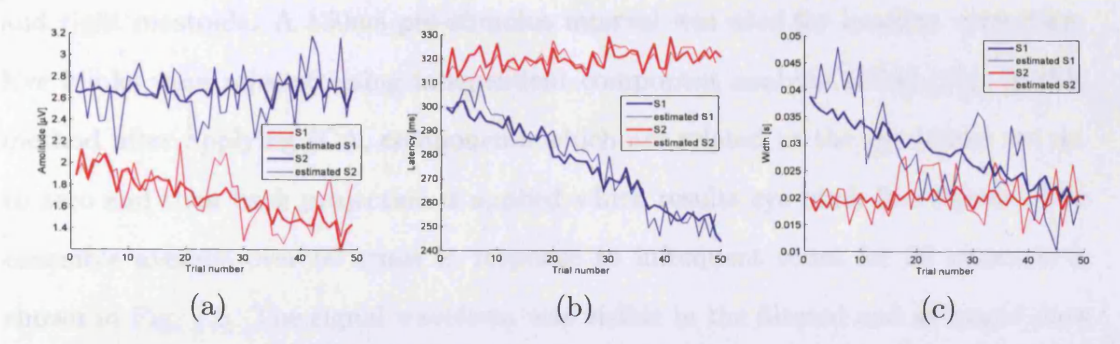


Figure 7.4: An example of the estimated amplitude, latency, and width of two ERP subcomponents in simulated data with SNR = -5dB, (a) amplitude, (b) latency, and (c) width.

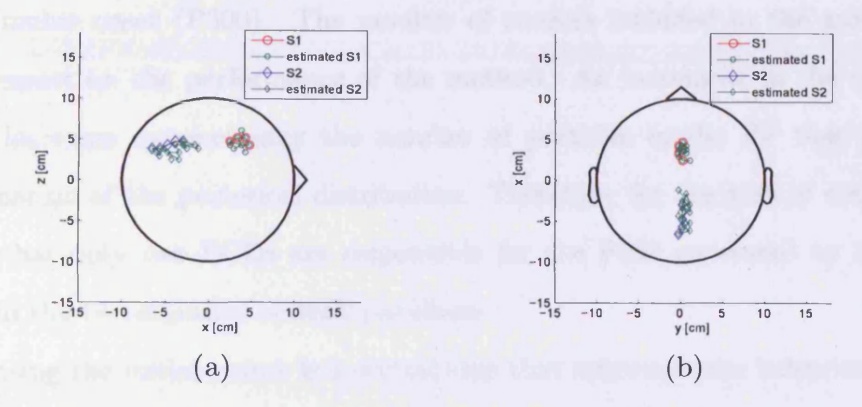


Figure 7.5: Estimated locations using the proposed method for Fig. 7.4 in (a) axial and (b) sagittal views.

7.3.2 Real Data Results

Real data was obtained in an *oddball* paradigm. The subject was a female, right-handed undergraduate student. She heard in total 300 tones, 240 (80%) of which were frequent and 60 (20%) of which were infrequent. During acquisition, the frequency bandwidth of the linear bandpass filter was 0.03-40Hz and the sampling rate was 250Hz.

The data were re-referenced off-line to the algebraic mean of the signals at the left

and right mastoids. A 150ms pre-stimulus interval was used for baseline correction. Eye blinks were rejected using independent component analysis (ICA) [24]. In this method after applying ICA, components which are related to the eye blinks are set to zero and then back projection is applied which results eye blink free signals. The ensemble average over 60 trials in response to infrequent tones for 25 channels is shown in Fig. 7.6. The signal waveform was visible in the filtered and averaged data but not in the single-trial data. Fig. 7.6 shows two dominant peaks, one negative peak approximately 100ms post-stimulus and one positive peak approximately 300ms after stimulus onset (P300). The number of sources included in the model has a major impact on the performance of the method. An increment in the number of sources increases exponentially the number of particles in the PF that is needed for estimation of the posteriori distribution. Therefore, for the sake of convenience, assume that only two ECDs are responsible for the P300 generated by infrequent stimuli in the two-stimulus oddball paradigm.

Choosing the initial points is a crucial step that influences the behavior and convergence of the filtering procedure. To determine the initial points for the amplitude, latency, and width of each subcomponent the data is average referenced and segmented around the P300 component. Also, the initial location is assumed to be frontal site for P3a and parietal site for P3b. Epochs from 200ms to 500ms time-locked to stimulus onset for infrequent trials only were extracted. By assuming that the location is fixed, Gaussian waves were fitted to the data. Since the average data benefits from less noise compared to single trial data, all the forgetting factors were set to 1. The algorithm was executed until the results remained the same. The real

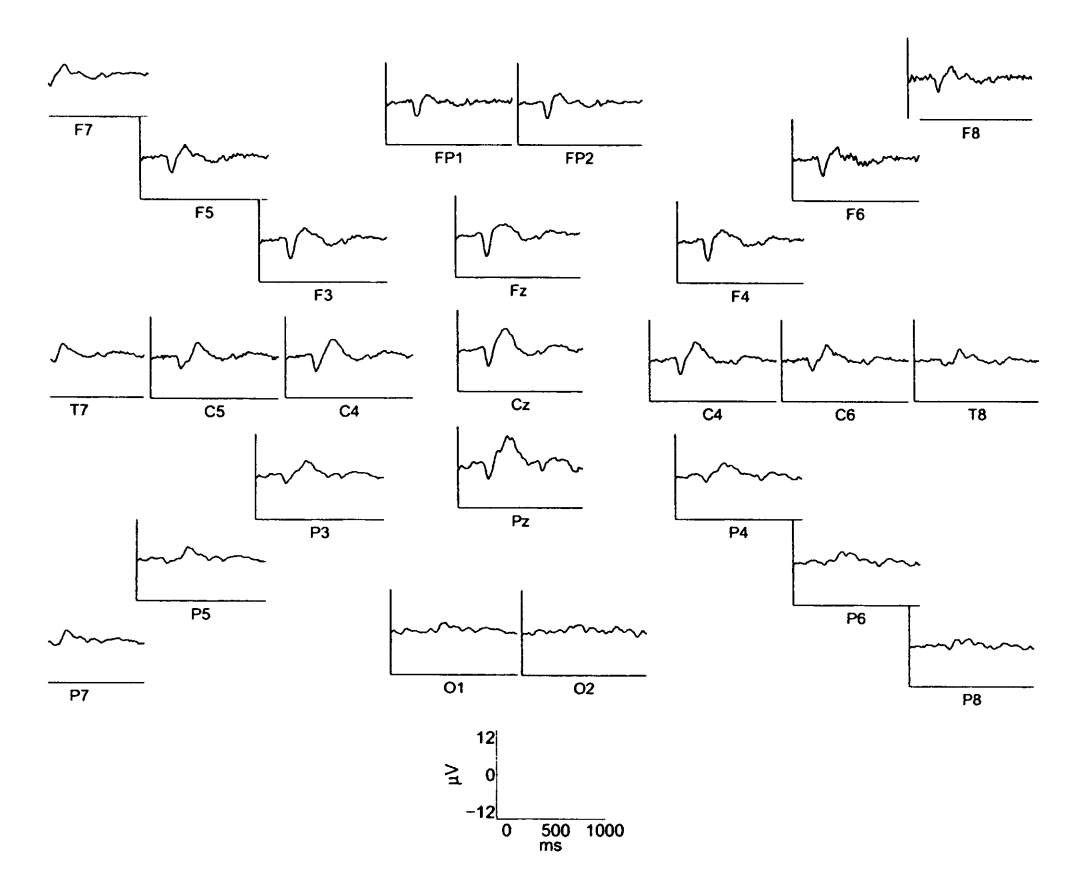


Figure 7.6: Average ERP over 60 trials of real data for a female subject. The lower diagram represents the amplitude and time scales for all the plots. P300 amplitude can be seen better in the central sensors.

and fitted data for 25 channels are shown in Fig. 7.7 by red and blue lines, respectively. The amplitude, latency, and width of the fitted data were used to initialize the algorithm.

During the running of the algorithm, $\lambda_{\rho} = 0.001, \lambda_{a} = 0.9, \lambda_{Q} = 0.9, \lambda_{\mu} = 0.8$ and $\lambda_{\sigma} = 0.8$ was chosen. Setting all forgetting factors to 1 causes divergence of the filtering progress for this subject. The estimated amplitude, latency, and width of the P3a and P3b subcomponents are shown in Fig. 7.8. The amplitudes are the absolute values of the three dimensional ECD amplitude moments. The figure shows

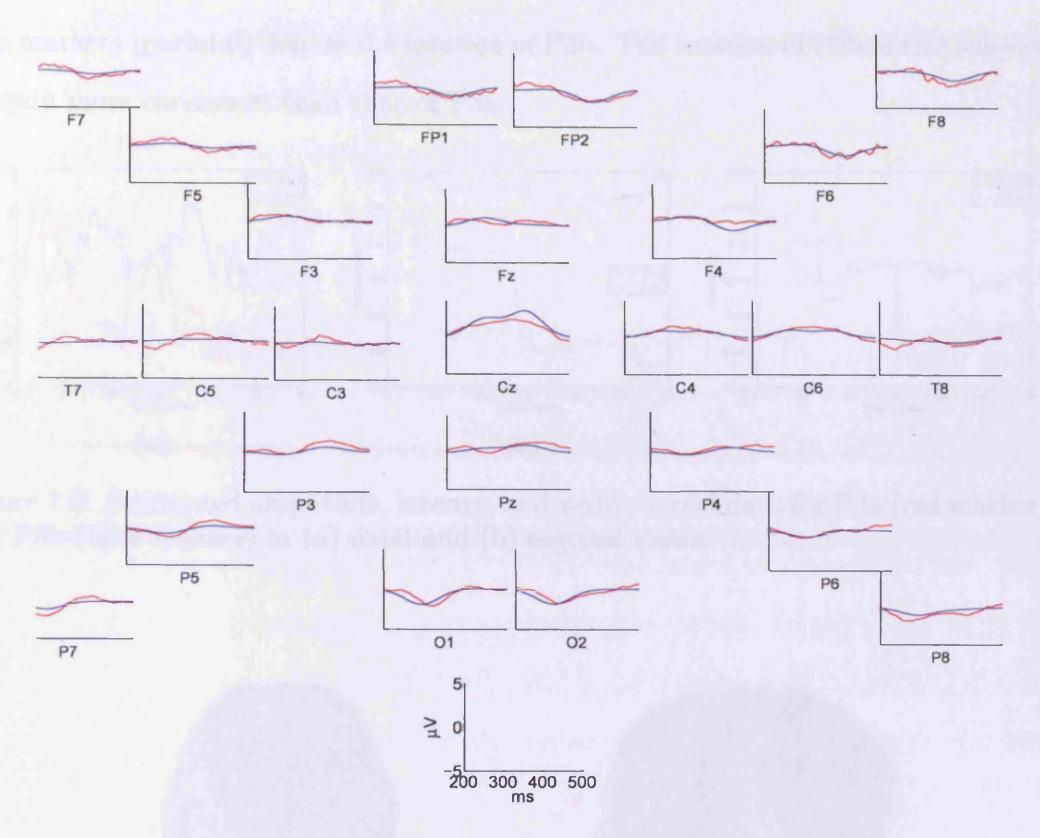


Figure 7.7: Average re-referenced and segmented data around P300 (200ms-500ms) shown with red lines and fitted data shown with blue lines. The lower diagram represents the amplitude and time scales for all the plots. The parameters of the fitted waveforms were used for initializing the algorithm.

that the amplitude of P3b is more stationary than that of P3a on most trials. P3a amplitude diminishes from trial to trial while P3b is approximately constant. The latency of P3a is shorter than that of P3b (P3a occurs earlier than P3b: [87]), and in addition, P3b latency is less variable than P3a latency. Also, the width of P3b is larger and more stable than that of P3a, as would be expected given previous empirical findings. Fig. 7.9 depicts the estimated locations of P3a and P3b in axial and sagittal views. The red markers (frontal) denote the location of P3a while the

blue markers (parietal) denote the location of P3b. The location of P3b in this subject is again more consistent than that of P3a.

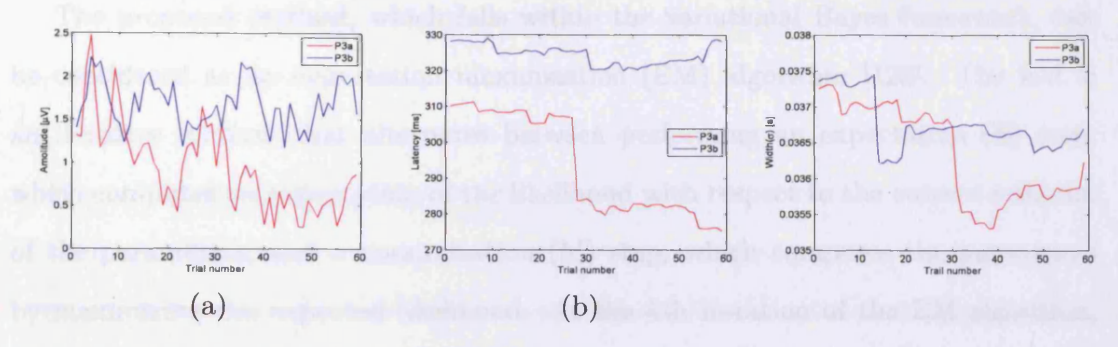


Figure 7.8: Estimated amplitude, latency, and width in real data for P3a (red marker) and P3b (blue marker) in (a) axial and (b) sagittal views.

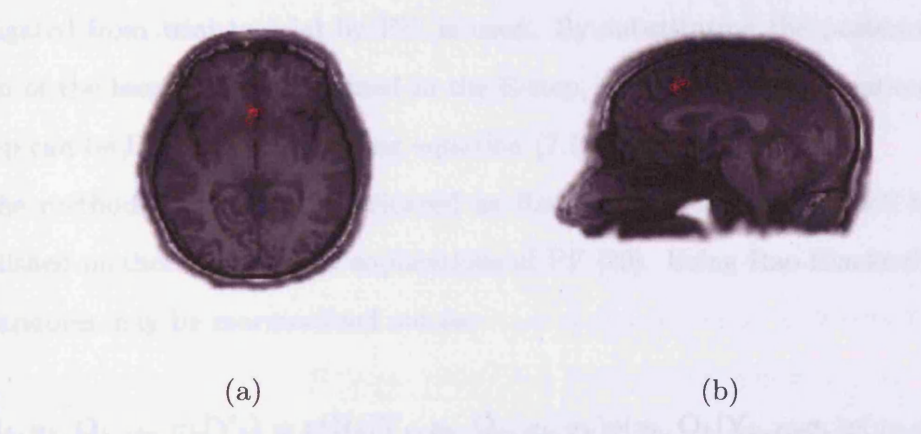


Figure 7.9: Estimated locations of P3a (red marker) and P3b (blue marker).

7.4 Discussion

The proposed approach has the ability to both localize and track ECD locations. Localizing and tracking ECDs can have many benefits in the application of ERP analysis in circumstances where the locations of dipoles may change during the course of recording [89].

The proposed method, which falls within the variational Bayes framework, can be considered as an expectation maximization (EM) algorithm [123]. The EM is an iterative method that alternates between performing an expectation (E) step, which computes an expectation of the likelihood with respect to the current estimate of the parameters, and a maximization (M) step, which computes the parameters by maximizing the expected likelihood. At the kth iteration of the EM algorithm, the distribution of interest for the E-step is $p(\mathbf{R}_k|\mathbf{Y}_k,\boldsymbol{\theta}_k^{IR})$, where $\boldsymbol{\theta}_k^{IR}$ represents all the parameters except the location. In the proposed model it is nonlinear and this distribution is intractable. Instead, an approximation to this distribution, which is propagated from trial to trial by PF, is used. By substituting the posterior distribution of the locations \mathbf{R}_k obtained in the E-step, the required optimization for the M-step can be found by maximizing equation (7.11) with respect to $\boldsymbol{\theta}_k^{IR}$.

The method can also be considered as Rao-Blackwellized PF, which is a well established method in different applications of PF [29]. Using Rao-Blackwellization, the variables may be marginalized out as

$$p(\mathbf{R}_k, \mathbf{a}_k, \mathbf{Q}_k, \mu_k, \sigma_k | \mathbf{Y}_k) = p(\mathbf{R}_k | \mathbf{Y}_k, \mathbf{a}_k, \mathbf{Q}_k, \mu_k, \sigma_k) p(\mathbf{a}_k, \mathbf{Q}_k | \mathbf{Y}_k, \mu_k \sigma_k) p(\mu_k, \sigma_k | \mathbf{Y}_k)$$
(7.1)

The above equation implies that each distribution can be estimated using different methods. Here, assume that the parameters are independent. Equation (7.1), which is the product of \mathbf{H} , \mathbf{a}_k , and $\boldsymbol{\psi}_k$, entails that the parameters are indeed independent. \mathbf{H} is a function of $\boldsymbol{\rho}_k$ and $\boldsymbol{\psi}_k$ is a function of σ_k and μ_k .

In this study it is assumed that the evolution of the parameters is a first order Markov model and the transition probabilities are known. Hence, the method trades off between reducing the noise power and following any sudden changes. In other words, if the signal has moderate noise power, or the variability across trials is smooth, the method can be applied successfully. On the other hand, if the signal is very noisy and has sudden changes in parameter values, this method may not estimate the parameters accurately. In this case, it may give us a trend for parameters from trial to trial, which can be used effectively in circumstances where it is reasonable to assume that the components or subcomponents of interest will either decrease or increase (in either amplitude or latency) over time. Studies of the effects of habituation, learning and fatigue are good examples of this kind. It is also notable that this approach relies on weaker assumptions than those in other methods (e.g. ensemble averaging and ML), which assume that the temporal basis or the locations of the sources remain the same across trials.

When the noise temporally is independent and identically distributed the signal quality is improved. Different results are likely if the noise is strongly correlated with time, such as when it is due to large amplitude alpha rhythms. Unknown temporal noise correlations can thus adversely affect the result of the method. The method is most suitable for scenarios in which the noise is strongly correlated in the spatial dimension and offers significant advantages relative to the methods which assume the statistics of the noise remain the same during the course of recording [62].

In the real data results (oddball paradigm), a complete and accurate localization of all sources contributing to P300 is not likely to be possible at the present time [82]. It is widely accepted, however, that fronto-parietal interactions are one of the main

contributors and as a result, the current work emphasizes the potential for being able to compare how frontal and partial contributions vary with time across groups [32]. For example, the method can be applied to compare variation of P3a and P3b in young and old participants, or between controls and individuals with organic or psychiatric disorders.

Finally, although PF has the ability to converge to the global minimum, the initial locations are assumed to be known a priori. This is because the number of trials was limited (converging to a local minimum needs some iterations) and the signal was contaminated with a high level of noise. The initial locations were chosen according to widely documented knowledge (e.g. [32]) about the ERP components that are observed in odd-ball experiments. Initial points could be assigned on the basis of other kinds of information, for example the outcomes of studies in which haemodynamic measures of neural activity are acquired in the same tasks for which ERPs are then analyzed subsequently.

7.5 Conclusions

In this chapter, a novel method for identifying ERP subcomponents was introduced. The ERP subcomponent sources were modeled by ECDs and their moments were modeled by Gaussian waves. The unknown parameters of the model were estimated using PF, ML and the Newton-Raphson technique from trial to trial, and the evolution of the parameters was assumed to be a first order Markovian process. The results obtained from simulation and real data showed the potential use of the method in real applications.

Reliably extracting the ERP subcomponents in each trial would be of great benefit in contrasting ERPs across different patient groups. In this context, the existence of a reliable means of extracting ERP subcomponents offers a means of assessing whether factors such as habituation and fatigue influence ERPs differently according to variables such as the disease state or severity, or the location of focal brain damage. Assessment of the performance of the approach described here in populations other than healthy young adults is one way in which this work will be taken forward subsequently.

Appendix

A ML Estimation of $\mathbf{a}_{k,i}$

Using [85]

$$\frac{\partial}{\partial \mathbf{s}} (\mathbf{x} - \mathbf{A}\mathbf{s})^T \mathbf{W} (\mathbf{x} - \mathbf{A}\mathbf{s}) = -2\mathbf{A}^T \mathbf{W} (\mathbf{x} - \mathbf{A}\mathbf{s})$$
(A1)

derivative of (7.11) with respect to $\mathbf{a}_{k,i}$ at time t becomes:

$$\left. \frac{\partial}{\partial \mathbf{a}_{k,i}} f(\boldsymbol{\theta}; \mathbf{Y}_k) \right|_{t=t} = -2\mathbf{H}^T(\boldsymbol{\rho}_{k,i}) \psi_{k,i}(t) \mathbf{Q}_k^{-1} \left(\mathbf{y}_k(t) - \sum_{j=1}^q \mathbf{H}(\boldsymbol{\rho}_{k,j}) \mathbf{a}_{k,j} \psi_{k,j}(t) \right)$$
(A2)

where $y_k(t)$ is the tth column of Y_k . Accumulating equation (A2) for t = 1 to M and making it equal to zero results:

$$\sum_{t=1}^{M} \mathbf{H}^{T}(\boldsymbol{\rho}_{k,i}) \psi_{k,i}(t) \mathbf{Q}_{k}^{-1} \mathbf{H}(\boldsymbol{\rho}_{k,i}) \mathbf{a}_{k,i} \psi_{k,i}(t) = \\
\sum_{t=1}^{M} \mathbf{H}^{T}(\boldsymbol{\rho}_{k,i}) \psi_{k,i}(t) \mathbf{Q}_{k}^{-1} (\mathbf{y}_{k}(t) - \sum_{j=1, j \neq i}^{q} \mathbf{H}(\boldsymbol{\rho}_{k,j}) \mathbf{a}_{k,j} \psi_{k,j}(t))$$
(A3)

Using the above equation and the following facts:

$$\|\psi_{k,i}\|_2^2 = \sum_{t=1}^M \psi_{k,i}^2(t)$$
 (A4)

$$\sum_{t=1}^{M} \psi_{k,i}(t) (\mathbf{y}_{k}(t) - \sum_{j=1, j \neq i}^{q} \mathbf{H}(\boldsymbol{\rho}_{k,j}) \mathbf{a}_{k,j} \psi_{k,j}(t)) =$$

$$([\mathbf{y}_{k}(1) \dots \mathbf{y}_{k}(M)] - \sum_{j=1, j \neq i}^{q} \mathbf{H}(\boldsymbol{\rho}_{k,j}) \mathbf{a}_{k,j} [\psi_{k,j}(1) \dots \psi_{k,j}(M)]) [\psi_{k,i}(1) \dots \psi_{k,i}(M)]^{T} =$$

$$(\mathbf{Y}_{k} - \sum_{j=1, j \neq i}^{q} \mathbf{H}(\boldsymbol{\rho}_{k,j}) \mathbf{a}_{k,j} \psi_{k,j}) \psi_{k,i}^{T}$$
(A5)

equation (7.12) is obtained.

B ML Estimation of Q_k

Using the following equations [85]

$$\frac{\partial tr\{\mathbf{A}\mathbf{W}^{-1}\mathbf{B}\}}{\partial \mathbf{W}} = -(\mathbf{W}^{-1}\mathbf{B}\mathbf{A}^{T}\mathbf{W}^{-1})$$
 (B1)

$$\frac{\partial |\mathbf{W}|}{\partial \mathbf{W}} = |\mathbf{W}|\mathbf{W}^{-T} \tag{B2}$$

the derivative of (7.11) with respect to \mathbf{Q}_k becomes

$$\frac{\partial}{\partial \mathbf{Q}_{k}} f(\boldsymbol{\theta}; \mathbf{Y}_{k}) =
-\frac{1}{M} \left(\mathbf{Q}_{k}^{-1} [\mathbf{Y}_{k} - \sum_{i=1}^{q} \mathbf{H}(\boldsymbol{\rho}_{k,i}) \mathbf{a}_{k,i} \boldsymbol{\psi}_{k,i}] [\mathbf{Y}_{k} - \sum_{i=1}^{q} \mathbf{H}(\boldsymbol{\rho}_{k,i}) \mathbf{a}_{k,i} \boldsymbol{\psi}_{k,i}]^{T} \mathbf{Q}_{k}^{-1} \right)^{T} + \mathbf{Q}_{k}^{-T} = 0$$
(B3)

Post multiplication of equation (B3) by \mathbf{Q}_k^T and recognizing that $\mathbf{Q}_k = \mathbf{Q}_k^T$ results:

$$-\frac{1}{M}\mathbf{Q}_{k}^{-1}[\mathbf{Y}_{k} - \sum_{i=1}^{q} \mathbf{H}(\boldsymbol{\rho}_{k,i})\mathbf{a}_{k,i}\boldsymbol{\psi}_{k,i}][\mathbf{Y}_{k} - \sum_{i=1}^{q} \mathbf{H}(\boldsymbol{\rho}_{k,i})\mathbf{a}_{k,i}\boldsymbol{\psi}_{k,i}]^{T} + \mathbf{I} = 0$$
 (B4)

Equation (B4) simply results in:

$$\mathbf{Q}_{k} = \frac{1}{M} [\mathbf{Y}_{k} - \sum_{i=1}^{q} \mathbf{H}(\boldsymbol{\rho}_{k,i}) \mathbf{a}_{k,i} \boldsymbol{\psi}_{k,i}] [\mathbf{Y}_{k} - \sum_{i=1}^{q} \mathbf{H}(\boldsymbol{\rho}_{k,i}) \mathbf{a}_{k,i} \boldsymbol{\psi}_{k,i}]^{T}.$$
(B5)

C Derivation of Equations (7.16) and (7.17)

Equation (7.16) can be obtained similar to the calculations in Appendix A. Using equation (A1), the derivative of negative log-likelihood with respect to $\mu_{k,i}$ at time t can be written as:

$$\left. \frac{\partial f(\boldsymbol{\theta}; \mathbf{Y}_k)}{\partial \mu_{k,i}} \right|_{t=t} = -2(\mathbf{H}(\boldsymbol{\rho}_{k,i}) \mathbf{a}_{k,i} \frac{\partial \psi_{k,i}(t)}{\partial \mu_{k,i}})^T \mathbf{Q}_k^{-1} (\mathbf{y}_k(t) - \sum_{i=1}^q \mathbf{H}(\boldsymbol{\rho}_{k,i}) \mathbf{a}_{k,i} \psi_{k,i}(t)) \quad (C1)$$

again $\mathbf{y}_{k}(t)$ is the tth column of \mathbf{Y}_{k} . By accumulating the above equation for t=1 to M and using the fact that $\frac{\partial \psi_{k,i}(t)}{\partial \mu_{k,i}} = \frac{t-\mu_{k,i}}{\sigma_{k,i}^{2}} \psi_{k,i}(t)$, after some algebra equation (7.16) follows.

The second order derivative of the negative log-likelihood with respect to $\mu_{k,i}$ is equal to the derivative of equation (7.16):

$$\frac{\partial^{2} f(\boldsymbol{\theta}; \mathbf{Y}_{k})}{\partial \mu_{k,i}^{2}} = \frac{2}{\sigma_{k,i}^{2}} \sum_{t=1}^{M} \frac{\partial (\mu_{k,i} - t)}{\partial \mu_{k,i}} \psi_{k,i}(t) \boldsymbol{\alpha}_{k,i}^{T} \mathbf{Q}_{k}^{-1} \boldsymbol{\xi}(t) + (\mu_{k,i} - t) \frac{\partial \psi_{k,i}(t)}{\partial \mu_{k,i}} \boldsymbol{\alpha}_{k,i}^{T} \mathbf{Q}_{k}^{-1} \boldsymbol{\xi}(t) + (\mu_{k,i} - t) \psi_{k,i}(t) \boldsymbol{\alpha}_{k,i}^{T} \mathbf{Q}_{k}^{-1} \frac{\partial \boldsymbol{\xi}(t)}{\partial \mu_{k,i}} \tag{C2}$$

which after some algebra results in equation (7.17).

Chapter 8

Summary, Conclusions, and Future Works

8.1 Summary and Conclusions

In the past, communication between the neuroscience and signal processing communities has been limited. However, because of the realization of mutual requirements and interests by researchers from both areas, the two communities are working together more frequently. This means increased opportunities for the investigation of normal brain functions and the diagnosis of abnormalities. Two main problems for the neuroscience community may be addressed by signal processing experts. The first is single trial estimation and the second is source localization of E/MEG data. During the past three decades, many approaches to both problems have been developed.

This study proposed a new method for single trial estimation, two new methods for source localization, plus a novel method for simultaneous single trial estimation and source localization. These methods have many possible applications in neuro-science, engineering and medicine. For instance, ERP analysis can be used to identify and classify individual ERP responses that are not accompanied by overt behavioral responses. Due to the consistency of the P300 response to novel stimuli, a brain-computer interface might also be constructed relying on the proposed ST-ERP estimation or E/MEG source localization methods described here. Furthermore, the methods can be used as assessment tools for patients who are only able to provide minimal cooperation and/or few behavioral responses. They also may have benefits for localization of epileptic foci. In the following paragraphs the proposed approaches are summarized.

As was emphasized in the introductory chapter, one of the main problems in ERP research is the destructive effect of artifacts which can mask the signal of interest. A desirable development, therefore, is accurate single-trial estimation of ERPs. In chapter 4, a method developed to mitigate the effect of noise in each single trial based on PF and discrete wavelet transformation of ERPs was reported. The main advantages of the proposed method are in employing sequential importance sampling and Bayesian theory combined with DWT, which promises a high performance in the presence of non-Gaussian and non-stationary noise. This method uses only one EEG channel for ST-ERP extraction and, therefore, ignores spatial information contained in E/MEG data. Moreover, it may be more sensitive to outliers than other methods such as the MAP estimator, since no prior information about the measurement has been employed. The method was tested for simulated and real data. The simulation results demonstrated the improved accuracy of estimations by PF in comparison with KF, especially when the assumption about GWN was violated.

Another main problem in E/MEG research is the inverse problem (source localization). The Inverse problem can be solved only by introducing restrictive assumptions about the head and signal propagation models. Among the existing solutions for the inverse problem, BF has the best spatial resolution. The BF approach described in Chapter 5 was generalized by including two more constraints within its formulation. One constraint minimizes the noise power at the output of the filter and the other deflates the location of the already identified sources. The multiply constrained problem was solved using the Lagrange multiplier method and the results were normalized to the power profile of noise only. Furthermore, an iterative deflation and localization method was introduced to improve the performance of the method. It was shown that the proposed deflation BF method has no dependence on the correlation between sources. The method is also useful when the classical BF identifies all the locations around the dominant source. Only when the sources are very close does the BF outperform the deflation BF. Unfortunately, both BF and deflation BF are still sensitive to the depth of sources.

In addition to the above method, RBPF and B-RBPF approaches were introduced in Chapter 6 for E/MEG dipole source localization. RBPF is a method that estimates source locations (the nonlinear part of the states) using PF and marginalizes out and estimate dipole moments (the linear part of the states) using KF. RBPF is robust in the face of different levels of noise power including spatially colored and real EEG background noise. RBPF performed consistently for superficial as well as deep sources, and had superb performance when the sources were correlated. The B-RBPF, which is a combination of RBPF and BF, is also robust in the face of different kinds and levels of noises. B-RBPF, in comparison to RBPF, is more consistent across

different locations and in the presence of correlations between sources. B-RBPF is particularly useful when the number of sources is unknown. In addition, B-RBPF has superior performance to other methods when the sources are close to each other. The major drawbacks of the method are the execution time and memory usage, which are considerably more than those of other approaches. Furthermore, for B-RBPF, along with choosing appropriate noise covariance matrices, a proper window length M should be chosen. The data in this window needs be stationary. In many cases it can be assumed that the real data around a short window is stationary, since the brain state does not change substantially over short periods of time (0.05-0.1sec). This assumption is much weaker than that required by the BF and RAP-MUSIC approaches, where the signal should be stationary over the whole data length.

In Chapter 7, a novel method for identifying ERP subcomponents was proposed. This method can be considered as one that can estimate both single trial parameters and source locations. In this method, the ERP subcomponent sources were modeled by ECDs and their moments were modeled by Gaussian waves. The un known parameters of the model were estimated using PF, ML, and the Newton-Raphson technique from trial to trial while the evolution of the parameters was assumed to be a first order Markovian process. The results obtained using simulated and real data showed the potential use of the method in real applications.

8.2 Future Work

PF is a recent and powerful method with many applications in engineering and science. To the best of our knowledge, however, this method has not been widely applied

to biomedical signals, especially E/MEG data. The method has considerable potential for solving problems in the growing biomedical signal processing area.

One application of PF would be establishing a new BCI technique, whereby the EEG signals are classified using spatial information. Currently, most BCI methods are based on time and frequency information.

Throughout this study dipole source localization was considered. Another approach - called distributed or tomographic source localization - has also been widely employed for analyzing E/MEG signals. An objective in forthcoming work is to extend the newly developed methods to tomographic source localization, under conditions where the locations of the sources are unknown. For example, in the deflation BF method proposed in Chapter 5, one approach would be starting the process by finding the tomograph image of each source separately, while deflating the others. By adding all tomograph images together, the end result should be a more accurate tomograph image than can be obtained without the deflation procedure.

With the available technology, achieving excellent spatial and temporal resolution is not possible unless neuroimaging techniques such as fMRI and E/MEG data are combined. Several methods for fusion of these modality have been proposed. New techniques based on PF may be helpful in this regard: likely source locations of E/MEG data can be constrained by fMRI data, and the time course data can contribute to an understanding of the temporal relationships between activity in regions identified via fMRI. The current work offers many opportunities for significant advances in medical image registration and data fusion.

Bibliography

- [1] A. Achim, F. Richer, and J. M. Saint-Hilaire, Methodological considerations for the evaluation of spatio-temporal source models, Electroencephalogr. Clin. Neurophysiol. 79 (1991), 227–240.
- [2] L. Albera, A. Ferrol, D. Cosandier-Riml, I. Merlet, and F. Wendling, *Brain source localization using a fourth-order deflation scheme*, IEEE Trans. Biomed., 55 (2008), no. 2, 490–501.
- [3] S. Andrews, R. Palaniappan, and V.S. Asirvadam, Single trial source separation of vep signals using selective principal components, Proc. 2nd International Conference on Advances in Medical Signal and Information Processing, September 2004, pp. 51–57.
- [4] M. S. Arulampalam, S. Maskell, N. Gordon, and T. Clapp, A tutorial on particle filters for online nonlinear/non-gaussian bayesian tracking, IEEE Trans. Signal Processing 50 (2002), no. 2, 174–188.
- [5] A. P. Bagshaw and T. Warbrick, Single trial variability of EEG and fMRI responses to visual stimuli, Neuroimage 38 (2007), 280–292.
- [6] S. Baillet, J. C. Mosher, and R. M. Leahy, *Electromagnetic brain mapping*, IEEE Signal Processing Magn. 18 (2001), 14–30.
- [7] D.S. Barth, W.W. Sutherling, and J. Beatty, Intracellular currents of interictal penicillin spikes: evidence from neuromagnetic mapping, Brain Res 368 (1986), 36–48.

- [8] E. A. Bartnik, K. J. Blinowska, and P. J. Durka, Single evoked-potential reconstruction by means of wavelet transform, Biological Cybernetics, 67 (1999), 175–181.
- [9] M. A. B. Brazier, Varieties of computer analysis of electrophysiological potentials, Electroenceph. and Clin. Neurophysiol. Supp. 26 (1967).
- [10] M. J. Brookes, C. M. Stevenson, G. R. Barnes, A. Hillebrand, M. I. G. Simpson, S. T. Francis, and P. G. Morris, Beamformer reconstruction of correlated sources using a modified source model, NeuroImage 34 (2007), no. 4, 1454-1465.
- [11] J. Bullier, *Integrated model of visual processing*, Brain Res. Rev. **36** (2001), 96–107.
- [12] C Campi, A Pascarella, and A Sorrentino, A Rao-Blackwellized particle filter for magnetoencephalography, Inverse Problems 24 (2008), no. 025023.
- [13] S. Cerutti, V. Bersani, A. Carrara, and D. Liberati, Analysis of visual evoked potentials through wiener filtering applied to a small number of sweeps, J. Biomed. Eng. 9 (1983), 3–12.
- [14] F. H. Y. Chan, F. K. Lam, P. W. F. Poon, and W. Qiu, Detection of brainstem auditory evoked potential by adaptive filtering, Med. Biol. Eng. Comput. 33 (1995), 69–75.
- [15] R. Chapman and J. McCrary, EP component identification and measurement by principal components analysis, Brain Cogn. 27 (1995), no. 3, 288–310.
- [16] S.R. Cherry and M.E. Phelps, *Brain mapping: The methods*, New York: Academic, 1996.
- [17] S. N. Cohen, K. Syndulko, B. Rever, J. Kraut, J. Coburn, and W. W. Tourtellotte, Visual evoked potentials and long latency event-related potentials in chronic renal failure, Neurology 33 (1983), 1219–1222.
- [18] M. G. H. Coles, H. G. O. M. Smid, M. K. Scheffers, and L. J. Otten, *Electrophysiology of mind*, ch. Mental chronometry and the study of human information processing, pp. 86–131, Oxford University Press, 1995.

- [19] H. Pratt D. H. Lange and G. F. Inbar, Segmented matched filtering of single event related evoked potentials, IEEE Trans. Biomed. Eng. 42 (1995), 317–321.
- [20] S. S. Dalal, K. Sekihara, and S. S. Nagarajan, Modified beamformers for coherent source region suppression., IEEE Trans Biomed Eng. 53 (2006), no. 7, 1357– 1363.
- [21] F. Darvas, D. Pantazis, E. Kucukaltun-Yildirim, and R. M. Leahy, Mapping human brain function with MEG and EEG: methods and validation, NeuroImage, 23 (2004), no. Suppl. 1, S289–S299.
- [22] J. de Munck, F. Bijma, P. Gaura, C. Sieluzycki, M. I. Branco, and R. Heethaa, A maximum likelihood estimator for trial-to-trial variations in noisy MEG/EEG data sets, IEEE Trans. Biomed. Eng. 51 (2004), no. 12, 2123-2128.
- [23] J. C. de Munck, The estimation of time varying dipoles on the basis of evoked potentials, Electroencephalogr. Clin. Neurophysiol. 77 (1990), 156–160.
- [24] S. Delsanto, F. Lamberti, and B. Montrucchio, Automatic ocular artifact rejection based on independent component analysis and eyeblink detection, in Proceedings of International IEEE EMBS Conf. on Neural Engineering (2003), 309–312.
- [25] A. Devor, A. K. Dunn, M. L. Andermann, I. Ulbert, D. A. Boas, and A. M. Dale, Coupling of total hemoglobin concentration, oxygenation, and neural activity in rat somatosensory cortex, Neuron 39 (2003), 353–359.
- [26] L. Din and B. He, Spatio-temporal EEG source localization using a three-dimensional subspace FINE approach in a realistic geometry inhomogeneous head model, IEEE Trans. Biomed. Eng. 53 (2006), no. 9, 1732–1739.
- [27] A. Dogandzic and A. Nehorai, Estimating evoked dipole responses in unknown spatially correlated noise with EEG/MEG arrays, IEEE Trans. on Signal Proc. 48 (2000), no. 1, 13–25.
- [28] E. Donchin and M. G. H. Coles, Is the p300 component a manifestation of context updating?, Behavioral and Brain Science 11 (1988), 355-372.

- [29] A. Doucet, N. Freitas, and N. Gordon, Sequential monte carlo metods in practice, Springer, 2001.
- [30] M. Fabre-Thorpe, G. Richard, and S. J. Thorpe, Rapid categorization of natural images by rhesus monkeys, R. Neuroreport 9 (1998), 303–308.
- [31] D. Cabrera Fernandez, R. Grave de Peralta Menendez, and S.L. Gonzalez Andino, *Some limitations of spatio-temporal source models*, Brain Topogr 7 (1995), 87–93.
- [32] T. Frodl, G. Juckel, J. Gallinat, R. Bottlender, M. Riedel, U. Preuss, H. J. Muller, and U. Hegerl, Dipole localization of P300 and normal aging, Brain Topography 13 (2000), no. 1, 3–9.
- [33] J. S. George, C. J. Aine, J. C. Mosher, D. M. Schmidt, D. M. Ranken, H. A. Schlitt, C. C. Wood, J. D. Lewine, J. A. Sanders, and J W. Belliveau, Mapping function in the human brain with magnetoencephalography, anatomical magnetic resonance imaging, and functional magnetic resonance imaging (review), J. Clin. Neurophysiol. 12 (1995), 406-431.
- [34] S. D. Georgiadis, P. O. Ranta-aho, M. P. Tarvainen, and P. A. Karjalainen, Single-trial dynamical estimation of event-related potentials: a Kalman filter based approach, IEEE Trans. Biomed. Eng 52 (2005), no. 8, 1397–1406.
- [35] J. Gerson, V. A. Vardenas, and G. Fein, Equivalent dipole parameter estimation using simulated annealing, Electroenceph. Clin. Neurophysiol. 92 (1994), 161–168.
- [36] D. S. Goodin, K. C. Squires, and A. Starr, Long latency event-related components of the auditory evoked potential in dementia, Brain 101 (1978), 635–648.
- [37] D. Gutierrez, A. Nehorai, and A. Dogandzic, Performance analysis of reduced-rank beamformers for estimating dipole source signals using EEG/MEG, IEEE Trans. Biomed. Eng 53 (2006), no. 5, 840–844.
- [38] A. R. Haig, E. Gordon, G. Rogers, and J. Anderson, Classification of single-trial ERP sub-types: Application of globally optimal vector quantization using simulated annealing, Clinical Neurophysiology 94 (1995), 288–297.

- [39] H. Haneishi, N. Ohyama, K. Sekihara, and T. Honda, Multiple current dipole estimation using simulated annealing, IEEE Trans. Biomed. Eng. 41 (1994), no. 1004-1009.
- [40] Simon Haykin, Adaptive filter theory (2nd ed.), Prentice-Hall, Inc., Upper Saddle River, NJ, USA, 1991.
- [41] B. He, T. Musha, Y. Okamoto, S. Homma, Y. Nakajima, and T. Sato, Electric dipole tracing in the brain by means of the boundary element method and its accuracy, IEEE Trans. Biomed., 34 (1987), no. 6, 406-414.
- [42] U. Hegerl and T. Frodl-Bauch, Dipole source analysis of P300 component of the auditory evoked potential: a methodological advance?, Psychiatry Res. 72 (1997), no. 2, 109–118.
- [43] V. Homberg, H. Hefter, G. Granseyer, W. Strauss, H. Lange, and M. Hennerici, Event-related potentials in patients with huntington's disease and relatives at risk in relation to detailed psychometry, Electroenc. Clin. Neurophisiol. 63 (1986), 552-569.
- [44] A.M. Howseman and R.W. Bowtell, Functional magnetic resonance imaging: Imaging techniques and contrast mechanisms, Philos. Trans. R. Soc. London B, Biol. Sci. 354 (1999), 1179–1194.
- [45] J. E. Hudson, Adaptive array principles, Peregrinus Ltd., Stevenage, U.K., 1981.
- [46] H. B. Hui and R.M. Leahy, Linearly constrained MEG beamformers for MVAR modeling of cortical interactions, 2006, pp. 237–240.
- [47] P. Jaskowski and R. Verleger, Amplitudes and latencies of single trial ERPs estimated by a maximum likelihood method, IEEE Trans. Biomed. Eng 46 (1999), 987–993.
- [48] _____, An evaluation of methods for single-trial estimation of p3 latency, Psychophysiology 37 (2000), 153–162.
- [49] J. J.Foxe, M. E. McCourt, and D. C. Javitt, Right hemisphere control of visuospatial attention: line-bisection judgments evaluated with high-density electrical mapping and source analysis, Neuroimage 19 (2003), 710–726.

- [50] R. Johnson, Advances in psychophysiology, ch. The amplitude of the P300 component of the event related potential: review and synthesis, pp. 69–137, JAI Press, Greenwich, 1988.
- [51] M. L. A. Jongsma, T. Eichele, C. M. Van Rijn, A. M. L. Coenen, K. Hugdahl, H. Nordby, and R. Q. Quiroga, Tracking pattern learning with single-trial eventrelated potentials, Clinical Neurophysiology 117 (2006), 1957–1973.
- [52] T. Jung, S. Makeig, M. Westerfield, J. Townsend, E. Courchesne, and T. J. Sejnowski, Analysis and visualization of single-trial event-related potentials, Human Brain Mapping 14 (2001), 166–185.
- [53] P. Karjalainen, J. Kaipio, A. Koistinen, and M. Vauhkonen, Subspace regularization method for the single trial estimation of evoked potentials, IEEE Trans. Biomed. Eng. 46 (1999), 849–860.
- [54] R. N. Kavanagh, T. M. Darcey, D. Lehmann, and D. H. Fender, Evaluation of method for three-dimensional localization of electrical sources in the human brain, IEEE Trans. Biomed. Eng. 25 (1978), 421–429.
- [55] S. M. Kay, Fundamentals of statistical signal processing, volume I: Estimation theory, Englewood Cliffs, NJ: Prentice-Hall, Inc., 1993.
- [56] G. Kitagawa, Monte carlo filter and smoother for non-Gaussian nonlinear state space models, J. Computational and Graphical Statistics (1996), no. 93, 1203– 1205.
- [57] K. H. Knuth, A. S. Shah, W. A. Truccolo, M. Ding, S. L. Bressler, and C. E. Schroeder, Differentially variable component analysis: Identifying multiple evoked components using trial-to-trial variability, Journal of Neurophysiology 95 (2006), 3257–3276.
- [58] A. Korvenoja, J. Huttunen, E. Salli, H. Pohjonen, S. Martinkauppi, J. M. Palva, L. Lauronen, J. Virtanen, R. J. Ilmoniemi, and H. J. Aronen, Activation of multiple cortical areas in response to somatosensory stimulation: combined magnetoencephalographic and functional magnetic resonance imaging, Hum Brain Mapp 8 (1999), 13–27.

- [59] D. H. Lange and G. F. Inbar, A robust parametric estimator for single-trial movement related brain potentials, IEEE Trans. Biomed. Eng. 43 (1996), no. 4, 341–347.
- [60] D. H. Lange, H. Pratt, and G. F. Inbar, Modeling and estimation of single evoked brain potential components, IEEE Trans. Biomed. Eng. 44 (1997), no. 9, 791–799.
- [61] S. Lemm, G. Curio, Y. Hlushchuk, and K. R. Mller, Enhancing the signal-tonoise ratio of ICA-based extracted ERPs, IEEE Trans. Biomed. Eng. 53 (2006), no. 4, 601–607.
- [62] T. Limpiti, B. D. Van Veen, H. T. Attias, and S. S. Nagarajan, A spatiotemporal framework for estimating trial-to-trial amplitude variation in event-related MEG/EEG, Biomed. Engin., IEEE Transa. on 56 (2009), no. 3, 633–645.
- [63] J. S. Liu, Metropolized independent sampling with comparison to rejection sampling and importance sampling, Stat. Comput. 6 (1996), 113–119.
- [64] N. K. Logothetis, J. Pauls, M. Augath, T. Trinath, and A. Oeltermann, Neurophysiological investigation of the basis of the fMRI signal, Nature 412 (2001), 150–157.
- [65] S. J. Luck, An introduction to the event-related potential technique, MIT press, 2005.
- [66] B. Lutkenhoner, Dipole source localization by means of maximum likelihood estimation I-Theory and simulations, Electroencephalogr. Clin. Neurophysiol. 106 (1998), 314–321.
- [67] J. Maarten, Noise reduction by wavelet thresholding, New York, 2001.
- [68] V. Makinen, P. May, and H. Tiitinen, The use of stationarity and nonstationarity in the detection and analysis of neural oscillations, NeuroImage 28 (2005), 389–400.
- [69] S. Mallat, A wavelet tour of signal processing, Academic Press, 1999.

- [70] C. D. McGillem and J. I. Aunon, Measurement of signal components in single visually evoked brain potentials, IEEE Trans. Biomed. Eng 24 (1977), 232-241.
- [71] C. M. Michela, M. M. Murraya, G. Lantza, S. Gonzaleza, L. Spinellib, and R. G. de Peralta, *EEG source imaging*, Clinical Neurophysiology 115 (2004), 2195–2222.
- [72] W. Miltner, C. Braun, J. R. Johnson, G. V. Simpson, and D. S. Ruchkin, A test of brain electrical source analysis (BESA): a simulation study, Electroencephalogr Clin Neurophysiol 91 (1994), 295–310.
- [73] J. Mocks, T. Gasser, and P. Tuan, Variability of single visual evoked potentials evaluated by two new statistical tests, Electroenceph. Clin. Neurophysiol. 57 (1984), 571–580.
- [74] H. R. Mohseni, F. Ghaderi, E. L. Wilding, and S. Sanei, *A beamforming particle filter for EEG dipole localization*, Proc. IEEE Int. Conf. Acoust., Speech, Signal Process. (ICASSP), 2009, pp. 337–340.
- [75] H. R. Mohseni, E. L. Wilding, and S. Sanei, Sequential monte carlo techniques for EEG dipole placing and tracking, Proc. The 5th IEEE Sensor Array and Mutichanel Signal Process. workshop (SAM), July 2008, pp. 95–98.
- [76] H. R. Mohseni, E.L. Wilding, and S. Sanei, *Pre-processing of event-related potential signals via kalman filtering and smoothing*, 15th IEEE International Conference on Digital Signal Processing (DSP), 2007, pp. 179–182.
- [77] H. R. Mohseni, E.L. Wilding, and S. Sanei, Sequential Monte Carlo techniques for EEG dipole placing and tracking, Proc. The 5th IEEE Sensor Array and Mutichanel Signal Processing workshop (SAM), July 2008, pp. 95–98.
- [78] J. C. Mosher and R.M. Leahy, Source localization using recursively applied and projected (rap) music, IEEE Trans. on Signal Processing 47 (1999), no. 2, 332– 340.
- [79] J. C. Mosher, P. S. Lewis, and R. M. Leahy, Multiple dipole modeling and localization from spatio-temporal meg data, IEEE Trans. Biomed. 39 (1992), 541–557.

- [80] J. C. De Munck, H. M. Huizenga, L. J. Waldorp, and R. M. Heethaar, Estimating stationary dipoles from MEG/EEG data contaminated with spatially and temporally correlated background noise, IEEE Trans Signal Processing 50 (2002), 565-1572.
- [81] J. C. De Munck, P. C. M. Vijn, and F. H. Lopes da Silva, A random dipole model for spontaneous brain activity, IEEE Trans. Biomed Eng 39 (1992), 791–804.
- [82] E. Niedermeyer and F. L. Da Silva, Electroencephalography: Basic principles, clinical applications, and related fields, Lippincott Williams and Wilkins, 1999.
- [83] P.L. Nunez, Electric fields of the brain, New York: Oxford, 1981.
- [84] R. Oostenvelda and P. Praamstra, The five percent electrode system for highresolution EEG and ERP measurements, Clin. Neurophysiol. 112 (2001), no. 4, 713-719.
- [85] K. B. Petersen and M. S. Pedersen, *The matrix cookbook*, [Online]. Available: http://www2.imm.dtu.dk/pubdb/p.php?3274, 2007.
- [86] D. T. Pham, J. Mcks, W. Khler, and T. Gasser, Variable latencies of noisy signals: estimation and testing in brain potential data, Biometrika 74 (1987), 525–533.
- [87] J. Polich, Updating P300: An integrative theory of P3a and P3b, Clin Neurophysiol (2007), no. 118, 2128–2148.
- [88] R. Polikara, A. Topalisa, D. Greenb, J. Kouniosb, and C. M. Clarke, Comparative multiresolution wavelet analysis of ERP spectral bands using an ensemble of classifiers approach for early diagnosis of alzheimer's disease, Computers in Biology and Medicine 37 (2007), no. 4, 542–558.
- [89] C. J. Purcell and G. Stroink, Moving dipole inverse solutions using realistic torso models, IEEE Trans. On Biomed. Engin. 38 (1991), no. 1, 82–84.
- [90] R. Q. Quiroga and H. Garcia, Single-trial event-related potentials with wavelet denoising, Clinical Neurophysiology 114 (2003), no. 2, 376–290.

- [91] P. O. Ranta-aho, A. S. Koistinen, J. O. Ollikainen, J. P. Kaipio, J. Partanen, and P. A. Karjalainen, Single-trial estimation of multichannel evoked-potential measurements, IEEE Trans. Biomed. Eng. 50 (2003), no. 2, 189–196.
- [92] S. E. Robinson and J. Vrba, Functional neuroimaging by synthetic aperture magnetometry (SAM), Recent Advances in Biomagnetism (T. Yoshimoto, M. Kotani, S. Kuriki, H. Karibe, and N. Nakasato, eds.), Japan: Tohoku Univ. Press, 1999, pp. 302–305.
- [93] W. T. Roth and E. H. Cannon, Some features of the auditory evoked response in schizophrenics, Arch Gen Psychiatry 27 (1972), 466–471.
- [94] T. Sander, M. Burghoff, G. Curio, and L. Trahms, Single evoked somatosensory MEG responses extracted by time delayed decorrelation, IEEE Transactions on Signal Processing 53 (2005), 3384–3392.
- [95] S. Sanei and J. Chambers, EEG signal processing, John Wiley and Sons, 2007.
- [96] M. Scherg, Functional imaging and localization of electromagnetic brain activity, Brain Topogr. 5 (1993), 103–111.
- [97] M Scherg and D. Von Cramon, Two bilateral sources of the late AEP as identified by a spatiotemporal dipole model, Electroencephalogr. Clin. Neurophysiol. **62** (1985), 32–44.
- [98] M. Scherg and D. Von Cramon, Evoked dipole source potentials of the human auditory cortex, Electroencephalogr. Clin. Neurophysiol. 65 (1986), 344–360.
- [99] R. O. Schmidt, Multiple emitter location and signal parameter estimation, IEEE Trans. Antennas Propag. 34 (1986), no. 3, 276–280.
- [100] V. Smidl and A. Quinn, The variational bayes method in signal processing, Berlin, Germany: Springer.
- [101] E. Somersalo, A. Voutilainen, and J.P. Kaipio, Non-stationary magnetoencephalography by bayesian filtering of dipole models, Inverse Problems 19 (2003), 1047–1063.

- [102] M. V. Spreckelsen and B. Bromm, Estimation of single-evoked cerebral potentials by means of parametric modeling and Kalman filtering, IEEE Trans. Biomed. Eng 35 (1988), no. 9, 691–700.
- [103] L. Spyrou and S. Sanei, Source localization of event-related potentials incorporating spatial notch filters, Biomed. Engin., IEEE Trans. on 55 (2008), no. 9, 2232–2239.
- [104] S. Sutton, M. Braren, J. Zubin, and E. R. John, Evoked-potential correlates of stimulus uncertainty, Science 150 (1965), 1187–1188.
- [105] H. Tanakaa, T. Koeniga, R. D. Pascual-Marquia, K. Hiratab, K. Kochia, and D. Lehmann, Event-related potential and EEG measures in parkinson's disease without and with dementia, Dementia and Geriatric Cognitive Disorders 11 (2000), 39-45.
- [106] N. V. Thakor, Adaptive filtering of evoked potentials, IEEE Trans. Biomed. Eng. 34 (1987), 6–12.
- [107] W. A. Truccolo, M. M. Ding, K. H. Knuth, R. Nakamura, and S. L. Bressler, Trial to trial variability of cortical evoked responses: implications for the analysis of functional connectivity, Clin. Neurophys. 113 (2002), 206-226.
- [108] W. A. Truccolo, K. H. Knuth, A. Shah, S. L. Bressler, C. E. Schroeder, and M. Ding, Estimation of single-trial multicomponent ERPs: Differentially variable component analysis (dVCA), Biological Cybernetics 89 (2003), 426–438.
- [109] K. Uutela, M. Hamalainen, and R. Salmelin, Global optimization in the localization of neuromagnetic sources, IEEE Trans. Biomed. 45 (1998), 716–723.
- [110] B. D. Van Veen and K. Buckley, Beamforming: A versatile approach to spatial filtering, EEE ASSP Mag. 5 (1988), no. 2, 4–24.
- [111] B. D. Van Veen, W. Van Dronglen, M. Yuchtman, and A. Suzuki, Localization of brain electrical activity via linearly constrained minimum variance spatial filtering, IEEE Trans. Biomed. Eng. 44 (1997), 867–880.

- [112] Ricardo Nuno Vigrio, Extraction of ocular artefacts from EEG using independent component analysis, Electroencephalography and Clinical Neurophysiology 103 (1997), no. 3, 395 404.
- [113] A. Villringer and B. Chance, Noninvasive optical spectroscopy and imaging of human brain function, Trends Neurosci. 20 (1997), 435–442.
- [114] J. Vrba and S. E. Robinson, Signal processing in magnetoencephalography, Methods 25 (2001), no. 2, 249–271.
- [115] L. J. Waldorp, H. M. Huizenga, R. P. P. P. Grasman, B. E. Bcker, J. C. de Munck, and P. C. M. Molenaar, Model selection in electromagnetic source analysis with an application to VEFs, IEEE Trans. Biomed. Eng. 49 (2002), 1121–1129.
- [116] L. J. Waldorp, H. M. Huizenga, A. Nehorai, R. P. P. P. Grasman, and P. C. M. Molenaar, Model selection in spatio-temporal electromagnetic source analysis, IEEE Trans. Biomed. Eng. 52 (2005), 414–420.
- [117] C. C. Wood, Application of dipole localization methods to source identification in human evoked potentials, Ann. N.Y. Acad. Sci. 388 (1982), 139–155.
- [118] C. D. Woody, Characterization of an adaptive filter for the analysis of variable latency neuroelectric signals, Medical and Biological Engineering and Computing 5 (1967), no. 6, 539–554.
- [119] L. Xu, P. Stoica, S. L. Bressler J. Li, X. Shao, and M. Ding, ASEO: A method for the simultaneous estimation of single-trial event-related potentials and ongoing brain activities, IEEE Trans. Biomed. Eng. 56 (2009), 111–121.
- [120] X. L. Xu, B. Xu, and B. He, An alternative subspace approach to EEG dipole source localization, Phys. Med. Biol. 49 (2004), 327–343.
- [121] C. S. Ycki, R. Konig, A. Matysiak, R. Kus, D. Ircha, and P.J. Durka, Single-trial evoked brain responses modeled by multivariate matching pursuit, Biomed. Engin., IEEE Trans. on 56 (2009), no. 1, 74–82.

- [122] K. Yu and C. D. McGillem, Optimum filters for estimating evoked potential waveforms, IEEE Trans. Biomed. Eng. 30 (1983), 730-737.
- [123] A. Zia, T. Kirubarajan, J. P. Reilly, Derek Yee, K. Punithakumar, and Shahram Shirani, An EM algorithm for nonlinear state estimation with model uncertainties, IEEE Trans. On Signal Process. 56 (2008), no. 3, 921–936.